International Journal of Engineering (IJE)

ISSN : 1985-2312

VOLUME 4, ISSUE 2

PUBLICATION FREQUENCY: 6 ISSUES PER YEAR

International Journal of Engineering (IJE)

Volume 4, Issue 2, 2010

Edited By
Computer Science Journals
www.cscjournals.org

Editor in Chief Dr. Kouroush Jenab

International Journal of Engineering (IJE)

Book: 2010 Volume 4, Issue 2

Publishing Date: 31-03-2010

Proceedings

ISSN (Online): 1985-2312

IJE Journal is a part of CSC Publishers

http://www.cscjournals.org

Published in Malaysia

Typesetting: Camera-ready by author, data conversation by CSC Publishing Services – CSC Journals, Malaysia

CSC Publishers

Editorial Preface

This is the second issue of volume fourth of International Journal of Engineering (IJE). The Journal is published bi-monthly, with papers being peer reviewed to high international standards. The International Journal of Engineering is not limited to a specific aspect of engineering but it is devoted to the publication of high quality papers on all division of engineering in general. IJE intends to disseminate knowledge in the various disciplines of the engineering field from theoretical, practical and analytical research to physical implications and theoretical or quantitative discussion intended for academic and industrial progress. In order to position IJE as one of the good journal on engineering sciences, a group of highly valuable scholars are serving on the editorial board. The International Editorial Board ensures that significant developments in engineering from around the world are reflected in the Journal. Some important topics covers by journal are nuclear engineering, mechanical engineering, computer engineering, electrical engineering, civil & structural engineering etc.

The coverage of the journal includes all new theoretical and experimental findings in the fields of engineering which enhance the knowledge of scientist, industrials, researchers and all those persons who are coupled with engineering field. IJE objective is to publish articles that are not only technically proficient but also contains information and ideas of fresh interest for International readership. IJE aims to handle submissions courteously and promptly. IJE objectives are to promote and extend the use of all methods in the principal disciplines of Engineering.

IJE editors understand that how much it is important for authors and researchers to have their work published with a minimum delay after submission of their papers. They also strongly believe that the direct communication between the editors and authors are important for the welfare, quality and wellbeing of the Journal and its readers. Therefore, all activities from paper submission to paper publication are controlled through electronic systems that include electronic submission, editorial panel and review system that ensures rapid decision with least delays in the publication processes.

To build its international reputation, we are disseminating the publication information through Google Books, Google Scholar, Directory of Open Access Journals (DOAJ), Open J Gate, ScientificCommons, Docstoc and many more. Our International Editors are working on establishing ISI listing and a good impact factor for IJE. We would like to remind you that the success of our journal depends directly on the number of quality articles submitted for review. Accordingly, we would like to request your participation by submitting quality manuscripts for review and encouraging your colleagues to submit quality manuscripts for review. One of the great benefits we can

provide to our prospective authors is the mentoring nature of our review process. IJE provides authors with high quality, helpful reviews that are shaped to assist authors in improving their manuscripts.

Editorial Board Members
International Journal of Engineering (IJE)

Editorial Board

Editor-in-Chief (EiC)

Associate Editors (AEiCs)

Editorial Board Members (EBMs)

Table of Contents

Volume 4, Issue 2, May 2010.

The modeling of UPFC based on circuit elements in an exact transmission line model

Ali akbar Motiebirjandi motiebirjandi@srttu.edu
Faculty of Electrical Engineering / assistant professor
Shahid Rajaee University/ Tehran, 67616, Iran

Kauomars Sabzawari k_sabzawari@yahoo.com
Faculty of Electrical Engineering / M.Sc
Shahid Rajaee University/ Tehran, 67616, Iran

Abstract

UPFC is considered and known as one of the best FACTS devices. It is a combination of series and parallel quick compensation, and can therefore provide active and reactive control to achieve maximum power transfer, system stability and improve power quality and reliability. Therefore, presenting a suitable model for UPFC which enables studying the network and load flow in energy transmission lines, has gotten the experts' attention. This paper presents a new model of UPFC in steady state based on circuit elements in an exact transmission line model. Considering the fact that the elements like UJT and tunnel diode in negative resistance region cause power increase, the model determines the value of the active and reactive power injected by the series converter into the network, and then the series converter of UPFC is simulated by means of a negative resistor and an induction or capacitor reactance. Resistance and reactance are expressed as functions of voltage of buses, load angle, voltage injection and fire angle of series converter. The relations of this model have been achieved in a two-bus system and have been simulated in 14- and 30- bus standard.

Keywords: FACTS, UPFC, Load Flow, Reactive Power Control, Active Power Control.

1. INTRODUCTION

Unified power flow controller is a multi-functional inter-mediator in FACTs devices family. UPFC can act as a parallel or series compensator, voltage regulator, phase replacer or power controller in different conditions by simultaneous control of line parameters [1]. Different models of UPFC are presented in steady state, including:

UPFC model based on voltage sources and series impedance: in this model the series and parallel converters are replaced by a voltage source and series impedance [2],[3].

UPFC model based on ideal voltage and current sources: in this model the series converter is replaced by a voltage source and the parallel converter by an ideal current source [4].

UPFC injection mode: in this model the series and parallel converters are replaced by a voltage source and series impedance and are then combined with the π-line model [5].

UPFC hybrid model: in this model the series converter is replaced by a series voltage source and leakage impedance related to the series transformer, and the parallel converter is replaced by two ideal current sources; one expresses the shunt converter's active power and its loss, and the other indicates the reactive power of the shunt converter and its loss. [6]

This paper presents a new model of UPFC in steady state based on the circuit elements in the exact transmission line model in a way that the series converter injection active power can be simulated with a negative resistance and the series converter injection reactive power can be simulated with a capacitor or inductive reactance, and the parallel converter reactive power will be shown as a connected power to the bus. Equations of the resistance and reactance are computed in two–bus single machine power system in the approximate transmission line model. The model is then generalized to exact transmission line model and simulated in 14- and 30–bus power system.

2. UPFC model based on circuit elements

UPFC series converter injects active and reactive power to the network by injecting series voltage into the transmission line with controllable phase amplitude and angle. The series converter provides the required active power through the capacitor link and the parallel converter through the network. Also, each converter can inject reactive power to the network or receive from it independently (see figure 1).

In the existing UPFC models, converters are replaced by voltage or current sources and the controller final model is shown as the injection power to the bus which causes changes in the Jacobean matrix and the load flow program structure. The goal of this paper is to model the UPFC series converter with a resistance -which expresses the injected active power of series converter to the line- in steady state, and also to model the injected reactive power with a reactance so that the reactive power of parallel converter can be shown as connected power to the bus .

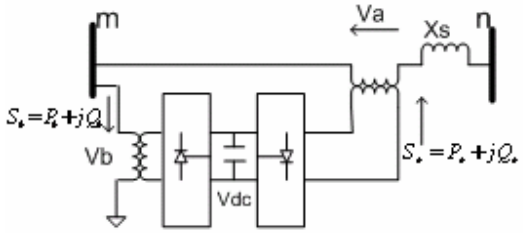

FIGURE 1: UPFC is placed in two- bus power system

In this model, we assume that the active and reactive power exchanged between the series converter and the network is known. Therefore, knowing the amplitude of buses' voltages and series converter injection voltage, we can compute the resistance and reactance values to replace the series converter.

Modelling of the Series Converter

For modelling of the UPFC series converter in steady state, the following assumptions are considered:

1- First, we consider the UPFC voltage source model in a two-bus one-machine system as depicted in figure 2 and by calculating the line current, we will obtain the active and reactive power injected by the series converter.
2- Then, we model the active power injected by a series converter with a negative resistance. The series converter reactive power is also modelled with a capacitive or inductive reactance, considering the type of the series converter.

Calculation of injected active and reactive power of the series converter

First, we obtain the electrical equations for figure 2 and calculate the series converter injection power.

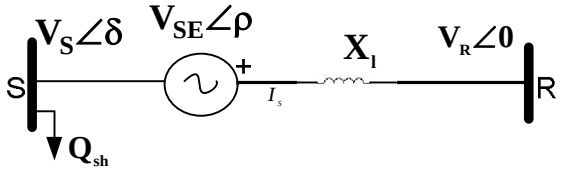

FIGURE 2: UPFC in a two–bus network

Flowing current in the line is calculated as follows:

$$I = \frac{V_S\angle\delta + V_{SE}\angle\rho - V_R\angle 0}{jX_L} \quad (1)$$

The active and reactive power injected by the series converter is expressed by the following equation:

$$S_{SE} = V_{SE} * \overset{*}{I} \quad (2)$$

Replacing the first equation in the second one and expanding it, the active and reactive power injected by the series converter is achieved:

$$P_{SE} = \frac{V_S * V_{SE}}{X_L}\sin(\delta-\rho) + \frac{V_R * V_{SE}}{X_L}\sin(\rho) \quad (3)$$

$$Q_{SE} = \frac{V_S * V_{SE}}{X_L}\cos(\delta-\rho) - \frac{V_R * V_{SE}}{X_L}\cos(\rho) + \frac{V_{SE}^2}{X_L} \quad (4)$$

The active and reactive power of the series converter can be modelled with a resistance and a reactance, respectively.

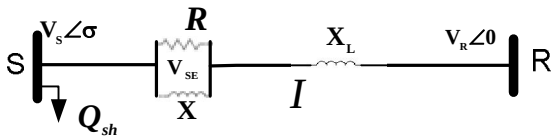

FIGURE 3: Modeling of the series converter with parallel

$$R = \frac{V_{SE}^2}{P_{SE}} \quad (5)$$

$$X = \frac{V_{SE}^2}{Q_{SE}} \quad (6)$$

To prove our assumptions, we calculate the R bus absorbed power for the both systems shown in figures 2 and 3 and show that the value of absorbed power by the R bus in the series converter voltage model and our own model are the same.

Calculation of the active and reactive power absorbed by the R bus in the UPFC voltage source model

The power of the R bus in the two–bus system of figure 2 is calculated using the following equation:

$$S_R = V_R * \overset{*}{I} \quad (7)$$

Replacing equation 1 in the above equation we have:

$$S_R = V_R * (\frac{V_S \angle \delta + V_{SE} \angle \rho - V_R \angle 0}{jX_L})^* \quad (8)$$

Expanding this equation yields the following equation:

$$S_R = P_R + jQ_R \quad (9)$$

So, the active and reactive power absorbed by the R bus can be expressed by these equations:

$$P_R = \frac{V_S * V_R}{X_L} \sin(\delta) + \frac{V_R * V_{SE}}{X_L} \sin(\rho) \quad (10)$$

$$Q_R = \frac{V_S * V_R}{X_L} \cos(\delta) - \frac{V_R * V_{SE}}{X_L} \cos(\rho) - \frac{V_R^2}{X_L} \quad (11)$$

In the next section, the active and reactive power absorbed by the R bus will be calculated with the new UPFC model and we will show that the results are the same.

Calculating the active and reactive power absorbed by the R bus in the UPFC circuitry elements model

The flowing current in the two-bus system of figure 3 are as follows:

$$I = \dot{I}_R + \dot{I}_L \quad (12)$$

$$I_R = \frac{V_{SE} \angle \rho}{R} \quad (13)$$

$$I_L = \frac{V_{SE} \angle \rho}{jX} \quad (14)$$

Replacing the equations 13 and 14 in equation 12, we conclude:

$$I = \frac{V_{SE} \angle \rho}{R} + \frac{V_{SE} \angle \rho - 90}{X} \quad (15)$$

By expanding the above equation:

$$I = \frac{V_{SE}}{R} \cos\rho + \frac{V_{SE}}{X} \sin\rho + j\frac{V_{SE}}{R} \sin\rho - j\frac{V_{SE}}{X} \cos\rho \quad (16)$$

Using this equation and $S_R = V_R * \overset{*}{I}$, we will have:

$$S_R = \frac{V_{SE} V_R}{R} \cos\rho + \frac{V_{SE} V_R}{X} \sin\rho - j\frac{V_{SE} V_R}{R} \sin\rho + j\frac{V_{SE} V_R}{X} \cos\rho \quad (17)$$

The active and reactive power absorbed by the R bus:

$$P_R = \frac{V_{SE} * V_R}{R}\cos\rho + \frac{V_{SE} * V_R}{X}\sin\rho \quad (18)$$

$$Q_R = -\frac{V_{SE} * V_R}{R}\sin\rho + \frac{V_{SE} * V_R}{X}\cos\rho \quad (19)$$

Inserting equations 5 and 6 in 18 and 19, we have:

$$P_R = \frac{V_S * V_R}{X_L}\sin(\delta) + \frac{V_R * V_{SE}}{X_L}\sin(\rho) \quad (20)$$

$$Q_R = \frac{V_S * V_R}{X_L}\cos(\delta) - \frac{V_R * V_{SE}}{X_L}\cos(\rho) - \frac{V_R^2}{X_L} \quad (21)$$

Comparing the equations 10, 11, 20 and 21, we can say that the active and reactive power absorbed by the R bus in the systems shown in figures 2 and 3 are the same. Consequently UPFC series converter can be modeled with resistance and reactance.

Direct calculation of resistance and reactance equivalent to series converter

Inserting relations (10) and (11) in (5) and (6) we have :

$$R = \frac{V_{SE} * X_L}{V_S \sin(\delta - \rho) + V_R \sin\rho} \quad (22)$$

$$X = \frac{V_{SE} * X_L}{V_S \cos(\delta - \rho) - V_R \cos\rho + V_{SE}} \quad (23)$$

In this relationship , V_S and V_R are the amplitude of buses voltage , δ is the angle between buses voltage , V_{SE} , ρ are the amplitude and angle of injected voltage to series converter and X_L is the line reactance .

Assuming the series converter and buses voltage and also load angle are fixed , the resistance and reactance are only a subordinate of series converter fire angle and can replace the series converter.

In order that this model can be simulated in load flow program , parallel elements convert to series elements.

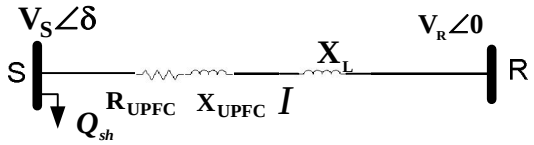

FIGURE 4: Modelling the UPFC in two –bus power system

The impedance equivalent to parallel elements equals to:

$$R_{UPFC} = \frac{R * X^2}{R^2 + X^2} \quad (24)$$

$$X_{UPFC} = \frac{X * R^2}{R^2 + X^2} \quad (25)$$

Therefore , by having buses voltage and the injected voltage of series converter values and the active and reactive power value the series converter exchanges with network , the values of resistance and reactance can be calculated , and put instead of series converter and also show the reactive power of parallel converter as connected power to bus.

Modelling the UPFC in the exact transmission line model

In the previous section, we obtained the UPFC model based on the circuitry in the approximate transmission line model. In this section, we model it in the exact transmission line model. To perform this modelling, we consider the UPFC in the two–bus single-machine system in the exact transmission line model in which the effects of the line capacitors are also considered. Figure 5 depicts the described model.

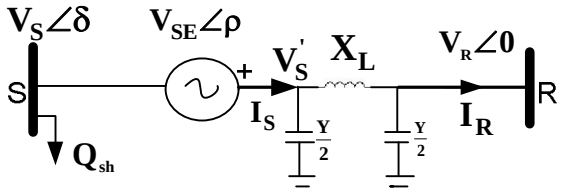

FIGURE 5: UPFC placed in exact line model

To calculate the active and reactive power exchanged between the series converter and the network, we first obtain the current I_S considering the equations between the current and voltage of the line model which is a bipolar network:

$$\begin{bmatrix} V'_S \\ I_S \end{bmatrix} = \begin{bmatrix} A & B \\ C & D \end{bmatrix} \begin{bmatrix} V_R \\ I_R \end{bmatrix} \quad (26)$$

in which:

$$V'_S = V_S\angle\delta + V_{SE}\angle\rho \quad (27)$$

$$A = D = (1 + \frac{YZ}{2}) \quad (28)$$

$$B = Z \quad (29)$$

$$C = Y(1 + \frac{YZ}{2}) \quad (30)$$

Considering figure 5, we can write:

$$Z = jX_L \quad (31)$$

$$Y = j\omega c = \frac{j}{X_C} \quad (32)$$

Using equation 26, the transmitter line current equation can be written:

$$I_S = \frac{D}{B} V'_S + \frac{CB - AD}{B} V_R \quad (33)$$

Inserting equations 27 to 32 in equation 33, the current equation is achieved as follows:

$$I = \frac{V_S \angle \delta + V_{SE} \angle \rho - V_R \angle 0}{jX_L} + \frac{V_S \angle \delta + V_{SE} \angle \rho}{-j2X_C} \tag{34}$$

The active and reactive power that the series converter exchanges with the network is obtained as follows:

$$P_{SE} - jQ_{SE} = V_{SE}^{*} * I \tag{35}$$

in which:

$$\overset{*}{V}_{SE} = V_{SE} \angle -\rho \tag{36}$$

Inserting equations 34 and 36 in equation 35 yields the following results:

$$\begin{aligned} P_{SE} - jQ_{SE} = {} & \frac{V_S * V_{SE}}{X_L} \angle (2\delta - \rho - 90) - \frac{V_R * V_{SE}}{X_L} \angle (\delta - \rho - 90) + \\ & \frac{V_{SE}^2}{X_L} \angle -90 + \frac{V_{SE}^2}{2X_C} \angle 90 + \frac{V_S * V_{SE}}{2X_C} \angle (\delta - \rho + 90) \end{aligned} \tag{37}$$

By expanding the above equation, the active and reactive power injected by the series converter is achieved as follows:
the active power that the series converter injects into the network:

$$P_{SE} = \frac{V_S * V_{SE}}{X_L} \sin(\delta - \rho) + \frac{V_R * V_{SE}}{X_L} \sin(\rho) + \frac{V_S * V_{SE}}{2X_C} \sin(\rho) \tag{38}$$

the reactive power that the series converter exchanges with the network:

$$Q_{SE} = \frac{V_S * V_{SE}}{X_L} \cos(\delta - \rho) - \frac{V_R * V_{SE}}{X_L} \cos(\rho) + \frac{V_{SE}^2}{X_L} - \frac{V_{SE}^2}{2X_C} - \frac{V_S * V_{SE}}{2X_C} \cos(\delta - \rho) \tag{39}$$

According to the figure 3, we can model the series converter active and reactive power with a negative resistance and a capacitor or inductive reactance, respectively. It means:

$$R = \frac{V_{SE}^2}{P_{SE}} \tag{40}$$

$$X = \frac{V_{SE}^2}{Q_{SE}} \tag{41}$$

Inserting equations 38 and 39 in equation 40 and 41, we can write:

$$R = \frac{V_{SE}}{\frac{V_S}{X_L} \sin(\delta - \rho) + \frac{V_R}{X_L} \sin \rho + \frac{V_S}{2X_C} \sin \rho} \tag{42}$$

$$X = \frac{V_{SE}}{\frac{V_S}{X_L}\cos(\delta-\rho) - \frac{V_R}{X_L}\cos\rho + \frac{V_{SE}}{X_L} - \frac{V_{SE}}{2X_C} - \frac{V_S}{2X_C}\cos(\delta-\rho)} \quad (43)$$

Using equations 24 and 25, the parallel reactance and resistance elements are converted to series elements and according to figure 6, the UPFC series converter in the exact line model, is modeled.

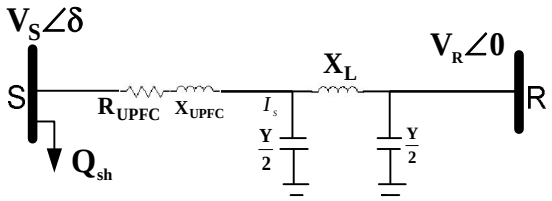

FIGURE 6: The UPFC series converter model in two-bus power system exact transmission model line

3. Simulation

In this section, we study the UPFC model based on circuitry elements in the 14- and 30-bus power system. Performing load flow using the Newton-Raphson method [7]in the 14- and 30-buses power system, the results of flowed power in the lines and voltage angle and amplitude of buses is calculated. The results are summarized in table 1-9.

Load flow results in 14-bus system without UPFC series converter

The results show that the bus number 5 has the lowest voltage and based on voltage, is a weak bus. Therefore we put UPFC converter as an example in line 1-5. By putting UPFC and changing the amplitude and angle of voltage injected by the series converter, the active and reactive power passing from line 1-5 will be controlled. The reactive power range is shown in figure 7 with respect to the active power. From this curve, it is obvious that using UPFC, we can change and control the active power in the range of 40 to 78 MW and reactive power between -8 to 42 MVAR.

bus number	bus voltage amplitude	bus voltage angle
1	1.06	0
2	1	-5.043
3	0.999	-13.362
4	.989	-11.428
5	.969	-9.151
6	1.02	-15.233
7	1.016	-14.628
8	1.05	-14.628
9	.998	-16.333
10	.998	-16.563
11	1.007	-16.095
12	1.012	-16.337
13	1.009	-16.526
14	.995	-17.72

TABLE 1: buses voltage amplitude and angle.

First bus	End bus	MW	MVAR
1	2	161	73.391
1	5	57.7	40.61
2	3	74.7	17.859
2	4	63.8	25.351
2	5	40.8	36.253
4	3	19.5	-7.468
4	7	27.4	-2.434
4	9	15.6	4.373
5	4	46.3	-24.413
5	6	44.5	8.218
6	11	7.7	7.208
6	12	7.77	3.345
6	13	17.8	9.045
7	9	27.4	16.563
8	7	0	21.284
9	10	4.72	0.712
9	14	8.89	1.102
11	10	4.27	5.193
12	13	1.68	1.569
13	14	6	4.303

TABLE 2: Active and reactive power lines without UPFC.

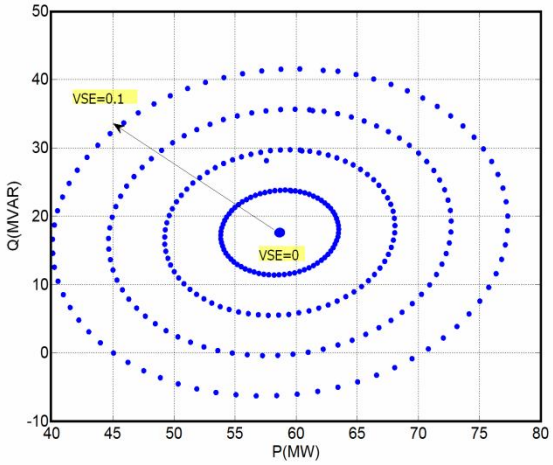

FIGURE 7: Changes in reactive power in terms of active power in line 1-5

For instance, we want the active power passing from line 1-5, to increase from 57.7 to 75.2 MW which is about 30 percent, and the reactive power of line 1-5 to decrease from 40.6 to 39.8 MVAR, which is around 1.7 percent. Therefore, assuming that the voltage amplitude injected by the series converter is fixed and equals to 0.1, using equations 38 and 39, we obtain the voltage phase angle of the series converter as follows:

$$V_{SE} = 0.1 \quad \text{and} \quad \rho = -130^{\circ}$$

Knowing the voltage phase and amplitude injected by the series converter, the resistance and reactance values that are equivalent to the series converter, is calculated using equations 24, 25, 42 and 43:

$$R_{UPFC} = -0.0028 \qquad \text{And} \qquad X_{UPFC} = -0.0975$$

Inserting the equivalent UPFC series converter resistance and reactance values in the line 1-5 and performing load flow calculations using Newton-Raphson method, the voltage and angle of buses and also the active and reactive power of lines can be calculated. The results are shown in tables 3 and 4.

Results of load flow with UPFC series converter in 14-bus power system

The results of tables 3 and 4 show that this model, like the other models of UPFC, is also able to control the active and reactive power of lines, stabilize the buses voltage and use the transmission lines in the optimized way. The flowed active and reactive power in line 1-5 is depicted in figures 8 and 9, with and without UPFC.

bus number	bus voltage amplitude	bus voltage angle
1	1.06	0
2	1	-4.476
3	0.999	-12.4
4	1.006	-10.155
5	1.007	-7.604
6	1.02	-13.583
7	1.024	-13.203
8	1.05	-13.203
9	1.006	-14.843
10	1.004	-15.041
11	1.01	-14.51
12	1.013	-14.698
13	1.01	-14.896
14	1	-16.156

TABLE 3: buses voltage amplitude and angle

First bus	End bus	MW	MVAR
1	2	143.00	65.939
1	5	75.615	30.761
2	3	71.173	12.748
2	4	57.794	8.887
2	5	32.342	6.467
4	3	23.027	3.563
4	7	26.786	3.373
4	9	15.349	6.799
5	4	54.968	2.282
5	6	45.565	28.477
6	11	8.384	5.31
6	12	7.861	3.066
6	13	18.12	8.068
7	9	26.786	17.204
8	7	0	15.662
9	10	4.116	2.564
9	14	8.519	2.322
11	10	4.884	3.322
12	13	1.761	1.291
13	14	6.381	3.057

TABLE 4: Active and reactive power lines with UPFC

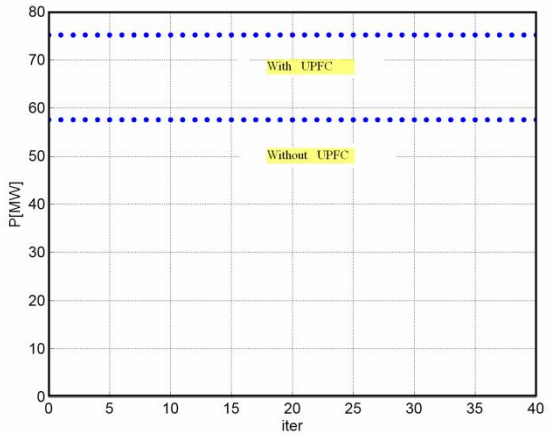

FIGURE 8: the curve of line 1-5 in active power with and without UPFC

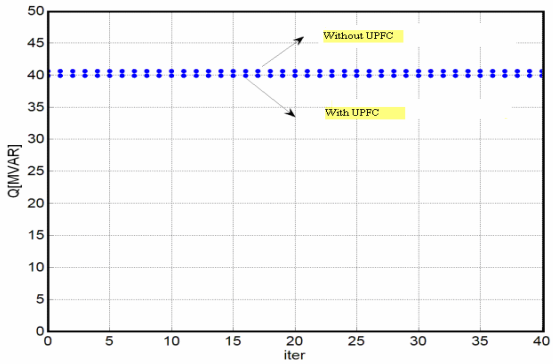

FIGURE 9: the curve of line 1-5 in active power with and without UPFC

In this system the load flow calculations are performed in the approximate transmission line model and its results are compared with the exact transmission line model. (See table 5)

	approximate model line	exact model line	percentage change
Voltage bus 5 (pu)	1.003	1.007	+0.39%
Active power line 1 - 5 (MW)	75.19	75.615	+0.56%
Reactive power line 1 - 5 (MVAR)	39.88	30.761	-22.86%

TABLE 5: changes of voltage and active and reactive power of line 1-5 with UPFC in approximation and exact transmission line model

Comparing the results, we conclude that the exact transmission line model yields more exact results. So, use of the exact transmission line model based on circuitry elements is preferred in comparison with the approximate model.
In the next section, the load flow calculations in 30-bus power system in presence of UPFC model in exact transmission line model will be investigated.

Results of load flow on 30–bus system without UPFC series converter

Performing the calculations of the load distribution, buses' voltage angles and amplitudes and also the active and reactive power passing from the lines are computed. The results for voltage and angle of buses number 2 and 5 and also the flowed power in line 2-5, are shown in tables 6 and 7.

bus number	bus voltage amplitude	bus voltage angle
2	1.043	-4.97
5	1.005	-13.54

TABLE 6: buses voltage amplitude and angle

First bus	End bus	MW	MVAR
2	5	78.7	25.2

TABLE 7: The active and reactive power line2-5 without UPFC

Results of load flow on 30–bus system in the presence of UPFC series converter

Using UPFC in line 2-5, we can control the passing active and reactive power from this line. Calculating the load flow by MATLAB software and use of Newton-Raphson method and for changes of voltage phase and amplitude injected by the series converter, the curve of reactive power changes has been plotted with respect to the active power in line 2-5 in figure 10

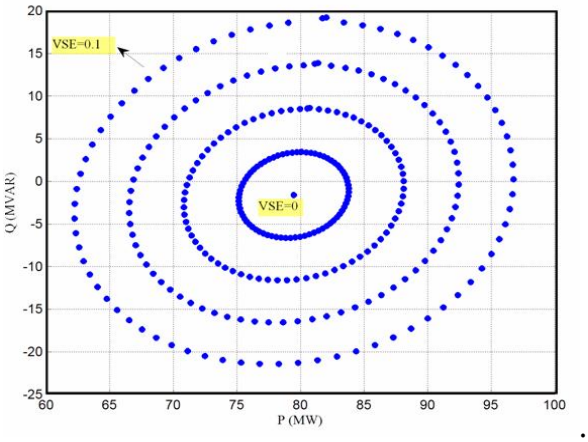

FIGURE 10: The reactive power changes in terms of active power in line 2-5

As this figure determines, by using the UPFC new model, the active power of line 2-5 of 30-bus power system can be controlled and changed between 63 to 97 MW and reactive power between -23 to 20 MVAR.

Therefore, for each value of voltage amplitude and phase of the series converter and using equations 24, 25, 42 and 43 the series converter equivalent resistance and reactance value will be calculated and used instead of the UPFC series converter . For example in work point:

$$V_{SE} = 0.1 \quad \text{and} \quad \rho = 80^{\circ}$$

The UPFC series converter equivalent series resistance and reactance values can be achieved as follows:

$$R_{UPFC} = -0.0016$$

And $X_{UPFC} = -0.077$

Putting the resistance and reactance values equivalent to the series converter and performing load flow, the results will be obtained according to tables 8 and 9.

bus number	bus voltage amplitude	bus voltage angle
2	1.043	-5
5	1.044	-11.1

TABLE 8: buses voltage amplitude and angle with UPFC

First bus	End bus	MW	MVAR
2	5	94.7	5.2

TABLE 9: The active and reactive power line2-5 with UPFC

Figures 11 and 12 show the curve for the active and reactive power passing from lines 2-5 with and without UPFC.

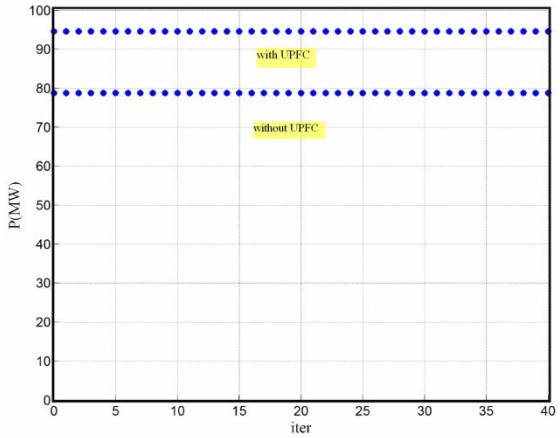

FIGURE 11: Active power curve passing line 2-5 in the presence and without UPFC

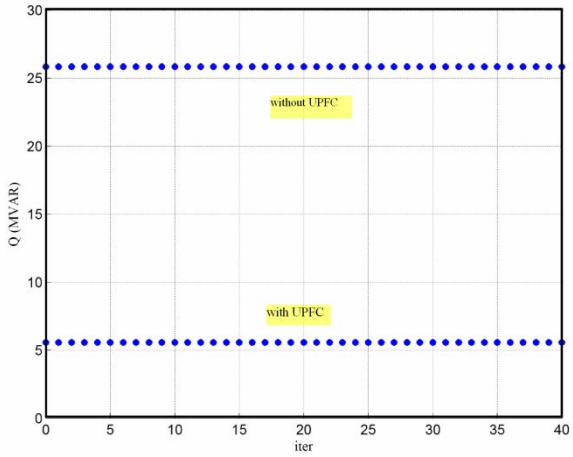

FIGURE 12: Reactive power curve passing line 2-5 in the presence and without UPFC

4. Conclusion

Considering the results of the simulation in figures 6 to 13 and tables 1 to 9, we can conclude:

- Like the other UPFC models, this model is also able to control the flowed power in transmission lines and as previously proved the results of this model and voltage injection model is the same. Therefore we can replace UPFC model on the basis of circuitry elements with other models.

- In this model a resistance is used instead of an injected active power, that the resistance value and polarity show the injected active power s value and direction; negative resistance shows the power injection and positive resistance shows the active power absorption.

- In this model instead of series converter reactive power, a capacitor or inductive reactance is used and its value indicates the rate of the reactive power. If the series converter injects reactive power into the network, the reactance will become capacitive (negative), and if the series converter absorbs reactive power from the network, the reactance will be inductive (positive).

- Unlike the previous models in which the active and reactive power of series converter could be modelled as connected power to bus and this leads to change of program structure and modification of Jacobian matrix, in this model the injected active and reactive power can be modelled with a resistance and reactance and in load flow programs only the network admittance matrix will change.

- Using the UPFC model based on circuitry elements in the exact transmission line model and adding the capacitors effects, yields more accurate load flow calculation results, so using the UPFC model in the exact transmission line model is preferred in comparison with the approximate model.

5. REFERENCES

1. N.G. Hingorani, Gyugyi. *"Understanding Facts"*. NewYork. IEEE.PRESS, pp. 1-300(2000)

2. M.H. Haque, and C. M. Yam. *"A simple method of solving the controlled load flow problem of a power system in the presence of UPFC"*. Elsevier Science, 65(1):55-62,2002

3. M. Noroozian, and M. Ghandhari. *"Use of UPFC for optimal power flow control"*, IEEE Transaction on Power Delivery,12 (4): 1629-1634 (1997)

4. M.H. Haque. *"Power flow control and voltage stabilitylimit:regulating transformer versus UPFC"*, IEEProc-Gener.Transm,151(3): 291-304 (2004)

5. M. Alomoush. *"Exact Pi-Model of UPFC-Inserted Transmission Lines in Power Flow Studies"*, IEEE Trans,22(1): 54-56 (2002)

6. H.L. Sheng, and C. ChiChu. *"Comprehensive UPFC Models for Power Flow Calculations in Practical Power Systems"*, IEEE Trans,1 (1): 27-32 (2000)

7. C.R. Fuerte-Esquivel. and H.Ambriz.*" A Comprehensive Newton- Raphson UPFC Model for the Quadratic Power Flow Sloution of Pratical Power Networks"*, IEEE Transaction on Power Systems, 15 (1): 102-109 (2000)

Vibration Attenuation of a Thin Cantilevered Beam Using LQG-Based Controller and Inertial Actuator

A. H. El-Sinawi aelsinawi@aus.edu
Associate Professor
Department of Mechanical Engineering
American University of Sharjah,
Sharjah, UAE, P.O. Box 26666

Abstract

This study considers the problem of attenuating the vibration at a certain location on a flexible cantilevered beam mounted on a vibrating base which is the tip in this case. Attenuation is achieved without the need for sensor placement at that location. A modal state-space model of the flexible beam is constructed from the beam's first ten modes of vibration. A reduced-order optimal observer is utilized to estimate the deflection of the beam's tip from measurements of vertical deflections at mid-span and actuator locations. An inertial actuator is mounted on the beam itself, provides the control effort necessary for attenuating the tip vibration, resulting from shaker excitation. Experimental and simulation results have demonstrated the effectiveness of the proposed control technique.

Keywords: Inertial actuator, optimal control, LQG, estimation, cantilevered beam, modal analysis.

NOTATION

$\mathbf{A}$	dynamics matrix of full order modal model
$\mathbf{A}_c$	dynamics matrix of the controller
$\mathbf{A}_\mathbf{r}$	dynamics matrix of reduced-order modal model
$\mathbf{A}_a$	dynamics matrix of augmented system
b	actuator damping coefficient
$\boldsymbol{B}_f$	input vector of transmitted force
$\mathbf{B}_\mathbf{m}$	input matrix of full order modal model
$\mathbf{B}_\mathbf{r}$	input matrix of reduced-order modal model
$\mathbf{B}_\mathbf{rc}$	control distribution modal matrix
$\mathbf{B}_\mathbf{c}$	controller input vector
$\mathbf{C}_c$	controller output matrix
$\mathbf{C}_\mathbf{md}$	modal displacement output matrix
$\mathbf{C}_\mathbf{mv}$	modal rate output matrix
$\mathbf{C}_\mathbf{r}$	output matrix of reduced-order system

$\mathbf{D}$	nodal damping matrix
$\mathbf{D}_{ur}$	reduced-order feed through matrix
$\boldsymbol{e}_2$	model reduction error
F_i	Excitation force from the shaker (support)
F_c	actuator control force
G_c	Actuator transfer function
G_r	transfer function of reduced model
$\mathbf{I}$	identity matrix
J	quadratic cost performance index
k	actuator stiffness
$\mathbf{K}$	nodal stiffness matrix
$\mathbf{K}_\mathbf{c}$	controller modal Matrix of gains
$\mathbf{L}$	Estimator gain matrix
$\mathbf{M}$	nodal mass matrix
m	number of actuators
m_o	mass of inertial actuator
n	dimension of nodal model
N	dimension of modal model
N_r	dimension of reduced order modal model
p	number of sensors
$\mathbf{P}_\mathbf{c}$	solution of the controller algebraic Riccati equation
$\mathbf{P}_\mathbf{e}$	solution of the estimator algebraic Riccati equation
$\mathbf{Q}$	Controller weighting matrix
$\boldsymbol{q}$	vector of nodal displacements
$\mathbf{R}$	controller weighting matrix
s	Laplace variable
t	time
u	input to transmitted force model
$\mathbf{U}_\mathbf{c}$	control law
$\mathbf{V}$	estimator weighting matrix
v	measurements noise
$\boldsymbol{w}$	vector of external inputs
$\mathbf{W}$	estimator weighting matrix
$\mathbf{W}_\mathbf{c}$	controllability grammian
$\mathbf{W}_\mathbf{o}$	observablility grammian
$y(t)$	displacement at actuator location
$\boldsymbol{Y}_r$	nodal output vector of reduced model
$\boldsymbol{Y}_s$	nodal output vector of full model
$\boldsymbol{z}$	modal states
$\boldsymbol{\Delta}$	modal damping matrix
$\boldsymbol{\eta}, \dot{\boldsymbol{\eta}}$	modal displacement and velocity vectors
$\boldsymbol{\Phi}$	matrix of eigenvectors

Ω diagonal matrix of eigenvalues

1. INTRODUCTION

Accuracy of the model of a flexible structure plays a major role in the design of an appropriate control system that will force the structure to perform certain tasks or attenuate structural vibration. Flexible structures are inherently distributed parameter structures with infinite degrees of freedom. A model of such structure will have to be a reduced order model but adequate enough to yield a controller that will carry out the necessary manipulation and/or vibration attenuation.

Research efforts in this field have provided a wealth of techniques for modeling and control of flexible structures. Once the model is constructed, the accuracy and precision of control systems, needed to manipulate the structure, or to perform certain tasks, depends solely on the accuracy of the structure's model. Since, models of flexible structures are reduced order, the control scheme has to either, focus on certain dynamic characteristics and try to control the structure based on the available model, or it has the ability to somewhat estimate or predict the un accounted for dynamics. In either case, the model and the controller will have limited ability in predicting the actual structural behavior **[1].** As it is known, any active control scheme must keep track of the behavior of the physical system in order to adjust its effort to suite the current status of the structure and perform the predefined requirements on that structure. This also poses another problem in large flexible structures, since sensor placement on large flexible structures increases the complexity of both the model and the controller. Therefore, to actively control a flexible structure, one has to keep in mind all the aforementioned challenges.

From modeling standpoint, many research efforts have utilized FEM to obtain models of flexible structures that can be used for control purposes. However, modal models obtained by FEM are not sufficient for providing a reliable model for control purposes for many reasons, one of which is that, FEM provides no information about damping in the structure **[1].** This aspect is crucial to the model since damping dictates the transient behavior of the structure as well as the phase of the control effort in relation to structural vibration.

In modeling of flexible structures, FEM technique is widely used for constructing analytical models of flexible structures. This method is well established but may not be accurate for controller design due to drawbacks mentioned above **[2, 3].** Another approach for modeling flexible systems is to determine the model directly from experimental data, such as experimental modal analysis [**2**]. Analytical methods have also been used to obtain working models for flexible structures **[4-6].**

As for the control of flexible structures, considerable research has been done in this field with various approaches and techniques. A common form of vibration control of flexible structure is done using passive means such as using viscoelastic materials, and passive damping **[7, 8].** Other control approaches utilize various forms of feedback control techniques to achieve certain manipulation, attenuation, suppression or isolation requirements **[9-13].** Other techniques involve robust control, optimal and fuzzy control **[14-19]**. Control techniques of flexible structures focus mainly on improving the agility, efficiency and bandwidth of the controller in the presence of noise as well as modeling and excitation uncertainties. A comprehensive review of shape control of flexible

structures with emphasis on smart structures using piezoelectric actuators is presented by **[20, 21].**

In this work, vibration attenuation of the tip of a cantilevered beam subjected to excitation at the support is presented. A novel control technique uses a non-collocated sensors and actuators to attenuate the vibration at the beam's tip. The control effort is determine by an LQG-based controller that uses feedback measurements at locations other than the tip to determine the required control force needed to attenuate the vibration at the tip. A non-reactive actuator (i.e. inertial actuator) is mounted close to the support and used to apply an appropriate control force to attenuate the tip vibration. The sensor-actuator non-collocation is utilized in this work to accommodate situations where sensor placement at the control location is prohibitive. Inertial actuators react directly off a mass; therefore, they can be placed directly on the vibrating structure without the need for a reactive base **[11, 12, 22]**. LQG is utilized to estimate the control effort needed without the need for sensor placement at the control location. LQG-based controller reduces computational cost and provides robustness in the presence of model uncertainties as well as measurements and excitation noise. Dynamic modal model of the flexible structure is constructed from the first ten modes of vibration obtained via finite element analysis of the structure. To improve the agility of the controller and reduce its sensitivity, the proposed control technique uses a reduced order modal model of the structure. The latter eliminates the least effective modes of vibration at the control location, i.e., modes with the least H_2 norms are truncated from the modal model [**23].** Both simulation and experiments are carried out to verify the integrity of the proposed control technique.

2. CONTROL STRATEGY DESCRIPTION

In the following sections, the linear quadratic Gaussian (LQG) based controller is constructed. The LQG has two parts, namely, an optimal observer, and an optimal controller. The observer generates estimates of the vertical nodal displacement of three locations on the beam, which are the actuator location, mid-span, and the beam tip. The controller output is a control force lateral to the beam axis. As for the inputs, the observer is subject to all external inputs that the actual beam is subject to. Those inputs are the force applied to the beam at the support F_i, and the vertical control force F_c. Moreover, optimal observers in general require feedback of errors between state estimates and state measurements.

The demand on LQG is to reduce the vibration of the beam tip. To fulfill this demand, the LQG has to perform the two nearly-simultaneous tasks of, (a) producing optimal estimates of the vibration at three locations along the beam's span and (b) generating a control vector that will drive the inertial actuator to minimize the force transmitted to the tip and subsequently reduce its vibration.

3. INERTIAL ACTUATOR

To better explain the control scheme proposed by this study. The layout of the dynamic system is shown in Figure (1-a). In Figure (1-b) a free body diagram of the beam is shown where the inertial actuator is applying force F_c to cancel out the effect of force F_i on the section of the beam to the right of the inertial actuator. The actuator is particularly

targeting the attenuation of the vibration at the tip through transferring a force to the beam with required magnitude and phase such that the tip's vibration is minimized. Modeling the actuator as a spring mass damper system, the transmitted force from actuator to the beam can be expressed in the form

$$-m_o \ddot{z} = F_c \tag{1}$$

where m_o is the mass of the actuator and z is the actuator's mass displacement. Therefore,

$$F_c = c(\dot{z} - \dot{y}) + k(z - y) \tag{2}$$

where y is the displacement of the beam at the actuator's location. Assuming that the ultimate objective of the controller is to nullify the displacement of the actuator mass relative to the beam (i.e., $z = 0$), will yield an a required actuator force of the form,

$$F_C = c(-\dot{y}) + k(-y) \tag{3}$$

With an actuator stiffness that is relatively large compared to the stiffness of the beam, and assuming only natural damping in the beam and actuator, the force acting on the actuator mass will vanish only if the vibration of the beam at the actuator location vanishes. However, since the purpose of the control is to eliminate the vibration at the beam tip not the actuator location, the controller will assume the actuator's mass vibration is indirectly caused by the vibration of the tip, and therefore, must keep track of the tip's vibration despite the fact that physical measurements at that tip are inaccessible. Therefore, if estimates of the tip vibration is fed to the actuator, the result will be a control force that will minimize the tip vibration with F_c in Equation (3) replaced by

$$F_C = c(-\dot{\hat{y}}_t) + k(-\hat{y}_t) \tag{4}$$

Where $\hat{y}_t$ is the estimate of the tip's vibration and the transfer function mapping the tip's displacement estimates to the control force is,

$$G(s) = \frac{F_s(s)}{\hat{Y}_t(s)} = -(bs + k). \tag{5}$$

this resembles a PD controller with proportional and derivative gains equal to the stiffness and damping of the actuator, respectively.

It is clear, that actual implementation of the inertial actuator will cause the dynamics of the latter to be part of the overall dynamics of the system. Therefore, actuator dynamics will be later on augmented with those of the structure (i.e., beam) during the design of the LQG-based controller.

4. STATE-SPACE REPRESENTATION OF THE BEAM

To implement the proposed concept of controlling the tip vibration using inertial actuator, a state-space model is formulated, in this case, for a distributed parameter system such as the beam shown in Figure (1). The beam is considered as an *n*-dimensional model of a modally damped flexible structure having (*m*) actuators and (*p*) sensors, not necessarily collocated. The beam system retrofitted with an actuator is shown in Figure

(1). The beam's structure is represented in nodal coordinates by the following second-order matrix differential equation:

$$\mathbf{M}\ddot{\boldsymbol{q}} + \mathbf{D}\dot{\boldsymbol{q}} + \mathbf{K}\boldsymbol{q} = \mathbf{B}\boldsymbol{w} \tag{6.a}$$

$$\boldsymbol{Y}_s = \mathbf{C}_{\mathbf{d}}\boldsymbol{q} + \mathbf{C}_{\mathbf{v}}\dot{\boldsymbol{q}} \tag{6.b}$$

In the above equation $\boldsymbol{q}$ is the $n \times 1$ displacement vector, $\boldsymbol{w}$ is the $m \times 1$ external input vector, $\boldsymbol{Y}_s$ is the $p \times 1$ nodal output vector, $\mathbf{M}$, $\boldsymbol{D}$, and $\mathbf{K}$ are the $n \times n$ mass, damping, and stiffness matrices, respectively. $\mathbf{C}_{\mathbf{d}}$, and $\mathbf{C}_{\mathbf{v}}$ are respectively, the $p \times n$ output displacement and output velocity matrices. The mass matrix is positive definite and the stiffness and damping matrices are positive semidefinite. The damping matrix $\mathbf{D}$ is assumed to be proportional to the stiffness matrix $\mathbf{K}$ without any significant effect on the integrity of the model [**23, 24**]. Dynamic model such as the one shown in Equation (6) is usually obtained from finite-element codes and has the dimension *n* which is unacceptably high to use in producing a state-space model suitable for structural control. Therefore an alternative approach is to use an *N*-dimensional second-order modal model of the system where $N << n$.

A second order modal-model of the system can be expressed as

$$\ddot{\boldsymbol{\eta}} + 2\boldsymbol{\Delta}\boldsymbol{\Omega}\dot{\boldsymbol{\eta}} + \boldsymbol{\Omega}^2\boldsymbol{\eta} = \mathbf{B}_{\mathbf{m}}\boldsymbol{w}(t) \tag{7.a}$$

$$\boldsymbol{Y}_s = \mathbf{C}_{\mathbf{md}}\boldsymbol{\eta} + \mathbf{C}_{\mathbf{mv}}\dot{\boldsymbol{\eta}} \tag{7.b}$$

where $\boldsymbol{\eta} = \boldsymbol{\Phi}\boldsymbol{q}$, and $\boldsymbol{\Phi}$ is the $n \times N$ modal matrix, $\boldsymbol{\Omega}$ is the $N \times N$ diagonal matrix of modal natural frequencies, $\boldsymbol{\Delta}$ is the $N \times N$ modal damping matrix, $\mathbf{B}_{\mathbf{m}}$ is the $N \times m$ modal input matrix, $\mathbf{C}_{\mathbf{md}}$ and $\mathbf{C}_{\mathbf{mv}}$ are the $p \times N$ modal displacement and rate matrices, respectively. Defining the state vector $\boldsymbol{z} = \begin{bmatrix} \boldsymbol{z}_1 & \boldsymbol{z}_2 \end{bmatrix}^T = \begin{bmatrix} \boldsymbol{\eta} & \dot{\boldsymbol{\eta}} \end{bmatrix}^T$, a flexible structures having point force(s) as the input(s) and point displacement(s) as outputs will have the state space representation,

$$\dot{\boldsymbol{z}} = \begin{bmatrix} \mathbf{0} & \mathbf{I} \\ -\boldsymbol{\Omega}^2 & -2\boldsymbol{\Delta}\boldsymbol{\Omega} \end{bmatrix}\boldsymbol{z} + \begin{bmatrix} 0 \\ \mathbf{B}_{\mathbf{m}} \end{bmatrix}\boldsymbol{w} \tag{8.a}$$

$$\boldsymbol{Y}_s = \begin{bmatrix} \mathbf{C}_{\mathbf{md}} & \mathbf{0} \end{bmatrix}\boldsymbol{z} + \mathbf{D}_{\mathbf{u}}\,\boldsymbol{u} \tag{8.b}$$

where, $Y_s(t)$ and $w(t)$ are the nodal output and input vectors, respectively. Matrix $\mathbf{D}_{\mathbf{u}}$ is the $p \times m$ feed through matrix. Equation (8) can also be represented by the following compact form,

$$\dot{\boldsymbol{z}} = \mathbf{A}(\theta)\boldsymbol{z} + \mathbf{B}(\theta)\boldsymbol{w} \tag{9.a}$$

$$\boldsymbol{Y}_s = \mathbf{C}(\theta)\boldsymbol{z} + \mathbf{D}_{\mathbf{u}}(\theta)\boldsymbol{w} \tag{9.b}$$

where $\mathbf{A}$, $\mathbf{B}$, $\mathbf{C}$, and $\mathbf{D}_{\mathbf{u}}$ matrices are functions of the system (natural frequency, damping ratio, and mode shapes (i.e., $\theta = f\left(\omega_i, \zeta_i, \text{ and } \phi_i\right)_{i=1\Lambda\, N}$) . The dimension of this state-space representation is $2N$ and it is much more manageable than the $2n$ state-space model obtained from the corresponding nodal model. Detailed information

on constructing state-space model from natural frequencies and mode shapes is given in [**15, 23**].

5. MODEL REDUCTION

To show the effectiveness of the proposed control strategy, the $2N$-dimension state space model of the beam-hub system constructed in Equation (9) will be reduced even further to a $2N_r$-dimension state-space representation. This will reduce the computational cost and further validate the effectiveness of the proposed technique. In this study the reduction is based on retaining only half the number of modes (i.e., $N_r = (N/2)$) and the modes retained will be those with the largest H_2 norm [**25**]. In such case, the H_2 reduction error is expressed as:

$$e_2 = \left\| G - G_r \right\|_2 \tag{10}$$

where G is assumed to be the transfer function of the full model corresponding to equation (9), and G_r is the transfer function of the reduced model. The square of the mode norms are additive [**25**], therefore the norm of the reduced system with N_r modes is the root-mean-square sum of the mode norms

$$\left\| G_r \right\|_2^2 = \sum_{j}^{N_r} \left\| G_j \right\|_2^2 \tag{11}$$

and the reduction error is,

$$e_2^2 = \left\| G \right\|_2^2 - \left\| G_r \right\|_2^2 = \sum_{j=N_r+1}^{N} \left\| G_i \right\|_2^2 \tag{12}$$

The term $\left\| G_i \right\|_2$ is the modal cost of Skelton [**26**], which for the *j*th mode has the form

$$\left\| G_j \right\|_2 \cong \frac{\left\| B_j \right\|_2 \left\| C_j \right\|_2}{2\sqrt{\xi_j \omega_j}} \tag{13}$$

It can be seen from Equation (12) that near optimal reduction is attained if the truncated mode norms for $j = N_r + 1, \Lambda\ N$ are the smallest. It should be noted that after truncation, modes should be rearranged such that the reduced model has a modal natural frequency $\Omega_f = diag[\omega_1, \Lambda\ \omega_k]$ where, ω_1 has the highest H_2 norm. *This also implies rearranging the corresponding modal states as well*. The new state space representation of the truncated system is:

$$\dot{\mathbf{z}} = \mathbf{A_r}(\theta)\mathbf{z} + \mathbf{B_r}(\theta)\mathbf{w} \tag{14.a}$$

$$\mathbf{Y_r} = \mathbf{C_r}(\theta)\mathbf{z} + \mathbf{D_{ur}}(\theta)\mathbf{w} \tag{14.b}$$

where the subscript r denotes a reduced –order model. This state-space model has the dimension $2N_r$.

6. AUGMENTATION OF THE CONTROLLR WITH THE STRUCTURE

As it was mentioned in the Section (3) above, the dynamics of the actuator must be augmented with the dynamics of the beam because the actuator will e mounted on the beam itself. The augmented system will have the following state-space matrices,

$$A_a = \begin{bmatrix} A_c & 0 \\ B_r C_c & A_r \end{bmatrix}, B_a = \begin{bmatrix} B_c \\ B_r \times D_c \end{bmatrix}, C_a = \begin{bmatrix} D_{ur} \times C_c & C_r \end{bmatrix}, \text{and } D_a = [D_{ur} \times D_c] \tag{15}$$

Where A_c, B_c, C_c, D_c, are the state space matrices of the controller given in Equation (5). Notice that the transfer function in Equation (5) is unrealizable at its current state, but it can be with a second order filter in the denominator assuming that measurements of acceleration rather than displacement are to be fed to the actuator; see **[15]** for details.

7. OPTIMAL OBSERVER-CONTROLLER SYNTHESIS

In this section, the optimal observer-controller is formulated. The formulation is based on the augmented model of Equation (15). Measurements of the beam's acceleration in the vertical direction are assumed to be available at actuator location and at beam's mid-span. The beam support is assumed to be mounted on a shaker the cause the excitation at the support. The optimal observer-controller will be an LQG type for which the plant is described as follows:

$$\dot{z} = \mathbf{A}_a z + \mathbf{B}_{rc} \mathbf{U}_\mathbf{c} + \mathbf{B}_a w \tag{16.a}$$

$$Y_a = \mathbf{C}_a z + \mathrm{v} \tag{16.b}$$

The plant model of equation (19) is perturbed by the external input w, and the output Y_a is corrupted with noise v. The term D_{ur} is dropped because the denominator of Equation (5) has been replaced by the second order filter. The optimal control problem is formulated by finding the linear quadratic regulator (LQR) gains and the Kalman estimator gains that will minimize a quadratic performance index,

$$J = \int_0^\infty (\mathbf{z}^T \mathbf{Q} \mathbf{z} + \mathbf{U_c}^T \mathbf{R} \mathbf{U_c}) dt \tag{17}$$

The estimator dynamics are given by the following state-space matrix differential equation

$$\dot{\hat{z}} = \mathbf{A}_a \hat{z} + \mathbf{B}_{rc} U_c + \mathbf{L}(Y_r - \mathbf{C}_a \hat{z}) + B_a w \tag{18.a}$$

$$\hat{Y}_a = \mathbf{C}_a \hat{z} \tag{18.b}$$

Here $\hat{z}$ is the vector of estimated modal states, B_{rc} is the modal feedback control distribution matrix, and $\boldsymbol{U}_\mathbf{c} = -\mathbf{K}_\mathbf{c} \hat{\boldsymbol{z}}$, where K_c, and L are respectively, the LQR and Kalman gains. The feedback gain vector $\mathbf{K_c}$ is give by

$$\mathbf{K_c} = \mathbf{R}^{-1} \mathbf{B}_{rc}^\mathbf{T} \mathbf{P_c} \tag{19}$$

where $\mathbf{P_c}$ is the solution of the controller algebraic Riccati equation

$$\mathbf{A}_a{}^{\mathbf{T}}\mathbf{P_c} + \mathbf{P_c}\mathbf{A}_a - \mathbf{P_c}\mathbf{B}_{rc}\mathbf{R}^{-1}\mathbf{B}_{rc}^{\mathbf{T}}\mathbf{P_c} + \mathbf{Q} = \mathbf{0}, \tag{20}$$

and the estimator gain matrix $\mathbf{L}$ is given by

$$\mathbf{L} = \mathbf{P_e}\mathbf{C}_a^{\mathbf{T}}\mathbf{V}^{-1} \tag{21}$$

where $\mathbf{P_e}$ is the solution of the estimator algebraic Riccati equation

$$\mathbf{A}_a\mathbf{P_e} + \mathbf{P_e}\mathbf{A}_a{}^{\mathbf{T}} - \mathbf{P_e}\mathbf{C}_a{}^{\mathbf{T}}\mathbf{V}^{-1}\mathbf{C}_a\mathbf{P_e} + \mathbf{B}_a\mathbf{W}\mathbf{B}_a{}^{\mathbf{T}} = \mathbf{0} \tag{22}$$

In this study, Equation (18) produces the vector $\hat{Y}_a = \begin{bmatrix}\hat{q}_c & \hat{q}_{tip} & \hat{q}_{mid-span} & \hat{q}_{act\_location}\end{bmatrix}^T$ where, q_c are the controller states. It should be noted that the matrix $\mathbf{K_c}$ is the LQR modal gains and the portion of $\hat{Y}_a$ namely; $\begin{bmatrix}\hat{q}_{tip} & \hat{q}_{mid-span} & \hat{q}_{act\_location}\end{bmatrix}^T$ is the vector of beam's nodal displacements, and thus, before utilizing the optimal feedback, this portion has to be transformed back to the modal domain using the modal matrix $\mathbf{\Phi}$. Matrices $\mathbf{R}$ and $\mathbf{V}$ are positive definite while matrices $\mathbf{Q}$ and $\mathbf{W}$ are positive semidefinite. The latter four matrices can be treated both as weighting matrices and as tuning parameters for the LQG [**26, 27**].

In this study it is assumed beforehand that q_{tip} is not available for measurements, therefore, no estimate error for this state is available for feedback. However, estimate errors for the actuator location and the mid-span states are available and must be fedback to the estimator through the Kalman matrix of gains $\mathbf{L}$. This implies that poles of the closed loop system depicted by Equation (18) are placed in such manners that only optimal LQG estimates of actuator location and mid-span displacements are obtained. This is a major deficiency and it will cause an arbitrary change in the tip state due to the lack of information available to the estimator about measured tip displacements. Such estimator will not be of much use if the tip deflection is to be controlled. Therefore, the last term of equation (18) (i.e., $\mathbf{B}_a w$) is utilized to both eliminate this deficiency and achieve the demand on the LQG. In other words, the term $B_a w$ will have to enable the LQG to (a) force subsequent estimates of tip modal states (i.e., $\hat{z}$) to be dependent on previous estimates of tip deflection and (b) generate a control force that will minimize the difference between the actuator mass and tip deflections through manipulation of the actuator location only. If the inertial actuator utilized to generates a force that is a function of the difference between the actuator mass displacement (i.e., zero in this case based on the reasoning in Equations (3-5)) and tip deflections, then equation (18) will have $w = \begin{bmatrix}F_i & F_c\end{bmatrix}^T$ where, F_i *and* F_c are the excitation and control forces, respectively. we obtain,

$$\mathrm{F}_i = C_c(\mathbf{sI} - \mathbf{A}_c)^{-1}B_c(0 - \hat{\mathrm{q}}_{act\_location}), \tag{26}$$

where s is the Laplace variable, $\mathbf{I}$ is a 2×2 identity matrix.

For effective implementation of the proposed control strategy it is important to determine early on whether the system is controllable (i.e., actuators excite all modes) and observable (i.e., the sensors detect the motion of all modes). It is clear, however, that

the proposed control strategy may very well have a value of N large enough to prohibit accurate calculation of the controllability and observability matrices of the system. To avoid such problem, the controllability and observability grammians are used instead of the original method proposed by Kalman [**22, 23**]. The grammians are determined from the following Lyapunov equations:

$$\begin{aligned} &\mathbf{A}\mathbf{W}_c + \mathbf{W}_c\mathbf{A}^T + \mathbf{B}\mathbf{B}^T = \mathbf{0}, \\ &\mathbf{A}^T\mathbf{W}_o + \mathbf{W}_o\mathbf{A} + \mathbf{C}\mathbf{C}^T = \mathbf{0} \end{aligned} \tag{30}$$

where $\mathbf{A}$, $\mathbf{B}$, and $\mathbf{C}$, are the dynamic , input, output matrices of the overall model of the system, respectively. Matrices $\mathbf{W}_c$ and $\mathbf{W}_o$ are, respectively, the controllability and observability grammians. The system is controllable and observable if $\mathbf{W}_c = \mathbf{W}_c^T$, and $\mathbf{W}_o = \mathbf{W}_o^T$. The synthesized controller is implemented and the results are presented in the next section.

8. EXPERIMENTAL AND NUMERICAL SIMULATION RESULTS

Vibration attenuation of the beam tip of Figure (1) is investigated. The beam-actuator system is subject to excitation shown in Figure (2) exerted on the beam's support. Dimensions and properties of the system under study are listed in Table 1. Actual behavior of the beam-actuator is constructed based on the first ten modes of vibration of the beam-actuator system for which the modal frequencies and modal norms are listed in Table (2). The reduced-order dynamics model used in the design of LQG is constructed from four modes only. The four modes are those with the largest H_2 norms as shown in Table 2, namely, modes 1, 2, 3, and 5. The reduced order model of the system is constructed from those four modes and the states are arranged according to the same sequence.

Using four modes of vibration to synthesize the LQG-based controller indicates that exact knowledge of the dynamics of the system is not necessary for successful implementation of the controller; rather a carefully reduced-order model is sufficient. The controller and estimator gain matrices, K_c, and *L* are generated in Matlab using weighting matrices $\mathbf{Q} = \alpha\mathbf{I}_{10\times10}$, $\mathbf{R} = \mathbf{I}_{2\times2}$, $\mathbf{V} = 10\times\mathbf{I}_{2\times2}$, and $\mathbf{W} = \mathbf{I}_{3\times3}$, $\alpha = 100$. Modal damping of 0.01 is used for all modes of vibration. Notice that the two extra states in K_c, and *L* belong to the controller as shown by Equation (15).

The control effort is tuned to reduce the relative vibration between the beam's tip and the actuator mass via (1) feedback of two error signals; which are the difference between measured and estimated displacements at actuator location and mid-span, which are used to produce better estimates of deflections including that of the tip. And (2) estimates of the tip deflection, are fed through the inertial actuator with a demand to produce the control effort necessary to reduce the tip vibration. Block diagram of the control scheme used in this simulation is shown in Figure (3).

The ideal outcome of the control strategy is to reduce the estimates of the beam tip vibration to zero. Figures 4 and 5 show significant reduction in the vibration both at the tip, and at the actuator location. Figure 6 shows the control force needed to achieve the attenuation and it is within the capabilities of the actuator.

To verify simulation outcomes, experiments are carried out under conditions identical to those used in the simulation. The experimental setup shown in Figure 7 is utilized to verify the integrity of the proposed technique. Significant reduction in the magnitude of the transfer function (approximately 30% at resonant frequencies) is attained as shown in Figure 8. No abnormal vibration is created at the actuator location when the controller is targeting the tip vibration as shown in Figure 9. Experimental actuator force is shown in Figure 10 which is reasonable and within the capabilities of the actuator used.

It should be pointed out that this control technique has draw backs mostly in its sensitivity to excitation changes, mass of the inertial actuator, and overestimates of the force which appear to be related to the choice of values for the weighting matrices of the controller and observer as well as the derivative term in the transfer function of Equation (5).

9. CONCLUSIONS

A novel approach for attenuating the vibration of a cantilevered beam mounted on a vibrating base has been presented. The proposed technique is particularly useful considering the fact that, real-life systems exhibits considerable variations in their properties. Thus, the characteristics of a structure corresponding to these properties show some stochastic variations. This makes it necessary to take into account the uncertainties of the system if a reliable control system is to be implemented. To this purpose, a robust and effective control system using optimal estimation and control techniques would be a suitable choice. The control strategy uses available measurements at various locations on a flexible structure to produce estimates of the vibration at inaccessible locations. Latter estimates are then used to control the vibration at those inaccessible locations using inertial actuator. The inertial actuator is non-collocated with the sensors, and can be mounted directly on the structure, providing flexibility in locating sensors and actuators according to needs and constraints.
Experimental and simulation results of the proposed method show significant reduction in the tip vibration without the need for any sensor(s) placement at the control location (the tip in this case). This is an important feature which could prove useful in applications where use of sensory devices at any location on the flexible structure is difficult to attain. The proposed strategy managed to reduce the vibration of the beam's tip by approximately 30% at resonant frequencies using only estimates of the tip vibration rather than actual measurements.
Fine tuning of the weighting matrices should be carried to obtain the optimal results for the control force and the reduction in the tip vibration. Further work is needed in the implementation of this technique and two and three dimensions where the processes can be duplicated for the other two dimensions that were not discussed by this work.

ACKNOWLEDGMENT

The author acknowledges the support of American University of Sharjah.

REFERENCES

[1]. J. Dosch, D. Leo, and D. Inman. "*Modeling and control for vibration suppression of a flexible active structure*". Journal of Guidance Control and Dynamics, 18(2): 340-346, 1995
[2]. J. N. Juang and R. S. Pappa. "*An eigensystem realization algorithm for modal*

parameter identification and model reduction (control systems design for large space structures)" . Journal of Guidance, Control, and Dynamics, 8: 620-627, 1985

[3]. Gawronski, W. and Williams, T. "*Modal reduction for flexible space structures*". Journal of Guidance, 4: 68–76, 1991

[4]. Y-R Hu and Alfred Ng. "*Active robust vibration control of flexible structures*". Journal of Sound and Vibration, 288: 43-56, 2005

[5]. J-H Han, K-H Rew and I. Lee. "*An experimental study of active vibration control of composite structures with a piezo-ceramic actuator and a piezo-film sensor*". Smart Materials and Structures, 6: 549-558, 1997

[6]. M. J. Balas. "*Active control of flexible systems"*. Journal of Optimization Theory and Applications, 25 (3): 415-436, 1978

[7]. Yen, H-Y. and Shen, M. H. "*Passive vibration suppression of a beam and blades using magneto-mechanical coating*". Journal of Sound and Vibration, 245(4): 701-714, 2001

[8]. Griffin, J. H. "*Friction damping resonant stresses in gas turbine engine airfoil*". International Journal of Turbo and Jet Engines, 7, pp. 297-307, 1999

[9]. H.A. Malki, M. D. Feigenspan, and D. G. Chen. "*Fuzzy PID control of a flexible-joint robot arm with uncertainties from time-varying loads*". IEEE Transactions on Control Systems Technology, 5(3): 371-378. 1997

[10]. Krodkiewski, J. M. and Faragher, J. S. "*Stabilization of motion of Helicopter rotor blades using delayed feedback-modeling, computer simulation and experimental verification*". Journal of Sound and Vibration, 234(4): 591-610, 2000

[11]. L. Benassi and S.J. Elliott. "*Active vibration isolation using an inertial actuator with local displacement feedback control*". Journal of Sound and Vibration, 278: 705–724, 2004

[12]. L. Benassi and S.J. Elliott. "*Global control of a vibrating plate using a feedback-controlled inertial actuator*". Journal of Sound and Vibration, 283: 69-90, 2005

[13]. N. Hogan. "*Impedance control: An approach to manipulation*". Journal of Dynamic Systems Measurement and Control, 107: 8-16, 1985

[14]. A. H. El-Sinawi. "*Vibration attenuation of a flexible beam mounted on a rotating compliant hub*". I-*Mech, Part I, Journal of Systems and Control Engineering*, 218:121-135, 2004

[15]. El-Sinawi, A. H. and Hamdan, M. N. "*Optimal vibration estimation of a non-linear flexible beam mounted on a rotating compliant hub*". Journal of Sound and Vibration, 259(4), pp. 857-872, 2003

[16]. El-Sinawi, A. H. and Kashani, A. R. "*Active isolation using a Kalman estimator-based controller*". Journal of Vibration and Control, 7: 1163–1173, 2001

[17]. M. R. Serbyn. "*Active control of cantilever-beam vibration*". Journal of Acoustical Society of America*,* 112 (5)5: 2246-2247*,* 2002

[18]. J. J. Dosch, G. A. Lesieutre; G. H. Koopmann; and C. L. Davis. "*Inertial piezo-ceramic actuators for smart structures*". Smart Structures and Materials, 2447: 14-25, 1995

[19]. R. Babuska and H. B. Verbruggen. "*An overview of fuzzy modeling for control*". Control Engineering Practice, 4 (11): 1593-1606, 1996

[20]. H. Irschik. A review on static and dynamic shape control of structures by piezo-electric actuation. *Engineering Structures*, 24(1): pp. 5-11, 2002

[21]. L.-C. Yao, J.-S. Chen, C,-Y, Hsu, "*A Mode Switching Sliding-mode Controller with Observer-based State-Dependent Boundary Layer and Its Application*". International Journal of Engineering, 1(1): 39-53, 2007

[22]. C. Paulitsch, P. Gardonio and S. J. Elliot. "*Active vibration control using an inertial actuator with internal damping*". Journal of Acoustical Society of America, 119 (4), pp. 2131-2140, 2006
[23]. Gawronski, W. and Williams, T. "*Modal reduction for flexible space structures*". Journal of Guidance, 4: 68–76, 1991
[24]. Gawronski, W. K. "*Dynamics and Control of Structures"*, (Springer-Verlag; New York: First edition.), 1998
[25]. Bellos, J. and Inman, D. J. "*Frequency response of non-proportionally damped, lumped parameter, linear dynamic system".* ASME Journal of Vibration and Acoustics, 112, pp. 194-201, 1990
[26]. Skelton, R. E. and Hughes, P. C. "*Modal cost analysis of linear matrix second-order system*". Journal of Dynamic Systems, Measurements and Control, 102: 151-158, 1980
[27]. Maciejowski, J. M. "*Multi Variable Feedback Design"*. (Addison-Wesley; Workingham: England.) 1989

Table 1: Simulation and Experimental Data

Component	Properties	Dimensions
Thin beam	Aluminum 6061 $E = 6.89 \times 10^{10}\ Pa$ $\rho = 2710\ kg/m^3$ $Poisson's\ Ratio = 0.35$	Length =0.53 m Thickness =2.1 mm Depth=0.035 m
Actuator	ETREMA Terfenol-D Actuator	Stiffness 300 kN/mm Mass=0.203 kg Damping =11560 kg/s Excursion=10 micro-meter pk-pk
Excitation	B&K shaker	1-100 Hz chirp signal + Random input

Table 2: Beam-Actuator system modal frequencies and modal H_2 Norms

Mode Number	Frequency Hz	H_2 Norm
1	10.106	0.05043736496038
2	54.732	0.00179075345056
3	139.72	0.00021895088343
4	195.05	0.00021895088343
5	271.71	0.0000000000000012
6	457.76	0.00004501906852
7	461.14	0.00000000000000
8	590.08	0.00002132364349
9	720.38	0.00000521173674
10	1000.4	0

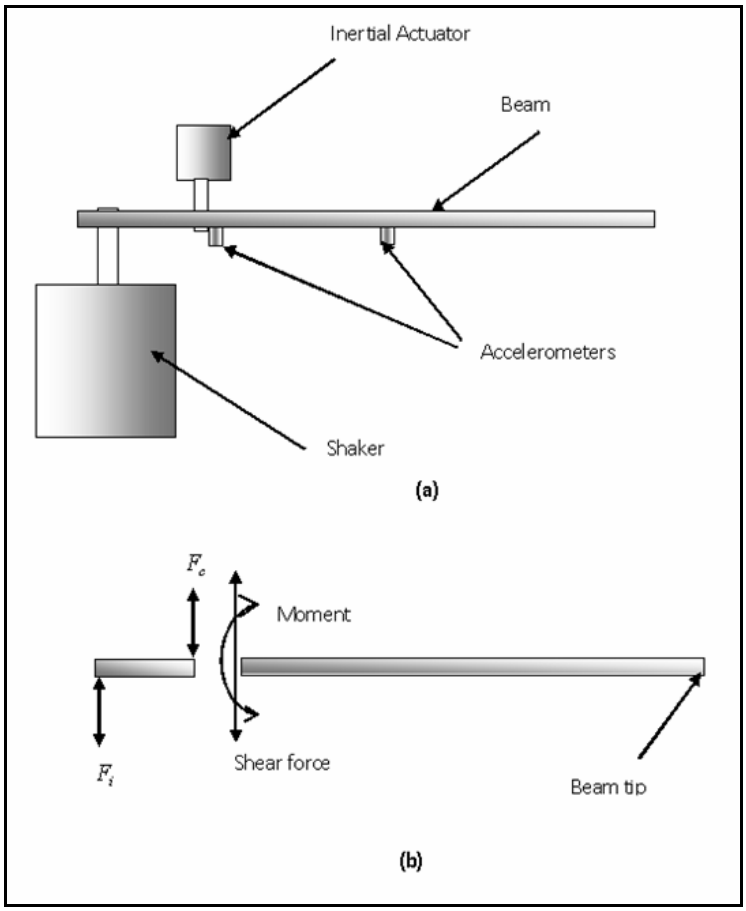

Figure 1: (a) Cantilevered beam mounted on a shaker (b) Free body diagram of the beam

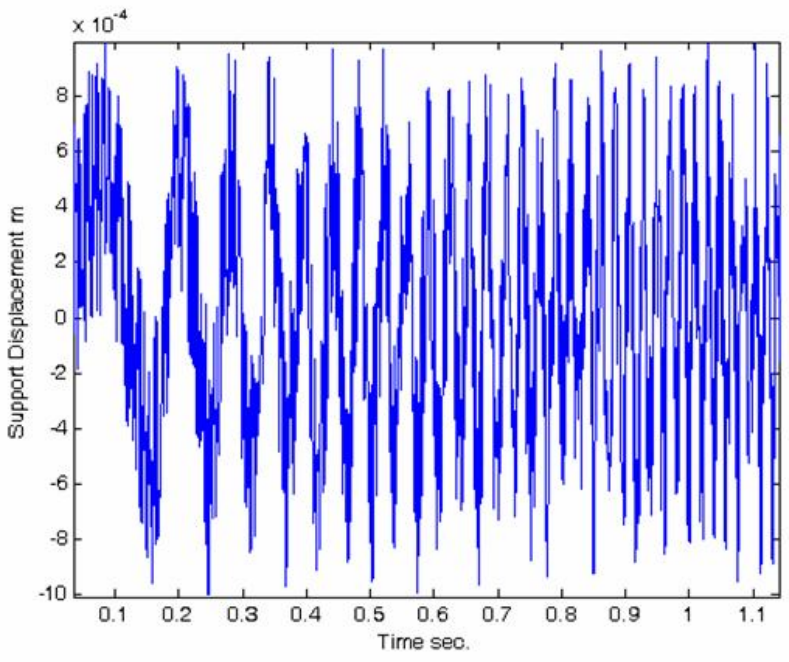

Figure 2: Excitation at the beam's support

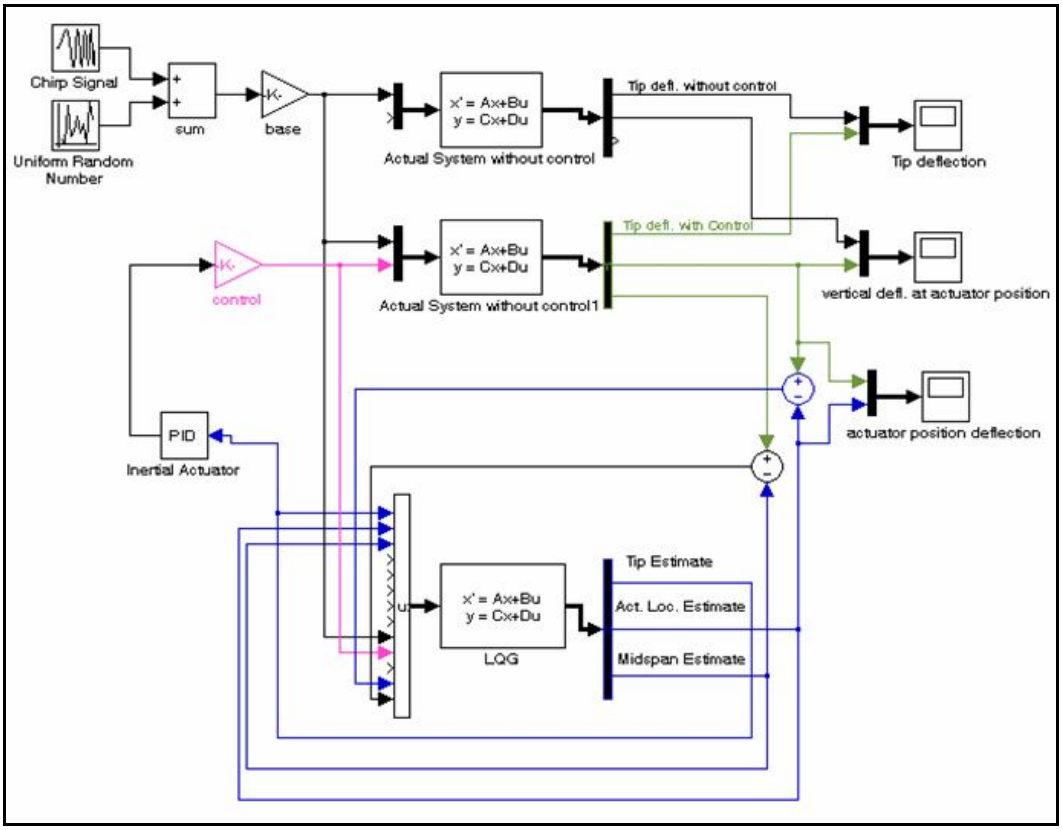

Figure 3: Block Diagram of the control scheme

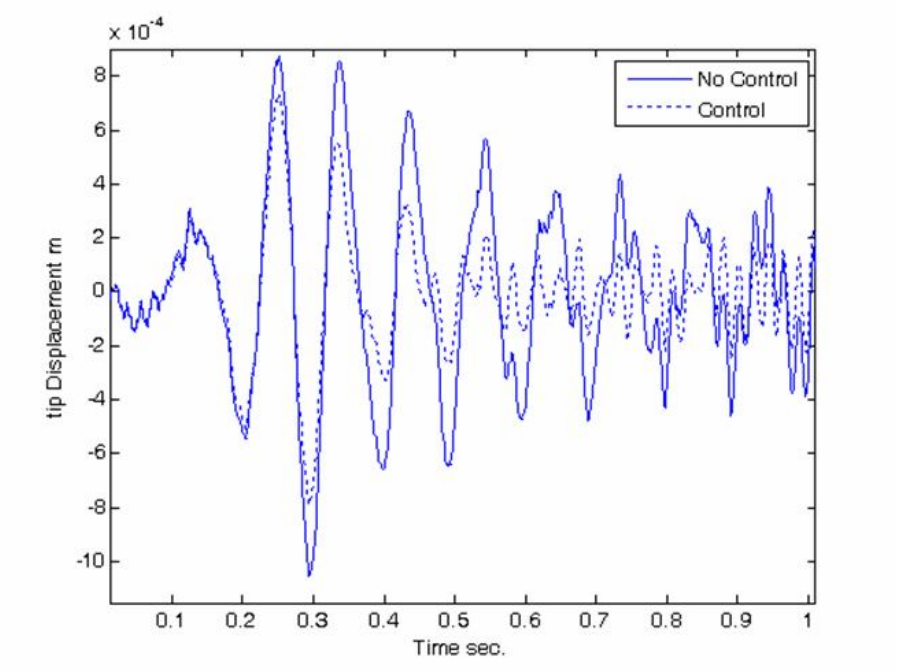

Figure 4: Tip vibration with and without control

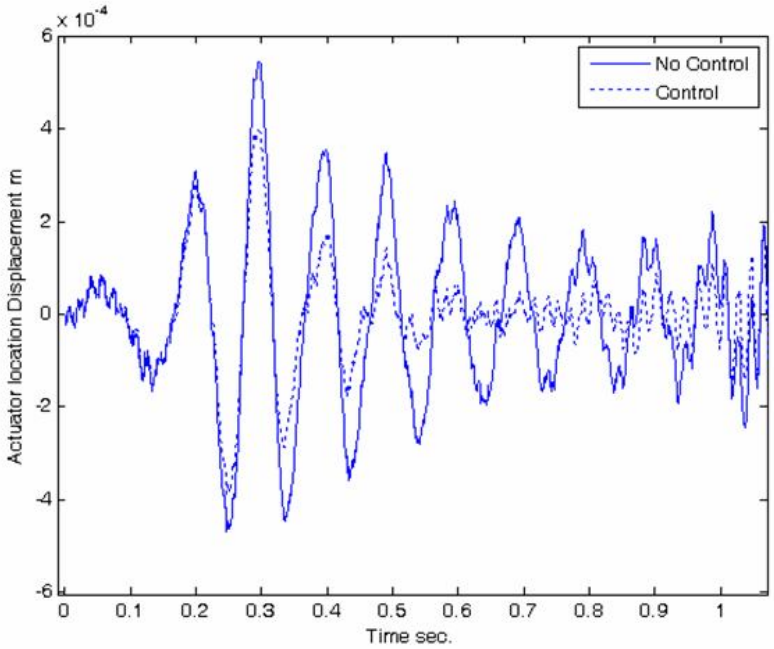

Figure 5: Vibration at the actuator location

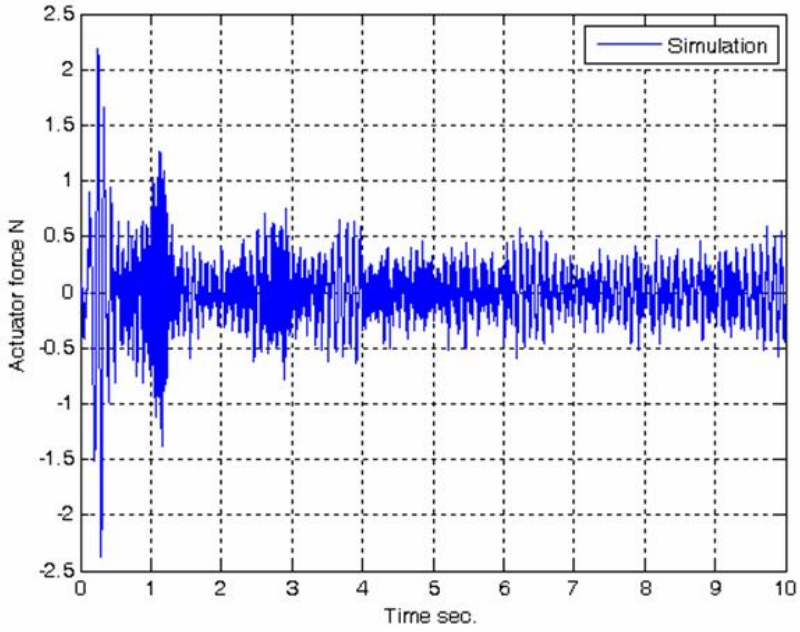

Figure 6: Control force, simulation

Figure 7: Experimental Setup

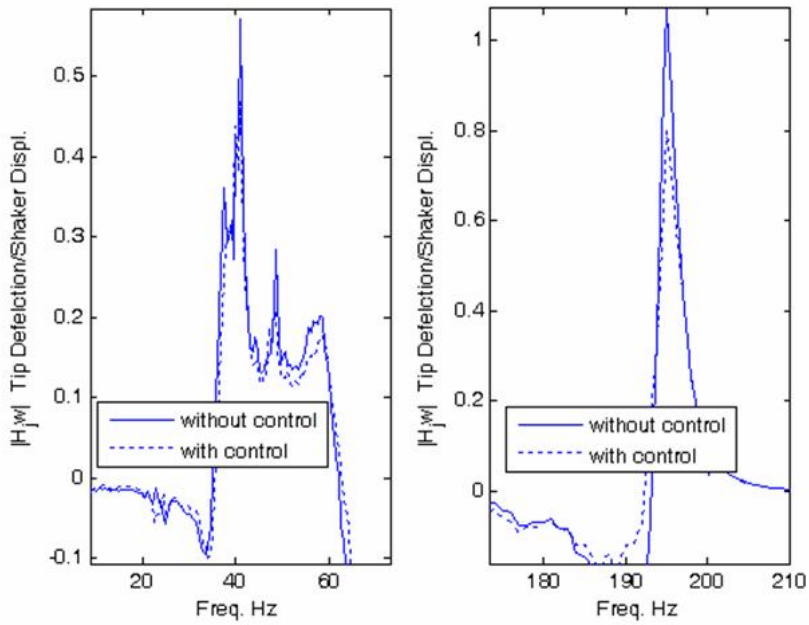

Figure 8: Frequency response function of the beam: tip displacement/shaker displacement

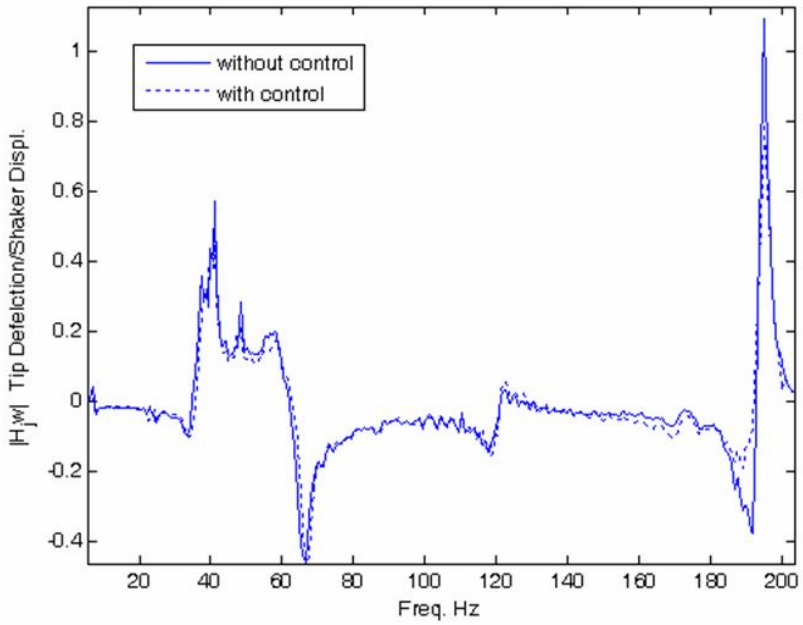

Figure 9: FRF of the beam with and without control

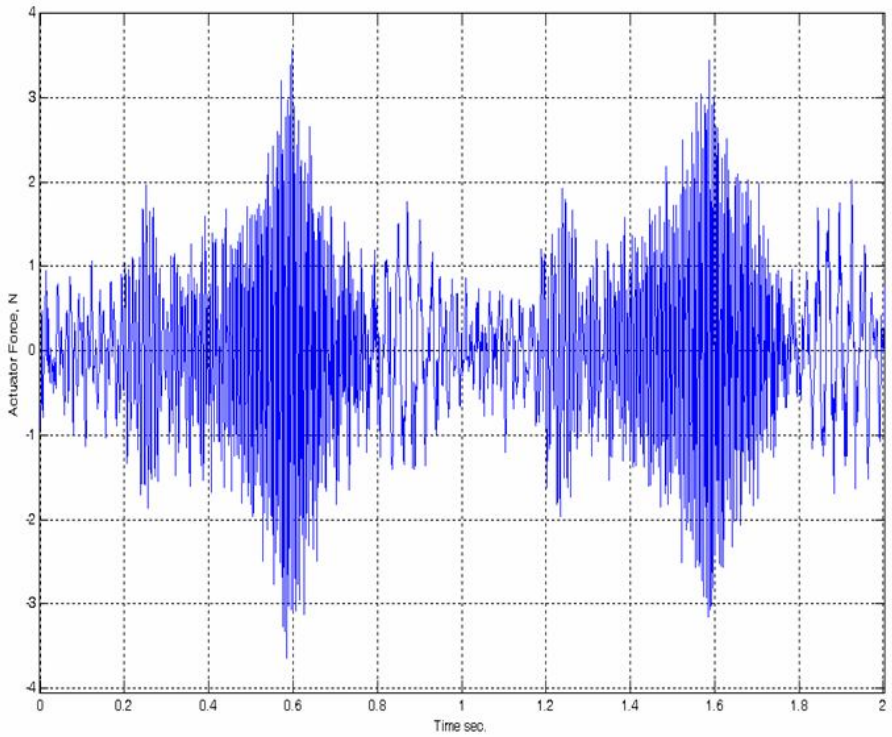

Figure 10: Control force, experimental

A New Strategy to Achieve Radical Combustion Through Exhaust Port Throttling for Two Stroke Engine

Saqaff Ahmed Alkaff saqaff@yemen.net.ye
Faculty of Engineering,
Mechanical Engineering Department
University of Aden, Yemen,
Aden, Yemen

Mohamed A. Khan khan_m_a_a@hotmail.com
Faculty of Engineering,
Mechanical Engineering Department
University of Aden, Yemen,
Aden, Yemen

Abstract

Radical combustion is a critical condition behind control. In two stroke engine, a condition of radical combustion could be achieved through control of the trapped exhaust gases at a certain condition, might include, the engine load, speed, concentration of the unburned hydrocarbons, their temperature and other operational parameters.

An earlier work was conducted towards the achievement of the radical combustion. The mechanism was made to throttle the opening of the exhaust port at a range of 1% to 8 % [1]. However, several difficulties were faced, mainly with the control mechanism of throttling. In addition there is a complexity in identifying the critical conditions at which the radical combustion could be achieved.

In this paper, a new strategy was used to control the exhaust port throttling in a way to manage the amount of exhaust gases trapped and avoiding the drawbacks of the throttling mechanism in the earlier work. Three trial plates were used, one-sixth closed, one-third closed and half closed to throttle the exhaust gases leaving the combustion chamber.

Results reveal the possibility of achieving radical combustion, when using the one-sixth closed plate under relatively higher load. Therefore, partial trapping of the exhaust gases should be carried, through the restriction of the opening of the exhaust port not to exceed 15% of the port exit area. However, it is more interesting, that throttling of the exhaust gases of the two stroke engine have clear influence on the quality and stability of the combustion and hence its direct effect on the fuel consumption and the rate of pollutants expelled to the environment.

Keywords: Spark Ignition Combustion**,** Radical Combustion, Exhaust Port Throttling, Two Stroke Engine, Trial Plates for Throttling Control,

1. INTRODUCTION

The combustion is a chemical reaction in which certain elements of the fuel (i.e. hydrogen and carbon) combined with oxygen liberating heat energy and causing an increase in temperature of the gases. The conditions necessary for combustion are the presence of a combustible mixture and some means of initiating the process (electric spark). Generally, the chemical reaction occurs more rapidly as the temperature increase. Chain reactions are the most common type of chemical reactions occurs in internal combustion engines. They consist of a series of consecutive, competitive and opposing reaction steps with different reaction rate constants [2, 3, 4]. These complex chemical reactions occur in all combustion processes. For many combustion processes, the specific rate constant for separate reaction steps either are not known or have been approximated roughly [5, 6, 7]. In this reaction process, the most active species are called free radicals. In chemical terminology, free radicals are known as unpaired electrons or "bond-paired" electrons. The hydrogen atom is a free radical, as is illustrated below, where the dots symbolize electrons.

$$\mathbf{H:H} \Rightarrow \quad \mathbf{H\bullet + H\bullet}$$

If one hydrogen atom **H** is taken away from $\mathbf{CH_4}$, two radicals are formed;

$$\mathbf{H{:}\,C{:}\,H} \Rightarrow \mathbf{H:C^{\cdot}} + {}^{\cdot}\mathbf{H}$$

Elementary reactions are called chain initiating or chain-terminating reactions, according as they produce or destroy free radicals. Also, with regard to the ratio of the number of free radicals in the products to that in the reactant, elementary reactions are called chain-propagating reactions if the ratio is equal to 1, and bring chain-branching reactions if the ratio is greater than 1. Some elementary reactions and their denominations are given below.

$\mathbf{A_2} \Rightarrow 2\mathbf{A}$ **chain initiating** (A_2 has low dissociation energy)

$$\left.\begin{aligned} \mathbf{A + B_2} &\Rightarrow \mathbf{AB + B} \\ \mathbf{B + A_2} &\Rightarrow \mathbf{AB + A} \\ \mathbf{A + AB} &\Rightarrow \mathbf{A_2 + B} \\ \mathbf{B + AB} &\Rightarrow \mathbf{B_2 + A} \end{aligned}\right\}$$ chain propagating (very fast rate)

$$\left.\begin{aligned} \mathbf{M + 2A} &\Rightarrow \mathbf{A_2 + M} \\ \mathbf{M + 2B} &\Rightarrow \mathbf{B_2 + M} \end{aligned}\right\}$$ chain termination

A and B are called chain carriers or free radicals and seldom build up in high concentrations. The elementary reaction

$$\mathbf{H + O_2} \Rightarrow \mathbf{OH + O}$$

Is a chain branching reaction, since the number of chain carriers formed is more than a number of chain carriers used up in the reaction [8, 9, 10].

In this combustion reaction, the element that involved must have energy supply from outside of the system. The molecules will not react unless heat is produced to some extent from outside. From the analysis, the combustion not only needs the high temperature but also by fuel concentration and pressure. Below this temperature, the chain reaction does not take place because of the few molecules acquire the activation of the combustion reaction have not enough energy[11, 12, 13].

The most important elements of the fuel are carbon and hydrogen with a small amount of sulphur, oxygen, water vapour, nitrogen and ash. The fuel elements are bonded to one and another. The bonding systems have their own energy and are difficult to break. To make sure this hydrocarbon

reacts, the energy must be added to break these bonds. Though there are many kinds of fuel as well as very complicated combustion mechanisms, fuels usually decompose before the combustion starts and the oxidation occurs through some basic form. The main substances are hydrogen, carbon monoxide, gaseous hydrocarbons and solid carbon [14, 15].

2. ACTIVATED RADICAL COMBUSTION THEORY

When the spark plug fires and ignites the fuel mixture, some of the fuel is isolated from the resulting flame by the exhaust constituents remained in the cylinder from the previous cycle and does not burn. Activated radical combustion process will burn all the fuel inside the combustion chamber by using the active radical molecules that are formed in the exhaust gas. When hot exhaust gases remain in the cylinder, it contains a small percentage of active radical molecules; when these are combined with the incoming fuel charge, the resulting mixture begins to auto-ignite at a lower temperature in comparison to that of a pure gasoline/air mixture [14, 17, 18, 19].

3. ACHIEVEMENT OF RADICAL COMBUSTION

Radical combustion is a critical condition behind control. The condition of the radical combustion is affected by the amount of exhaust gases trapped in the combustion chamber at certain critical conditions, including the engine load, engine speed, concentration of unburned hydrocarbons presence in the trapped part of exhaust and its temperature [1, 20, 21].

The earlier work was carried for the achievement of the radical combustion. A control of the amount of exhaust gasses flow out from combustion space, will lead to trap small amount of exhaust gasses and kept to the next cycle inside the combustion chamber. Trapping of such part of exhaust gases may assure the existence of radical agents as OH and H. The exhaust port throttling mechanism to control the amount of the exhaust gases flow out from the combustion chamber has been designed and fabricated. A sliding plate has been fabricated to slide within the machined slot in the cylinder block. Figure 1. illustrates the exhaust throttling mechanism and the slot machined through the cylinder head and the cylinder block.

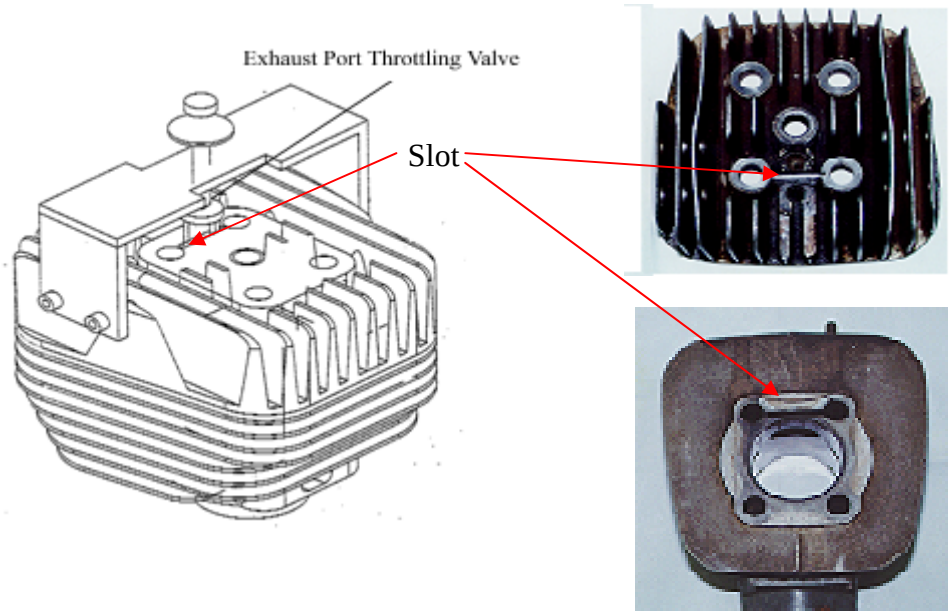

FIGURE 1: Illustration of the Throttling Valve Mechanism.

A very close tolerance slot was machined through the cylinder head and the cylinder block, in which the control blade move in and out to control the opening of the exhaust port. The machining process was carried out by Electrical Discharge Machining (EDM). The control blade was made of stainless steel and machined with very close tolerance with the slot using CNC machine. The control blade and its slot must have close tolerance to avoid any leakage. A spring is used to make sure that the control blade can move up or down, to increase or decrease the exhaust port opening. In this operation, the spring was in turn act to reduce vibration effect of the blade.

In this throttling process, the amounts of exhaust gases flow out can be reduced, hence a part of it will be kept inside the combustion chamber. Applying this type of throttling process, the occur of radical combustion was investigated. The engine is tested under different operating condition at which the exhaust port throttling was set at a range of 2 to 16 mm (exhaust port area of 1 to 8%). It was proved that radical combustion took place at an engine speed of 3000 to 4000 rpm while the engine load was in the range of 1 to 2.5 N.m. Specification of the classical two-stroke engine used in the test, condition of testing and the detailed results of the work were introduced [22, 23]. It was found that when the engine running under radical combustion, assures almost complete stable combustion. In addition the engine could run under lower temperature and with minimum emission as it is proved that contents of exhaust gases have much less CO and minimum Nitrogen Oxides NO_x. A typical results of the previous study are illustrated in figures 2 and 3. It is clear that, lower Specific Fuel Consumption (SFC)) of the engine under radical combustion could be achieved. This indicate better fuel economy. Figure 3 shows a good indication of relative increase of the carbon dioxide CO_2 under radical combustion which lead to tendency of complete combustion.

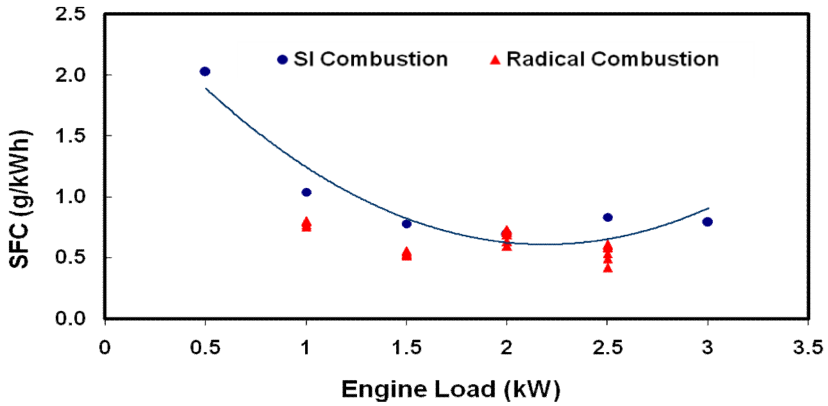

FIGURE 2: Specific Fuel Consumption (SFC) For SI Combustion and Radical Combustion (Engine Speed 4000)

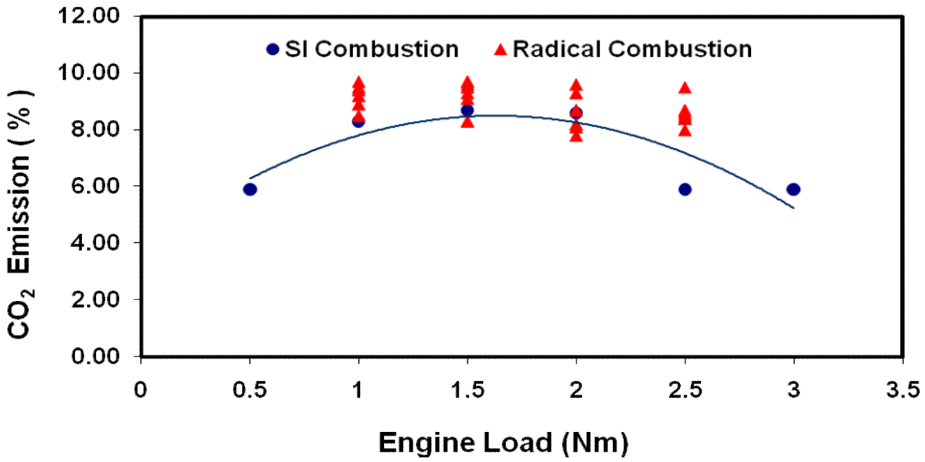

FGURE 3: CO_2 Emission for SI Combustion and Radical Combustion (Speed N=4000 rpm)

Although the above-mentioned method achieve radical combustion, but there are several difficulties faced with such mechanism of the exhaust port throttling, and summarized as follows:

1. Accumulation of carbon deposits on the moving blade as it is exposed to the combustion products. In the other hand, the high temperature reached, lead to affect the sliding mechanism and hence influence the accuracy of the throttling control.

2. As the slot is machined within a narrow space just at a side of the liner on the cylinder block, which make sealing is difficult as the gasket at that part is thin and might lead to a serious leakage, which in turn affect the engine performance.

3. This throttling mechanism was relatively costly, as highly sophisticated machines was used for the machining and producing its components.

4. Manual control of the throttling mechanism will be difficult and not reliable.

The above mentioned difficulties, made such type of throttling control was not successful.

4. A NEW STRATEGY FOR EXHAUST PORT THROTTLING:

In this paper, a new strategy is followed to overcome the above difficulties. The same classical two stroke engine was used. No modification this time is carried on the cylinder head or the cylinder block. The throttling control is placed, just at the point where, the exhaust manifold is connected to the cylinder block. Figure 4: shows clearly the position where to place the throttling control of a partially closed plate. The throttling process, is carried by means of a partially closed plate, at the exit of the exhaust port, to restrict and control of the amount of exhaust gases come out from the combustion chamber.

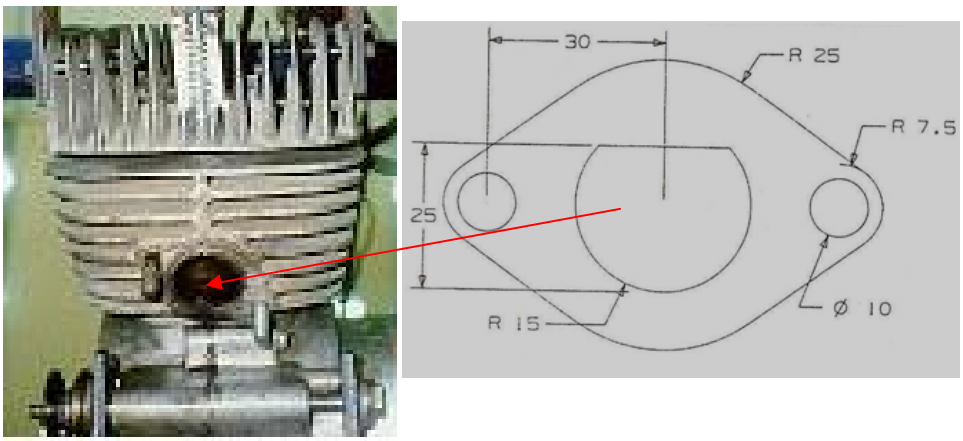

FIGURE 4: A Partially Closed Plate, To Be Fitted To Control The Flow Of The Exhaust Gases Come Out Of The Engine.

In this method of the exhaust port throttling, assuring the simplicity of control of the flow of exhaust gases. Thus displacing the gate of the throttling at the outer side of the cylinder block overcoming the drawback of the earlier work mechanism.

In this case the throttling process was carried out using three different trial plates of different opening size, one-sixth closed, one-third closed and half open, to throttle the exhaust gases leaving the combustion chamber. The configuration of those plates is illustrated in figure 5. The

plates was designed and fabricated to fit easily at the exit of the exhaust port where the neck of the exhaust pipe (exhaust manifold) is to be fitted.

FIGURE 5. Different Trial Plates of Different Opening.

4.1 Engine Testing

A single cylinder, 100 cc direct scavenging, air cooled two-stroke SI engine was employed in the present investigation. This engine was coupled to water dynamometer for torque measurements. A computer exhaust gas analyzer was used to measure the unburned hydrocarbon (UHC), Nitrogen oxides (NO_x) as a part per million (ppm), carbon monoxide (CO), carbon dioxide (CO_2) and Oxygen (O_2) as a percentage emission levels in the engine exhaust. Calibrated standard instrumentation was used for air and fuel flow rates, and exhaust temperature measurement. Experiments were conducted with ignition system using a normal spark plug, without any restriction on the exhaust gases, hence the engine was run as a normal spark ignition combustion. The engine was tested under different engine speed, ranges from 2000 rpm to 4000 rpm.

4.2 Engine Run to Achieve Radical Combustion:

In this stage the engine was run to achieve radical combustion, using the new strategy of control illustrated above. The partially closed plates are fitted alternatively to investigate the achievement of the radical combustion. The plate will act to restrict the flow of exhaust gases come out of the engine, thus lead to trap apart of the exhaust in the combustion space to the next cycle. The exhaust port opening area is 560 mm^2, if the plate is fully open. So with fitting of the different opening plates, the exhaust gases flow could be controlled. Therefore, the trap of a part of exhaust gases rich with free radicals, might lead to the achievement of radical combustion.

5. RESULTS AND DISCUSSION

The main goal of this paper is to investigate the criticality of radical combustion and its achievement using a simple method to throttle the engine exhaust gases. Different partially closed plates were used in the experiment, to trap a part of the exhaust gases likely rich with free radicals to the next cycle. Once, the new charge introduced to the engine combustion chamber will be mixed with the trapped exhaust gases carry radical, lead to achieve radical combustion.

The engine test results was recorded at speed range from 2000 to 4000 rpm, with spark ignition combustion (SI combustion, normal run). For the same range of speed, the engine results, for the condition with the exhaust throttle also recorded. The engine different parameters as UHC, SFC, NO_x, CO_2 and others are traced at different operating conditions under varying engine load. Results reveal the difficulty to achieve radical combustion, except with presence of plate one-sixth closed and at a higher speed. The other trial plates (one-third closed and half open), made the engine to run with less stable running condition, cause more interrupted running of the engine. More restriction of the exhaust gases will act to dilute the charge and lead to retard the combustion.

However, with the one-sixth closed trial plate, after several runs it was found that radical combustion could be achieved, under specific operating conditions. A sample of some of the

results are introduced to indicate the difference of the condition of normal run (SI combustion) and radical combustion.

Figure 6; presents the measured unburned hydrocarbon UHC emission versus engine load at 4000 rpm. Restriction and control of the exhaust port opening acts to achieve the radical combustion. Therefore, more stable combustion consumes most of the hydrocarbons of the fuel in an efficient way. This clearly indicate the reduction of the UHC emission levels. A noticeable decrease in the level of UHC ensure better combustion compared to the case of normal run (SI combustion) of a classical two stroke engine where UHC emission levels is normally higher. It is found that, there is a good agreement of this result with that obtain in an exhaust gas recycle (EGR), in which, slow down the speed of chemical reactions. This is favorable at higher speed, for two stroke engine as it give more chance for complete combustion, thus reduction in fuel consumption and exhaust emissions [24, 25].

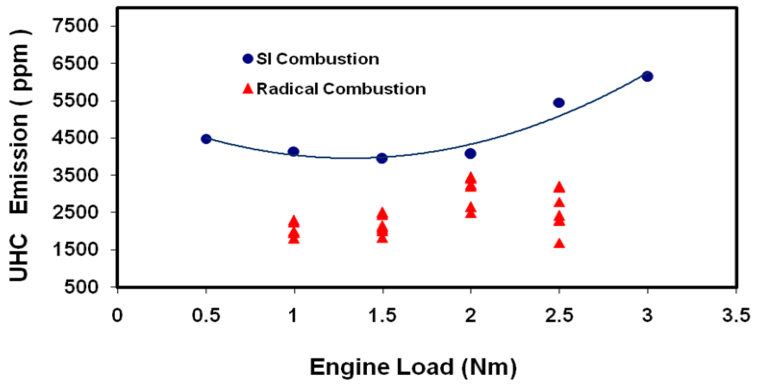

FGURE 6: UHC Emission for SI Combustion and Radical Combustion (Speed N=4000 rpm)

Figure 7; indicate the clear difference of the temperatures of the exhaust gases at normal running condition (spark ignition SI combustion) and radical combustion running condition. It is observed that when engine is running on radical combustion the exhaust gases temperature is lower over the entire load range. The reduction in the exhaust temperature is due to the trap of exhaust gases in the combustion space by restriction of their flow and mixed with new charge, acting to dilute the mixture. This might deplete the reaction and lead to noticeable decrease of the exhaust gas temperature under radical combustion. In addition, the radical combustion is sensitive to the condition of the exhaust trapped, in particular its temperature, and pressure [26].

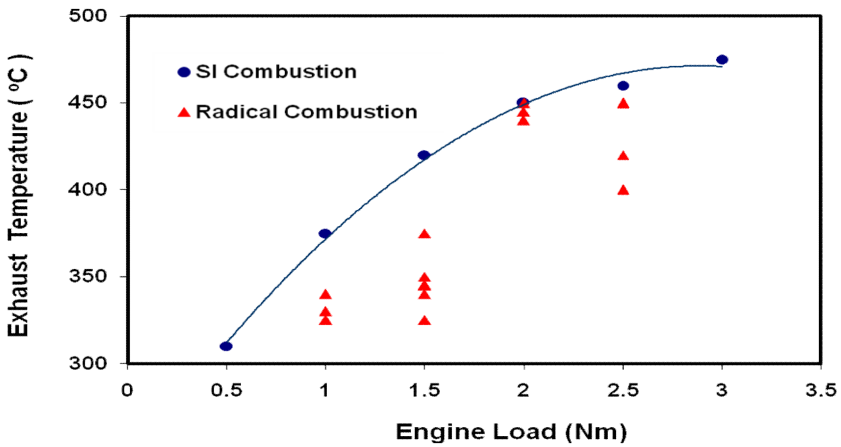

FGURE 7: Exhaust Temperature for SI Combustion and Radical Combustion (Speed N=4000 rpm)

The O_2 emission under SI ignition and radical combustion is investigated. Figure 8; shows the clear reduction of Oxygen percentage compared to that under SI combustion at 4000 rpm, in particular under moderate load. At higher engine speed the oxygen reacted with the hydrocarbon to form CO. With the restriction of the exhaust flow, the residence time is increases, which will further convert the CO to CO_2 and to the oxides of nitrogen, leading consume more oxygen. It is an evident that under radical combustion where auto-ignition is predominant more stable combustion is recorded with less exhaust emissions [27, 28]

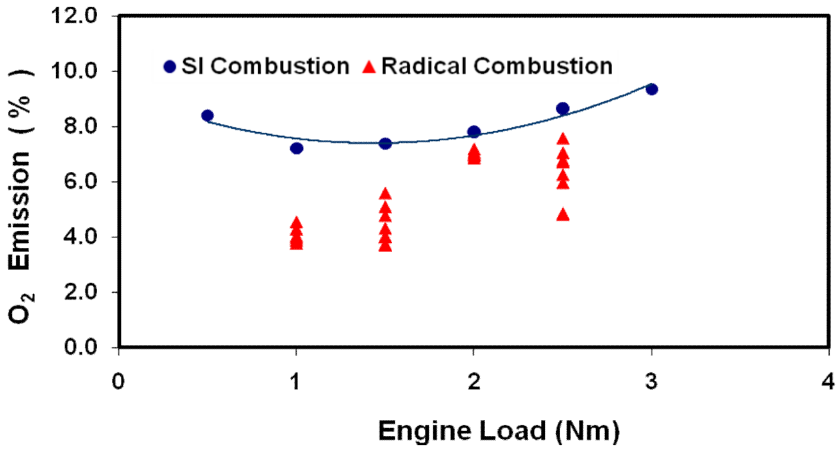

FGURE 8: O_2 Emission for SI Combustion and Radical Combustion (Speed N=4000 rpm)

Investigating of the engine running, incorporated with this new strategy of exhaust port throttling (throttling control at the exit of the exhaust port) leads to several interesting results about the criticality and conditions at which radial combustion is occurring.

1. The throttling controller should be placed adjacent to the exit from the combustion chamber. Displacement of the location of the controller as conducted in this run of experiment, made it hardly to achieve the radical combustion. It is believed that displacement of the throttling control will sweep some of the radical agents to the extra volume formed by the passage (between the port exit and manifold neck). Therefore considerable amount of those active radical will leave the combustion chamber hence reduce the activity of the mixture to achieve radical combustion.

2. Partial trapping of the exhaust gases should be carried through throttling of the exhaust port with a limit not to exceed 15 % of the exit area. Increase of the amount exhaust gases trapped lead to dilute the mixture inside the combustion chamber and hence affect the rate of combustion.

3. As the piston descends and the exhaust port starts to open, most of the unburned hydrocarbon (UBH) leave with first lot hence, presence of this extra volume due displacing of the controller will contribute in trapping less active exhaust gases.

4. As the amount of the exhaust gases trapped increase, it was found that radical combustion is taking place at relatively higher speed and load. Therefore, the volume and state of the trapped exhaust gases are very critical to achieve radical conditions.

5. Results reveal the importance of the shape and direction of opening of the exhaust port. Occurring of the radical combustion is strongly affected by the condition inside the combustion chamber, and the amount of exhaust gases trapped and their content of active radical.

However, it is more interesting, that throttling of the exhaust for two stroke engines have clear effect on the quality and stability of the combustion and hence its direct effect on the fuel consumption and the rate of pollutants expelled to the environment.

6. REFERENCES

1. Alkaff S. A, Ahmed Suhimi and, Hakim A Abbass." *Radical combustion. New concept for two stroke (SI) engines"* . ASEAN Journal On Scientific and Technology for Development Singapore. 17 (2) :91-99, 2000.

2. V.Ya. Basevich. "Chemical kinetics in the combustion processes: A detailed kinetics mechanism and its implementation". Progress in Energy and Combustion Science, Volume 13,Issue 3, Pages 199-248, 1987.

3. G.P. Huffman, F.E. Huggins, Naresh Shah and Anup Shah. "Behavior of basic elements during coal combustion". Progress in Energy and Combustion Science, Volume 16, Issue 4, Pages 243-251, 1990.

4. John M. Simmie . "Detailed chemical kinetic models for the combustion of hydrocarbon fuels". Progress in Energy and Combustion Science, Volume 29, Issue 6,Pages 599-634; 2003.

5. B. Lewis and G. Von Elbe." Combustion, Flames And Explosions Of Gases" , Academic Press, New York, (1951).

6. John B. Heywood. "Internal Combustion Engines Fundamentals". Mc-Graw hill Publishing Company. (1988).

7. Noorfidza Yub Harun; M.T. Afzal and Noorliza Shamsudin. " Reactivity Studies of Sludge and Biomass Combustion". International Journal of Engineering (IJE), Volume (3) : Issue(4). P 413-426. November 2009

8. Stone Richard. " Introduction to internal combustion". Mac Millan Publisher Ltd.; London (1985).

9. Kito, S., Wakai, K., Takahashi, S. and Komori, K. "Ignition Limit of Lean Mixture by Hydrogen Flame Jet Ignition." Proceedings of 15th Internal Combustion Engine Symposium; in Seoul, pp.233-238(1999).

10. Takeharu Hasegawa . "Gas Turbine Combustion and Ammonia Removal Technology of Gasified Fuels". Energies Journal , Volume 3, Issue 3. 335-449; 2010.

11. Semin ; Abdul Rahim Ismail and Rosli Abu Bakar. " Combustion Temperature Effect of Diesel Engine Convert to Compressed Natural Gas Engine ". American Journal of Engineering and Applied Sciences . Vol: 2 Issue: 1; P 212-216;.2009.

12. Catania, A.E., D. Misul, E. Spessa and A. Vassallo. " Analysis of combustion parameters and their relation to operating variables and exhaust emissions in an upgraded multivalve bi-fuel CNG SI engine". SAE Paper No. 2004-01-0983;2004.

13. E. I. Zabryanskii1 and V. P. Grebenshchikov. "Combustion temperatures of hydrocarbons and fuels" . Journal Chemistry and Technology of Fuels and Oils . Springer New York. P. Volume 8, Number 2;. P. 138-140;1972.

14. Ming Jia and Maozhao Xie . “A chemical kinetics model of iso-octane oxidation for HCCI engines.” Fuel Journal, volume 85(17–18) 2593–2604;2006.

15. Wakai, K., Shimizu, S., Fuma, H., Hirata T. and Taniguchi, H. "Study on the combustion in a Divided Chamber (Ignition Mechanism of Main Chamber Mixture)." Transaction of JSME (Section B) , 51-465, pp.1600-1609;1985.

16. Kuo, Kenneth K. “ Principles Of Combustion” . John Wiley & Sons, Inc., New York, (1986).

17. Spalding, D.B. “ Combustion and Mass Transfer”. Pegamon Press, New York, (1979).

18. Y. Ishibashi. “Basic understanding of activated radical combustion and its two-stroke engine application and benefits”. SAE paper 2000-01-1836;2000.

19. H. Zhao, J. Li, T. Ma and N. Ladommatos, “Performance and analysis of a 4-stroke multi-cylinder gasoline engine with CAI combustion”. SAE paper 2002-01-0420; March 2002

20. Q J. . Allen, D. Law. “Variable valve actuated controlled auto-ignition: speed load maps and strategic regimes of operation”. SAE paper 2002-01-0422 ; March 2002.

21. Steven Ashley. “A Radical Way to Burn”. Mechanical Engineering Journal. P.64-67; 1996.

22. Alkaff S. A, Ahmed Suhimi and, Hakim A Abbass. “ Radical Combustion for Two Stroke Spark Ignition Engines”. Bureau of Research and Consultancy (BRC) Seminar. MARA University Technology (UITM), Shah Alam, Malaysia, 1998.

23. Alkaff S. A, Ahmed Suhimi and, Hakim A Abbass. “Radical Combustion in Two Stroke (SI) Engines, Performance and Exhaust Emissions”. Bureau Of Research And Consultancy Journal, UiTM Malaysia.1, 11-24,1999.

24. y. ohyama. “Engine Control Using Combustion Model” . International Journal of Automotive Technology, Vol. 2, No. 2, pp. 53−62 (2001)

25. Soek Woo Kim and Yasuo Moriyoshi .”Analysis of Compression Ignition Combustion in Schnurle-Type Gasoline Engine”. KSME International Journal Vol: 18; No. 8, P. 1451-1406; 2004.

26. P. Amneus, D. Nilsson, F. Mauss, M. Christensen and B. Johansson. “ Homogeneous Charge Compression Ignition Engine”. The fourth International Symposium COMODIA 98; P. 567-572;1998.

27. Wijesinghe and G Hong. “Study of the auto-ignition combustion operating region of a small two-stroke engine”. Proc. IMechE Vol. 223 Part D: J. Automobile Engineering; P 651.659 2009.

28. Shunsuk Hashimoto, Yasunori Amino, Koji Yoshida, Hideo Shoji and Atsushi Saima. “ Analysis of OH Radical Emission Intensity during Auto ignition in a 2-Stroke Engine”. The fourth International Symposium COMODIA 98. P 405-410;1998.

Bi-level Control and Chopper Control Methods for Improving the Dynamic Performance of Stepper Motor

Walid Emar Walidemar@yahoo.com
Faculty of Engineering/Electrical Dept./Power electronics and Control
Isra University
Amman, 11622, Jordan

Ziad Sobih Zeyadsobeh@hotmail.com
Faculty of Engineering/Electrical Dept
Northeastern University
Boston, MA02115, USA

Musbah Aqel Musbahaqel@yahoo.com
Faculty of Engineering/Electrical Dept
Applied Science University
Amman, Jordan

Mahmoud S. Awad Dr_Awad_M@yahoo.com
Faculty of Engineering/Electrical Dept
Al-Balqa Applied University
Amman, Jordan

Abstract

This paper compares between chopper control method and bi-level control method. Both methods are used for improving the dynamic performance of variable reluctance stepper motor (VRSM) by modifying its time constant and thus, increasing its stepping rate. Therefore, the initial torque developed by the motor is high; the switching from one coil to the next is faster than normal and consequently, the rotor moves as quickly as it should be. The circuitry discussed in this paper is connected directly to the motor windings and the motor power supply, and this circuitry is controlled by a digital system that determines when the switches are turned on or off. Each class of drive circuit is illustrated with practical examples, but these examples are not intended as an exhaustive catalog of the commercially available control circuits, nor is the information given here intended to substitute for the information found on the manufacturer's component data sheets for the parts mentioned.

Keywords: Stepper motor, variable reluctance motor, time constant, new topology of chopper converter, chopper control.

1. INTRODUCTION

The dynamic response of stepper motor may be improved by using special drive and control circuits yielding better time constant, faster stepping rate and therefore higher torque and well working rotor [5].

For most industrial applications stepping motors are controlled by using microprocessor techniques. With the microprocessor any of the types of control can be used such as linear constant current control, bi-level control or chopper PWM control. It can make the motor to run through the desired number of steps and can control the acceleration and deceleration of the motor when required[2-5].

In this paper a bi-level and chopper PWM control will be demonstrated. At the end, a brief comparison is done to show the priority of each control method and drive circuitry.

2. FUNDAMENTAL PRINCIPLE OF CHOPPER CONTROL OF STEPPER MOTOR

The typical stepper motor with four windings with the drive waveforms are shown in the schematic diagram in Figure 1a, with one terminal common to all windings; it is most likely a variable reluctance stepping motor.

In use, the common wire typically goes to the positive supply and the windings are energized in sequence [12].

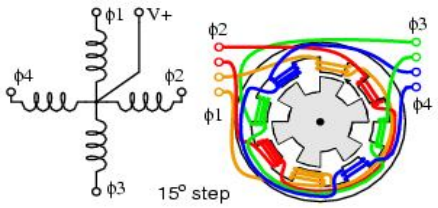

(a)

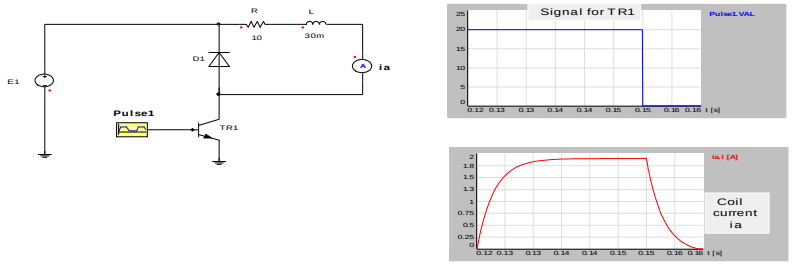

(b)

Figure 1: (a) Four phase (4-Φ) variable reluctance stepper motor. (b) Fundamental connection of a chopper down converter and phase current waveforms: ($E_1 = 5 - V, L = 30mH, R = 10\Omega$).

Figure 1b shows the equivalent circuit of one phase of the motor and a fundamental chopper down (step down) converter and the waveforms of the motor phase currents.

The basic principle of operation for a four winding variable reluctance stepper motor is illustrated in Figure 1.

The stator has 8 poles and the rotor has 6 teeth. When one of the stator coils is energized, the rotor teeth will align with the energized stator poles. This means, that the rotor will move to a position of minimum reluctance. Sequentially switching the stator phases produces a rotating magnetic field which the rotor follows. However, due to the lesser number of rotor poles, the rotor moves less than the stator angle for each step [1, 3, 6].

For a variable reluctance stepper motor, the step angle is given by:

$$\theta_s = 360^\circ / N_S \quad (1)$$

Where: θ_s is stator angle; N_S is number of stator poles.

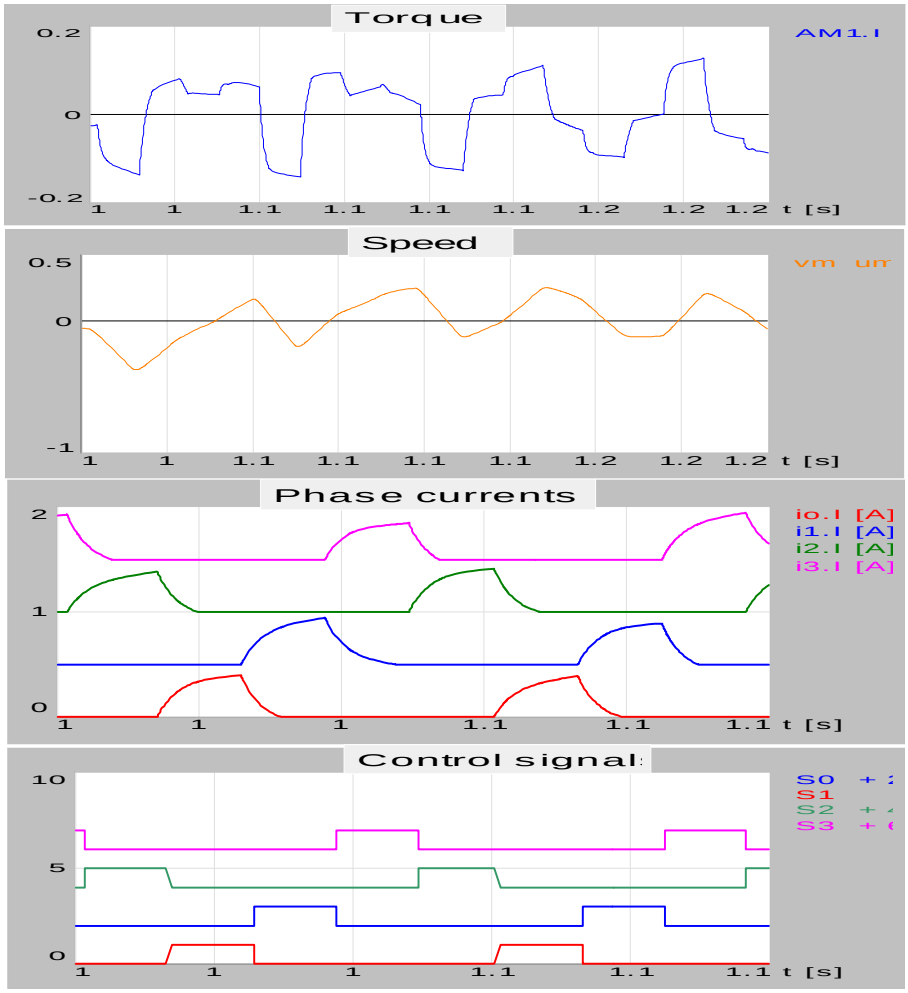

Figure 2: Schematic diagram showing torque, speed and phase current waveforms of a four phase variable reluctance stepper motor.

$$\theta_R = 360^\circ / N_R \quad (2)$$

Where: θ_R is rotor angle; N_R is number of rotor poles.

$$\theta_{ST} = \theta_R - \theta_S$$
$$= \frac{N_S - N_R}{N_S . N_R} \times 360^{\circ} \quad (3)$$

Where: θ_{ST} is step angle. The number of stator poles is the product of number of phases and number of poles per phase. Thus

$$N_S = m \times N_P \quad (4)$$

Where: m is number of poles; N_p is number of stator poles per phase.

Figure 1 shows that moving from Φ_1 to Φ_2, etc., the stator magnetic field rotates clockwise. By reversing the sequence of pulses, the direction of rotation is reversed above right. The direction, step rate, and number of steps are controlled by a stepper motor controller feeding a driver or amplifier. This could be combined into a single circuit board [1, 2, 10].

Figure 2 shows the resultant torque, speed and current waveforms of a 4-Φ variable reluctance stepper motor.

3. IMPROVEMENT METHODS OF DYNAMIC RESPONSE OF STEPPER MOTOR

It has been mentioned earlier that the basic problem for the drive of a VRSM lies in the inductance of the stator winding. The time constant ($\tau = L/R$) of the motor winding prevents the current to follow the winding voltage pulse**.** The current rises slowly and does not reach the full rated value, particularly at high speed. As a result the torque decreases with increase of pulse rate. Hence, the torque speed performance can be improved by using one of the following drive methods:

- Bi-level control method.
- Chopper control method

3.1 Bi-level control method

A good approach to improve the dynamic response of stepper motor is to use two power supplies instead of one. This is called bi-level control as shown in Figure 3. Bi-level drive enables us to obtain fast rise and fall times of current without using external resistors[5].

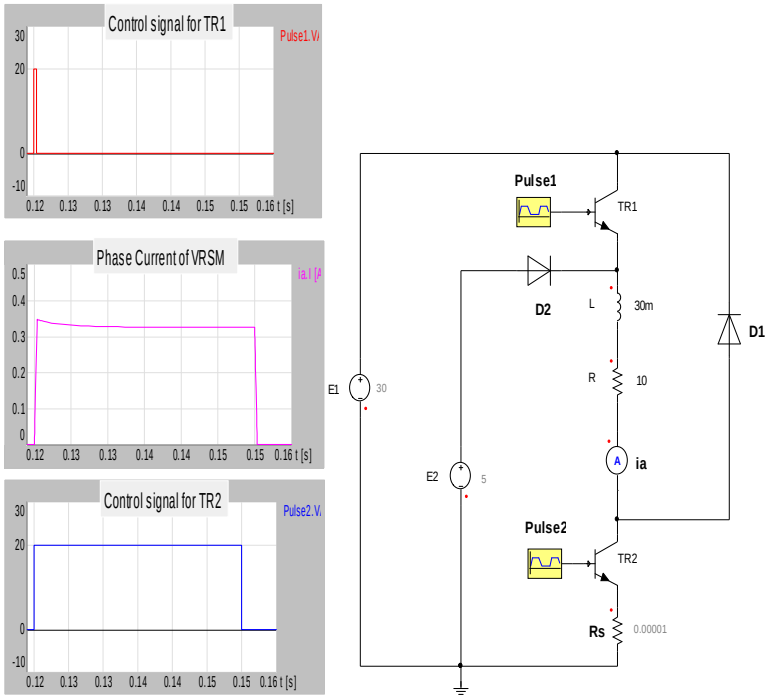

Figure 3: Bi-level control scheme of VRSM drive with current waveforms.

The principle of a bi-level control can be explained as follows: In this system there are two power supplies E_1, E_2. The upper supply E_1 is about *5* to *10* times higher than E_2 which is the rated value of the motor supply. The current sensing resistor R_s is not considered in this case ($R_s \rightarrow 0$).

At the starting of each step E_1 is connected to the motor coil. The coil current rises much faster than the rated supply and as soon as the coil current reaches the rated value; the supply is changed from E_1 to E_2. This continues with TR1 off and TR2 on upto the end of one step. When it is required to end the pulse TR2 is turned off and the current decays through the load, both freewheeling diodes D1, D2 and both supply voltages E1, E2. In this way losses in the circuit are reduced and the overall efficiency is increased.

3.2 Chopper control method

Chopper control may be achieved by using different types of chopper converters. Not all of these converters help to improve the performance of stepper motors. This paper introduces a new topology of chopper converters which significantly improves the dynamic performance of stepper motors.

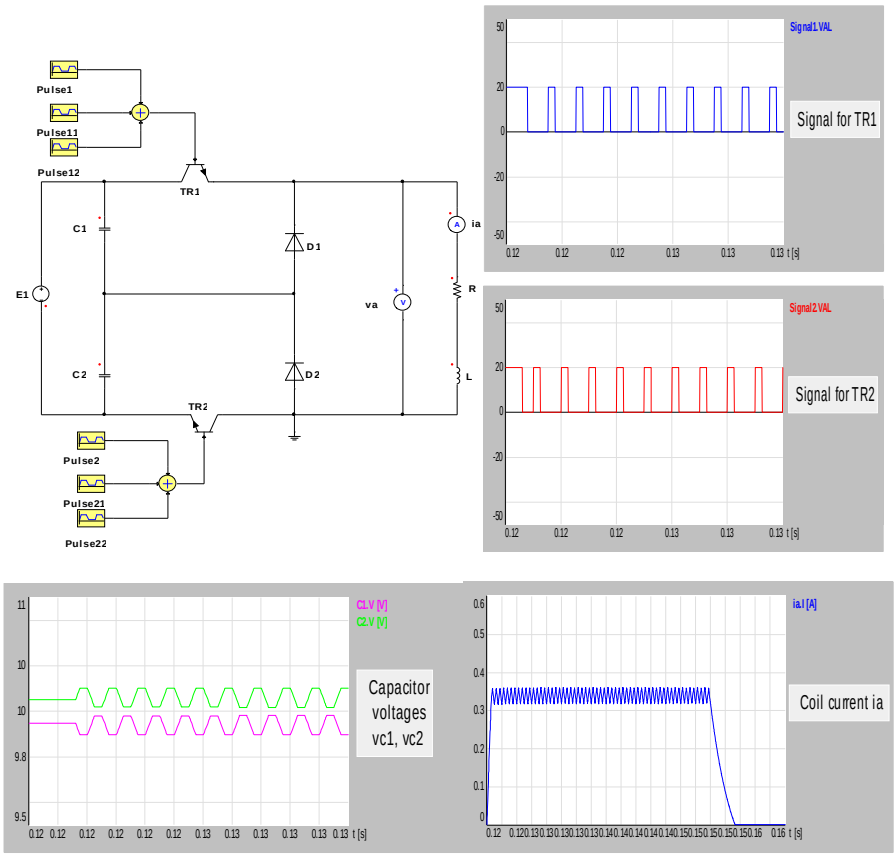

Figure 4: schematic diagram of a series connected double phase chopper down converter with Current and voltage waveforms.

The system is described with the help of Figure 4. The circuit in this figure consists of a chopper-down converter with two channels connected in series. In this scheme higher supply voltage E_1 is used. It may be as high as 2 to 4 times of the rated value of the motor voltage. This connection is also used to increase the voltage-handling capability of the power devices. It also gives with a variable output voltage the possibility of varying the motor speed by varying its terminal voltage.

Principle of operation of such connection may be explained as follows: The motor is switched on by the sequencer signal with this high voltage supply and the two capacitors (C_1, C_2). At the beginning both switches are on for a time required for the circuit current i_a to reach its rated value. Thus, if the supply voltage had a value of 30-V and if the switches were on all the time, the resulting current in the circuit would be $30V/10\Omega = 3A$. This is much greater than the required rated current (*0.5A*). The rate of rise of coil current increases and reaches its rated current much faster. The time constant of the circuit is again $L/R = 30/10 = 3ms$. Thus, the current in the coil rises at a rate of $30/3ms = 1000A/s$. The time to reach *0.5A* is then $0.5(A)/1000(A/s) = 0.5ms$.

As soon as the current reaches slightly above the rated value, both switches are periodically turned off and on using pulse width modulation (PWM) technique. The switches connected in series are usually operating out of phase by the time *T/2*. During this period each switch is on for certain time t_{on} to yield the required mean value of the coil voltage and off for the rest of this operating period, t_{off}. Both transistors have the same operating period T_p which is many times smaller than the energizing pulse (period) of the coil. When it is required to end the energizing pulse of the coil, both transistors are simultaneously turned off and the circuit current i_a begins to decrease through diodes D_1, D_2 as shown in Figure 4.

4. STEPPER MOTOR FOR BOTH DIRECTIONS

The following mechanical model in Figure 5 obtained from Simplorer 6 shows a 4-phase step motor. Whose electrical part is modeled by 4 electrical circuits in parallel connection.

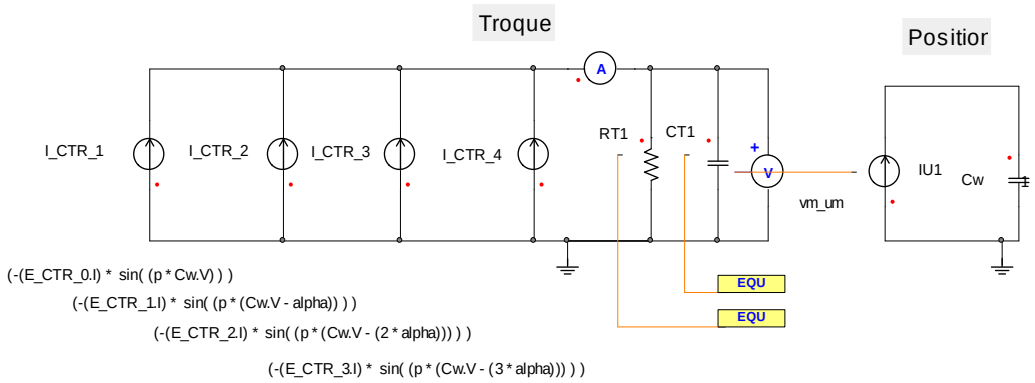

Figure 5: Mechanical part of four phase stepper motor.

There are different ways to model the mechanical part of the motor in Simplorer. Here it is used according to Simplorer 6 an electrical circuit to describe its mechanical behavior. It can be modeled as block diagram as well.

The control signal of the step motor is produced by 3 state machines. One for direction control, e.g. the required step length and moving direction. The others for generating pulse signals, which depends on the moving direction as shown in Figure 6.

By using static transistor model in Simperlor, the logic control signal can be connected directly to the transistor as a switch signal. A static transistor model is good enough to simulate the controlled behavior of the step motor in this case as shown in figure 7. Figure 7 also shows the waveform of the speed, torque and position of both-directional stepper motor.

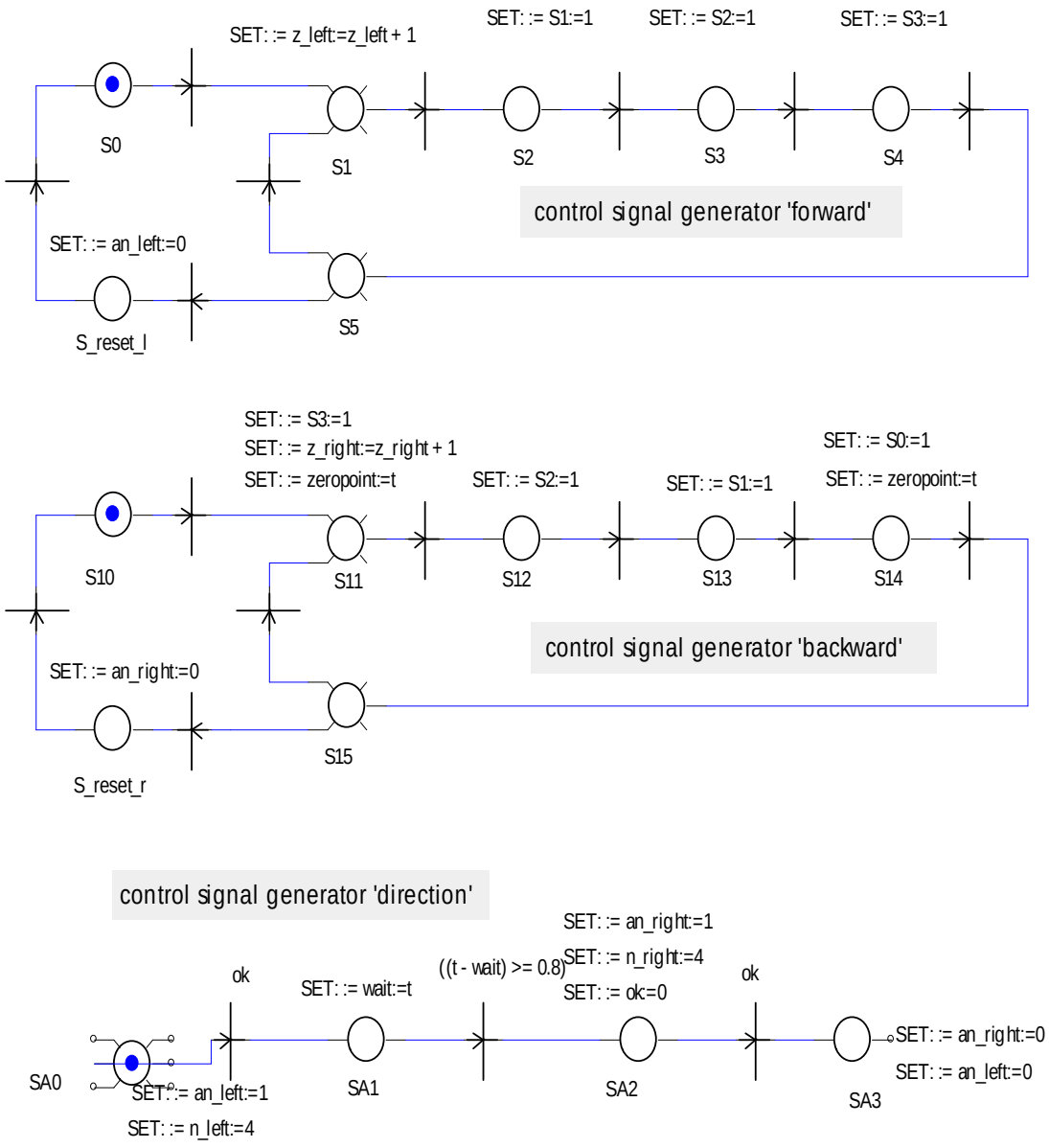

Figure 6: State graph.

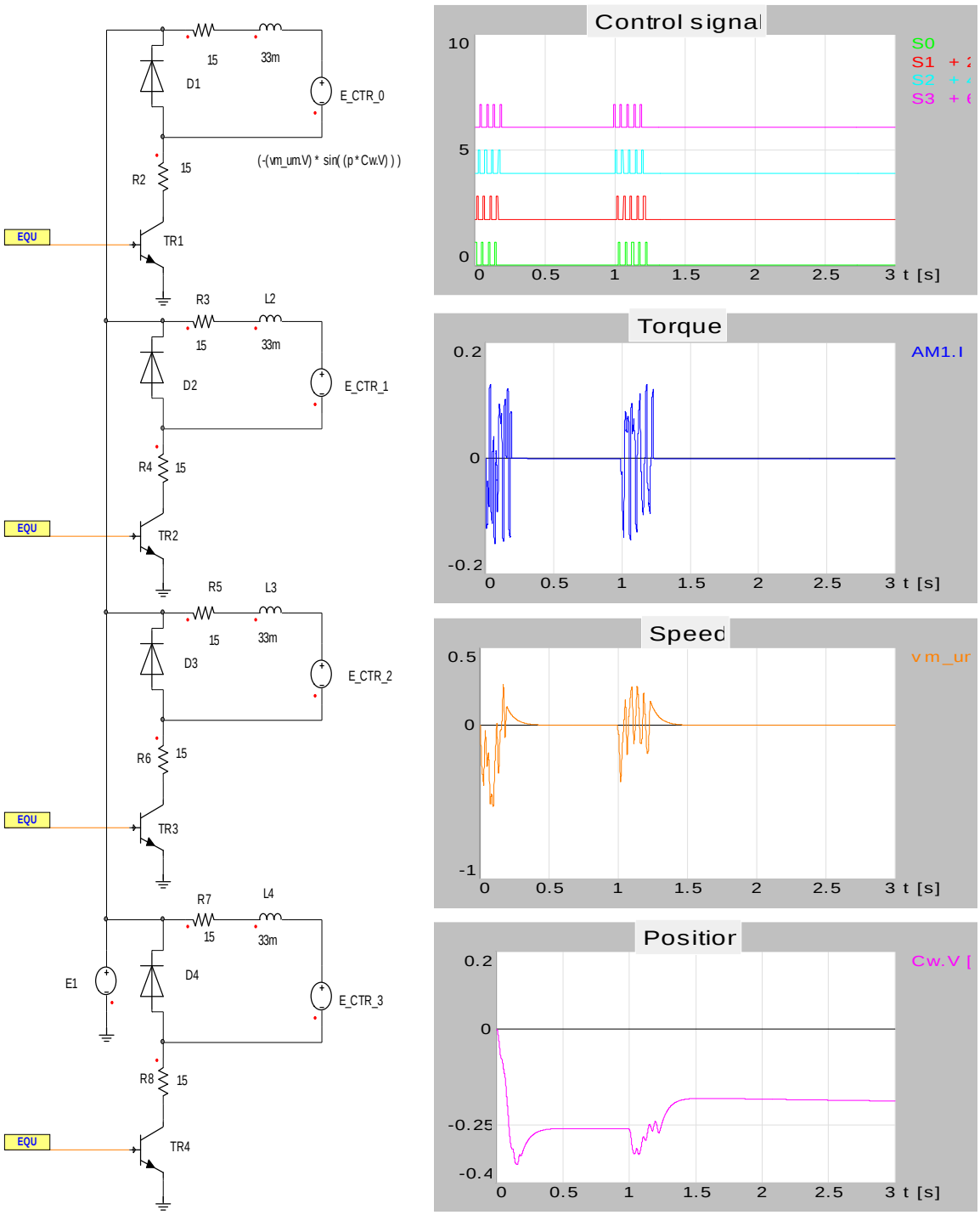

Figure 7: Electrical model and output waveforms.

5. CONCLUSION

The above described application examples of modern control and drive circuits show that performance and efficiency of variable reluctance stepper motors may be remarkably increased without any excessive expense increase like before.

A natural limit against any current increase by using very high power supply as in the bi-level control method is the danger of saturating the iron core and increasing the maximum temperature rise of the motor, due to the power loss in the stator windings. This shows one advantage of the modified chopper control method defined in this paper, which, compared to others, has the motor's power loss within a reasonable limit since the current in the windings is controlled.

The winding current is chopped and limited within a certain limit and this produces a direct proportional and positive effect on the torque. At their power loss limit stepper motors with anti-parallel series four phase chopper control may deliver more torque than stepper motor with other drive circuits.

Furthermore, if a higher torque is not required, one may either reduce the motor size or the power loss by utilizing the chopper control method. It gives only as much voltage as needed and makes the motor to run at as high speed as required and independently from the winding resistance.

On the other hand, the bi-level control method requires higher power supply than other methods which increases the economical costs of the system and the power supply is more expensive because it has to deliver 5 times as much power ($5E_1$ instead of E_1). Furthermore, the current is not limited or controlled anyhow and therefore, the magnetic field is not controlled. Consequently, the torque of the motor is out of control since it is proportional to the current and the magnetic field of the motor's windings.

Dedicated integrated circuits have dramatically simplified stepper motor driving. To apply these ICs designers need little specific knowledge of motor driving techniques, but an under-standing of the basics will help in finding the best solution.

6. REFERENCES

1. E. Walid, TT. Issam, A. Rateb. "A novel topology of delta modulation technique for improving the power factor of AC-DC converters". International journal of engineering (IJE), CSC journals, Volume 4, Issue 1, January/February 2010.

2. M. F. Rahman, A. N. Poo and C. S. Chang. "Approaches to Design of Ministepping Step Motor Controllers and Their Accuracy Considerations". IEEE Trans. Industrial Electronics, vol. IE-32, No. 3, pp. 229-233, August 1985.

3. M. F. Rahman and A. N. Poo. "An Application Oriented Test Procedure for Designing Microstepping Step Motor Controllers". IEEE Trans. Industrial Electronics, vol. 35, No. 4, pp. 542-546, November 1988.

4. P. C. Sen. "Modern Power Electronics". Published by S. Chand & Company LTD. New Delhi, 2004.

5. W. Theodore. "Electrical machines, drives, and power systems", sixth edition. Published by Pearson education international, New Jersey 07458, 2006.

6. W. D. Harries and J. H. Lang. "A simple motion estimation for variable reluctance motors, IEEE Trans. Ind. Appl., pp 237-243, March 1990.

7. P. P. Acarnley. “Stepping Motors: A Guide to Modern Theory and Practice“. IEE Control Engineering Series 19, Peter Peregrin Ltd., 1982.

8. M. F. Rahman and A. N. Poo. “An Application Oriented Test Procedure for Designing Microstepping Step Motor Controllers”. IEEE Trans. Industrial Electronics, vol. 35, No. 4, pp. 542-546, November 1988.

9. D. Carrica, M. A. Funes and S. A. Gonzalea. “Novel Stepper Motor Controller Based on FPGA Hardware Implementation”. IEEE/ASME Trans. Mechatronics, vol. 8, No. 1, pp.120-124, March 2003.

10. P. D. Ziogas, L. Morán, G. Joos, and D. Vincenti. "A refined PWM scheme for voltage and current source converters". IEEE-IAS Annual Meeting, 1990, PP. 997-983.

11. R. Wu, S. B. Dewan, and G. R. Slemon. "Analysis of an AC-to-DC voltage source converter using PWM with phase and amplitude control". IEEE Transactions on industry Applications, vol. 27, No. 2, March/April 1991, pp. 355-364.

12. X. Ruan, L. Zhou, and Y. Yan. "Soft-switching PWM three-level converters". IEEE Transactions on Power Electronics, Vol. 6, No. 5, September 2001, pp. 612-622.

13. M. H. Rashid. “Power Electronics, Circuits, Devices and applications”. Third edition, 2004, Pearson Education, Prentice Hall, Upper Saddle River, NJ 07458.

14. Miftakhutdinov, R. “An Analytical Comparison of Alternative Control Techniques for Powering Next Generation Microprocessors”. TI Seminar, 2002.

15. G. Moschopoulos, P. Jain. "Single-phase single-stage power-factor-corrected converter topologies". IEEE Trans. on Industrial Electronics, vol. 52, no. 1, pp. 23- 35, Feb 2005.

Three Dimensional Bearing Capacity of Shallow Foundations Adjacent to Slopes Using Discrete Element Method

Mona Arabshahi monaarabshahi@gmail.com
Graduate Student of Soil Mechanics and Foundation Engineering
School of Civil Eng., College of Engineering, University of Tehran

Ali Asghar Mirghasemi aghasemi@ut.ac.ir
Associate Professor
School of Civil Eng., College of Engineering
University of Tehran

Ali Reza Majidi armajidi@gmail.com
Ph.D. of Soil Mechanics and Foundation Engineering
Mahab Ghodss Consulting Engineers

ABSTRACT

In the current study, an effort is made to determine three dimensional bearing capacity of a shallow foundation adjacent to a slope using discrete element method. The soil mass under the footing is modeled as discrete blocks connected with a set of normal and shear springs called Winkler springs. In order to define the geometry of the failure surface of the soil, six independent angles are considered, which will be obtained by trial and error. So, the failure surface is not fixed and can be changed by different characters.

The purpose of the paper is to determine the three dimensional bearing capacity coefficients of rectangular foundations which are placed adjacent to a slope. In order to get to such a scope a discrete element program called BCAP3D (Bearing capacity analysis program in 3D) is employed. The result is presented in relative graphs, versus the ratio ($\frac{x}{B}$), for each foundation aspect ratio ($\frac{L}{B}$). Besides, a comparison is made between the current method with other methods used in the same field.

Keywords: 3 Dimensional, Bearing Capacity, Shallow Foundations/Footings, Discrete Element Method.

1. INTRODUCTION

1-1 Field of The Research

Bearing capacity of foundations has always been one of the most interesting research subjects in geotechnical engineering. In such a field of study, extensive efforts have been made for bearing capacity in two dimensions. It seems that 2D theoretical approaches have reached to a relatively satisfactory level for ordinary loading and soil conditions. Considering that real foundations are not infinitely long and their failure mechanism is certainly three dimensional, it is necessary to study the real conditions and try to develop analytical 3D estimations of the bearing capacity.

Among the researches in 3D bearing capacity, a few of them consider the effect of the ground inclination or a nearby slope in reducing the ultimate load of the footing, which is the main subject of the current paper.

1-2 Previous Studies

Evaluation of the 3D bearing capacity of shallow foundations is usually assessed by introducing experimental and empirical shape factors into the ordinary 2D equations for the strip footings developed by researchers such as Meyerhof [1], Terzaghi and Peck [2], Hansen [3], de Beer [4], Vesic [5], and the others.

The general bearing capacity relationship suggested by these researches can be expressed as:

$$q_{ult} = cN_c + qN_q + 0.5\gamma BN_\gamma \quad (1)$$

Where N_c, N_q and N_γ are the bearing capacity coefficients in two dimensional state. For considering the effect of the lateral surfaces in three dimensional conditions, the experimental related shape factors will be used.

In order to employ analytical methods in such a research, Shield and Drucker [6] presented a theoretical evaluation of 3D bearing capacity of rectangular foundations on homogeneous clay ($\varphi = 0$) by means of upper and lower bound solutions. Nakase [7] used a limit equilibrium method and assumed cylindrical sliding surfaces for rectangular footings on normally consolidated clays. Narita and Yamaguchi [8], presented a three dimensional analysis of bearing capacity of rectangular foundations by means of the method of slices, assuming that sliding surfaces are composed of a set of log-spirals with different initial radii. There are plenty of other researches in different conditions such as works of Ugai [9], Michalowski [10], Michalowski and Dawson [11], Zhu and Michalowski [12] and Salgado et al. [13].

Askari and farzaneh [14] used an upper bound method to determine the bearing capacity of strip foundations near slopes. Sarma and Chen [15] also studied the same problem during earthquake using a limit equilibrium technique.

1-3 History of The Discrete Element Method

Cundall and Strack [16] established a Discrete Element Method to study the micromechanical behaviour of granular materials by modelling assemblies of two dimensional circular particles. In this method each particle is considered as a distinct (discrete) element.

The new concept of DEM presented here, falls within the framework of the limit equilibrium methodology. In two dimensional state, this method was presented by Chang for analysis of bearing capacity of foundations [17], slope stability [18] and retaining walls [19]. Using this method, soil mass is modelled as a system of blocks connected together by elasto-plastic Winkler springs. So in the current method, every block is considered as a discrete element.

The former state of DEM is an explicit method and the latter one is an implicit method.

1-4 Using DEM for 3D bearing capacity

Majidi and Mirghasemi [20] employed the DEM to study the 3D bearing capacity of rectangular foundations. The same method is used here to obtain the 3D bearing capacity of footings adjacent to slopes.

2. DISCRETE ELEMENT MODEL

The method used in order to achieve the 3D bearing capacity coefficients of a foundation is briefly introduced in here.

2-1 General Information and main equations

To determine the three dimensional bearing capacity of rectangular shallow foundations by DEM, it is assumed that the soil mass beneath the footing consists of several discrete blocks connected with an infinite number of Winkler springs, as shown in Fig. 1. As the load applied on the footing increases, these blocks are going to slip in order to define the failure mechanism.

Each group of Winkler springs consists of three sets of springs in different orthogonal directions (Fig.2). One set of springs is located in the direction normal to the contact surface to simulate the normal stiffness of the soil (E) and the two other sets are placed within the contact surface, perpendicular to each other, to behave as shear stiffness (G) of the soil.

The behaviour of the normal and shear springs is assumed to be Elasto-Plastic. As shown in Fig. 3, the normal springs do not yield in compression. However, in tension they would yield at the tensile capacity.

Also, based on Mohr-Coulomb failure criteria, the shear springs yield when the shear strength (τ_p) is reached, as:

$$\tau_p = c + \sigma_n \tan\varphi \quad (2)$$

The initial values of stiffness in the normal and shear directions between blocks can be estimated using Young's modulus (E) and shear modulus (G), respectively [18]. According to the soil behaviour, no tension will appear in normal spring and just shear springs will result in failure of the soil when they reach their shear resistance. Whenever the force in a shear spring reaches its ultimate value, the initial shear stiffness (k_{shear}) will be substituted by the reduced secant shear stiffness (k'_{shear}). (Fig. 3-b)

The present method can be used to model progressive failure of a sliding soil mass. As the applied load increases, the induced stresses in springs may exceed the allowable stresses. When the shear stress is beyond the admissible stress at an interface, the local factor of safety is set to be 1 for the interface and the iteration process redistributes the excessive amount of stress to the neighbouring blocks. The iterative procedure is carried out until the stresses at all interfaces of blocks are compatible with their deformations and completely satisfy the stress-displacement relationships.

In discrete element method, the constraint information is given on the centers of blocks. So, it is necessary to determine the relative displacement of two adjacent blocks according to the center of their interface. Due to the relative displacement between two neighbouring blocks, the springs are deformed and their stresses can be calculated. By integrating on each surface of the blocks, the relative force will be obtained. The forces acting on all sides of a block should satisfy the force and displacement equilibrium requirement. The relationship between the forces and the displacements for all blocks can be written as:

$$\{f\} = [K]\{U\} \quad (3)$$

Where [K] is the global stiffness of the system and the vectors {*f*} and {U} consist of body forces and displacements for all blocks, respectively.

Solving the equation (3), normal and shear forces between blocks will be obtained and so, the overall safety factor of the system can be defined through equation (4).

$$S.F = \frac{\sum \tau_{pi} A_i}{\sum \sqrt{(\tau_{si})^2 + (\tau_{ti})^2} . A_i} \quad (4)$$

Where τ_{pi} is the shear strength of the soil and τ_{si} and τ_{ti} are the existing shear stresses on the failure surface.

2-2 The Geometry of The Failure Surface

The failure mass of the soil below the footing consists of three zones similar to the classical 2D bearing capacity failure surface (Mirghasemi and Majidi, [21]). Each of them can be divided into several wedges as shown in Fig. 4.

The failure mechanism contains of an active zone below the footing (zone I), which is pushed downward into the soil mass and a passive wedge (zone III) moves laterally. The transition between downward movement of the active zone and lateral movement of the passive zone takes place through the radial shear zone (II). The shape of the failure surface of zone (II) is assumed to be a logarithmic spiral. The shape of the failure surface is a function of the footing width (B) and length (L), the internal friction angle of the underlying soil (φ) and the six independent angles of α_1, α_2, α_3, α_4, θ_1 and θ_2.

The angles θ_1 and θ_2 as shown in the Fig. 4-b, determine the inclination of lateral failure surfaces in the three dimensional space. The absolute values of θ_1 and θ_2 are assumed to be identical ($|\theta_1 = \theta_2|$) due to the symmetry in the foundation geometry and loading.

These six angles are not predefined and will be obtained by iteration in order to get the most critical failure surface. So, a large number of failure surfaces would be examined to determine the ultimate bearing capacity of the footing.

2-3 General Assumptions

In order to determine the ultimate bearing capacity of a shallow foundation adjacent to a slope by DEM, it is necessary to clarify the assumptions used in the analyses. They can be mentioned as:

1. The blocks are rigid and just relative displacement of adjacent blocks will be taken into account.
2. Every two adjacent blocks will remain in contact and no separation would be occurred.
3. The load is applied to a rectangular rigid foundation with the dimensions $B \times L$.
4. Loading is vertical and centric.
5. The general shear failure will occur in the soil mass.
6. The dry soil density is used.
7. There is a distance (x) between the footing and the edge of the slope which its inclination angle is β.
8. In order to obtain the 3D bearing capacity coefficients, the superposition method has been taken into account.
9. The surcharge applying to the ground is defined just on one side of the foundation where the failure mechanism would be constructed. No surcharge will be considered on the inclined ground surface.
10. The radial shear zone (II) is assumed to be divided into 10 blocks. Also, it's better for zones (I) and (III) to model as a single block due to their non-shear behaviour [20].

Fig.5 shows the position of a failure mechanism in the relation to the slope inclination.

3. COMPARISON TO OTHER METHODS

3-1 Compare to Classical methods

To compare the 3D bearing capacity of shallow foundation near the slopes resulted from DEM with other methods, the results of two classic semi-empirical methods which presented by Hansen [3] and Vesic [5] are used. Fig. 6 to Fig. 8 shows the bearing capacity of a footing on top of a slope of inclination (β) where: $\frac{x}{B} = 0$.

3-2 Compare to AASHTO LRFD Bridge Design Specification

AASHTO LRFD bridge design specifications suggests some empirical factors and graphs to determine the bearing capacity of foundations near slopes, for cohesionless soils and for saturated clays, separately. [22]
A comparison between the ultimate bearing capacities resulted from DEM and LRFD specifications is made and shown in Fig. 9 to Fig. 12.

3-3 Compare to experimental results

A comparison is made between the bearing capacity resulted from DEM and an experimental research of a square footing near a slope [23]. A footing of $10\text{cm} \times 10\text{cm}$ is places near a slope of 25° inclination. The soil properties are:

$\varphi = 32°, c = 0.2\ {}^{ton}/_{m^2}$

Table 1 shows the comparison between these two methods.

4. THREE DIMENSIONAL BEARING CAPACITY COEFFICIENTS

A nearby slope will definitely decrease the bearing capacity of a rectangular foundation. In the current study, the bearing capacity coefficients are achieved using DEM with mentioned assumptions. The results are presented for each of the coefficients versus the dimensionless quantity ($\frac{x}{B}$), for different foundation aspect ratios.

The bearing capacity can be obtained through the equation:

$$q_{ult} = cN_{cm} + qN_{qm} + 0.5\gamma BN_{\gamma m} \quad (5)$$

In which N_{cm}, N_{qm} and $N_{\gamma m}$ are the modified 3D bearing capacity coefficients of the rectangular foundation near a slope.

4-1 The coefficient of soil cohesion (N_{cm})

In order to have N_{cm}, we can obtain the bearing capacity of a weightless soil and disregarding the surcharge on the ground. Figs. 13 to 24 indicate the factor of N_{cm}.

4-2 The coefficient of soil weight ($N_{\gamma m}$)

$N_{\gamma m}$ can be defined as the bearing capacity of a cohesionless soil of density equals to $2\ ton/m^3$ and disregarding the surcharge on the ground. Figs. 25 to 36 indicate the factor of $N_{\gamma m}$. These Figures are provided for the situation: $\beta \leq \varphi$.

4-3 The coefficient of surcharge (N_{qm})

To obtain N_{qm}, the weight and cohesion of the soil should be disregarded. Figs. 37 to 40 indicate the factor of N_{qm}, for all the slope inclination.

The analyses indicate that N_{qm} is hardly a function of the slope inclination and for various slope inclinations N_{qm} varies in a small range. This is because of the definition of the surcharge in the current method.

As the surcharge on the ground is defined to the edge of the slope, for a certain ($\frac{x}{B}$) the amount of surcharge would be constant for every quantity of slope inclination. So, the only difference is a small decrease in the failure length of the third region in the failure mechanism, as the angle of the slope inclination increases.

4-4 Influence of The Foundation Aspect Ratio

An analysis is made to study the effect of the foundation aspect ratio on the bearing capacity of the footing. As it is shown in Fig. 41 and 42, increasing in footing aspect ratio ($\frac{L}{B}$) results in the decrease of the bearing capacity. This is because of the fact that as the foundation aspect ratio increases, the influence of the lateral failure surfaces on the bearing capacity decreases. And finally, it reaches its 2D ultimate value.

5. SUMMARY AND CONCLUSIONS

In this research, analyses based on Discrete Element Method (DEM) are carried out for determining three dimensional bearing capacity coefficients of shallow foundations near slopes. By determining the parameters through relative sensitivity analyses, the final analyses are made to get 3D bearing capacity coefficients. Besides, a comparison to other methods that can determine the 3D bearing capacity of a shallow foundation near a slope is made.

The results obtained from the present study can be summarized as follows:

1. The results of the present method are to some extent in accordance with classical semi-empirical results proposed by earlier researchers such as Hansen and Vesic. The present DEM will results in less bearing capacities compare to the classical methods.
2. DEM will results in higher value of bearing capacities comparing to AASHTO LRFD specifications. However, the difference isn't a great deal.
3. For higher values of foundation aspect ratios, the comparison between different methods results in less differences for bearing capacities.

4. Just like other methods, the bearing capacity coefficients obtained by DEM are highly dependent on the internal friction of the soil, especially for φ values greater than 30°.

5. For each value of the slope inclination, there is a critical x value which for $x \geq x_{critical}$ the slope has no effect on the failure mechanism and bearing capacity of the foundation. This critical distance can be found in the graphs provided for bearing capacity coefficients.
6. The critical x described above, will decrease by decreasing in the soil friction angle. It also will increase by increasing in foundation aspect ratio.
7. As can be seen in the graphs, for slope inclination more than 30°, N_c will decrease more slowly in comparison to inclinations less than 30°.

6. Tables and Figures

Difference (%)	Q (DEM) $(^{ton}/_{m^2})$	Q (experimental) $(^{ton}/_{m^2})$	x/B	Soil density $(^{ton}/_{m^2})$
13.8	9.05	10.5	0.3	1.61
11.2	7.1	8.0	0.3	1.51

Table. 1: Comparison between DEM and experimental bearing capacity

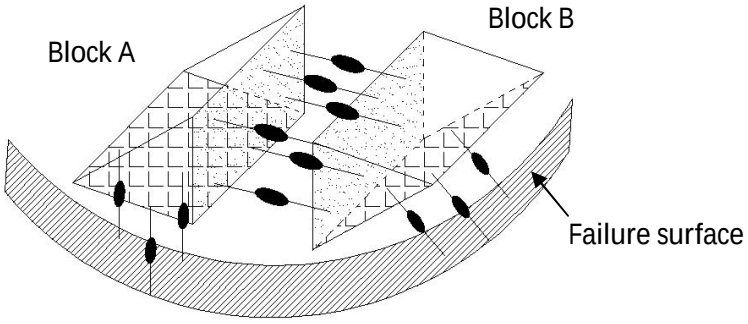

Fig.1: Connection of the blocks with the Winkler springs

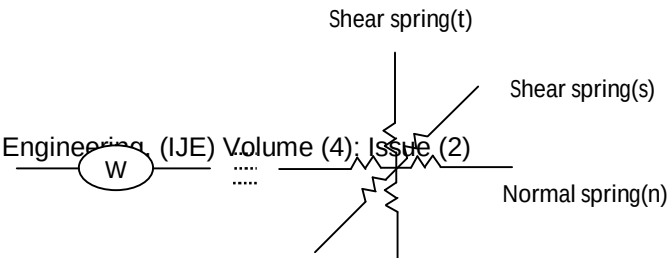

Fig.2: A Winkler spring is consists of three perpendicular springs

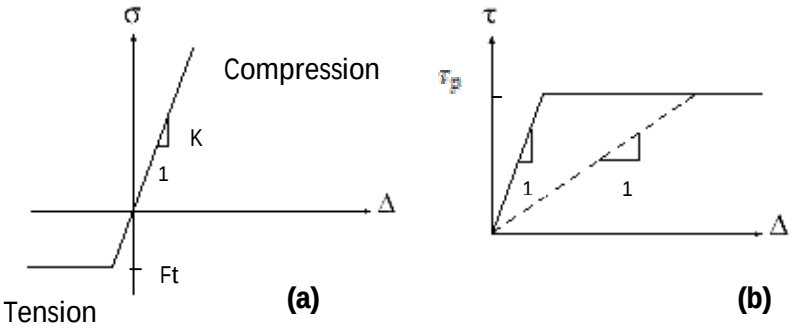

Fig.3: The behaviour of normal (a) and shear (b) springs

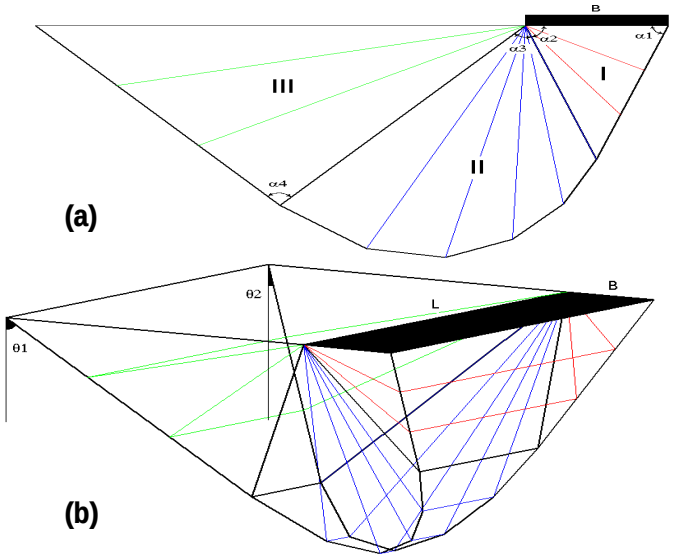

Fig.4: The failure surface below the footing (a) 2D view (b) 3D view

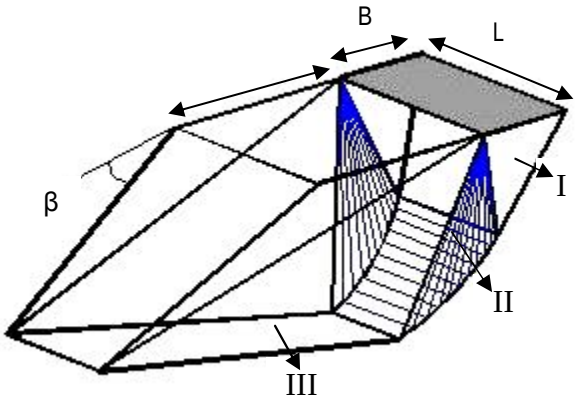

Fig.5: The position of the footing and the slope

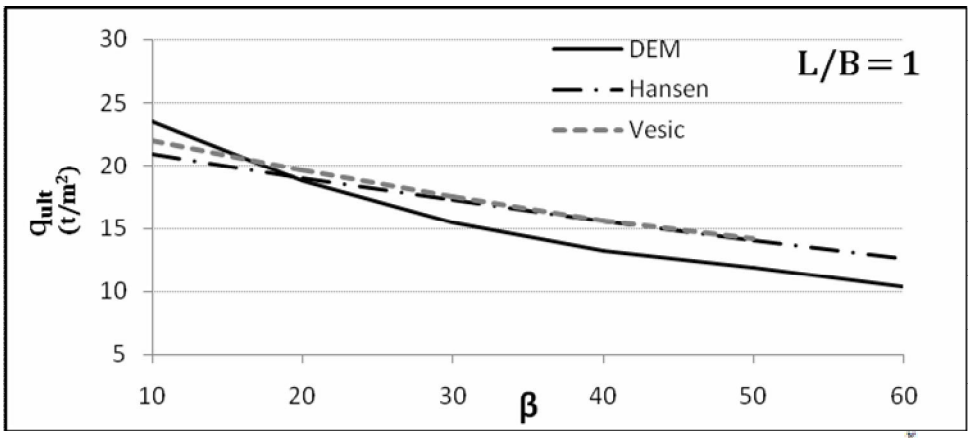

Fig. 6: Comparison of the bearing capacity resulted from DEM and Classic methods ($\frac{\kappa}{B} = 0, \varphi = 20$)

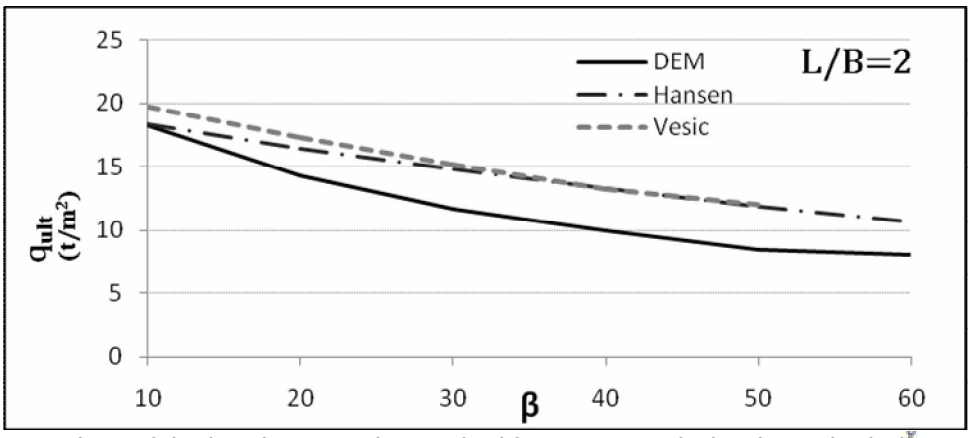

Fig. 7: Comparison of the bearing capacity resulted from DEM and Classic methods ($\frac{\kappa}{B} = 0, \varphi = 20$)

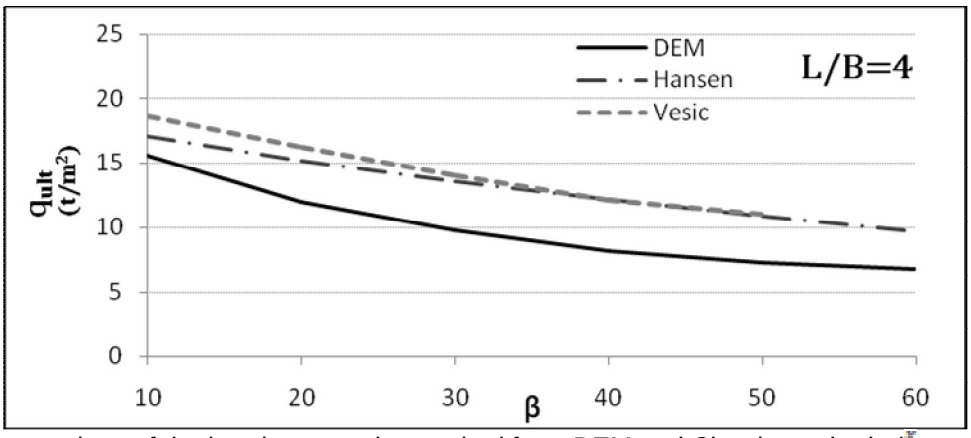

Fig. 8: Comparison of the bearing capacity resulted from DEM and Classic methods ($\frac{x}{B} = 0, \varphi = 20$)

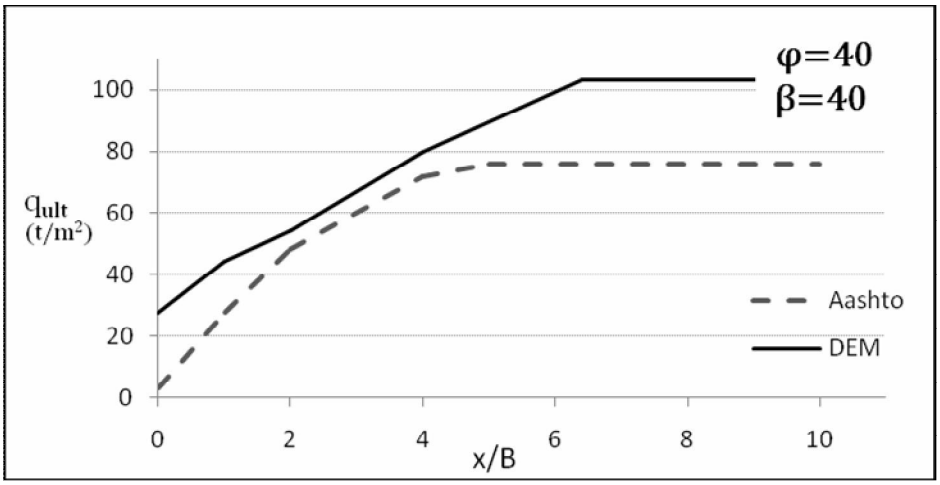

Fig. 9: Comparison of the bearing capacity of cohesionless soil resulted from DEM and AASHTO ($\frac{L}{B} = 2$)

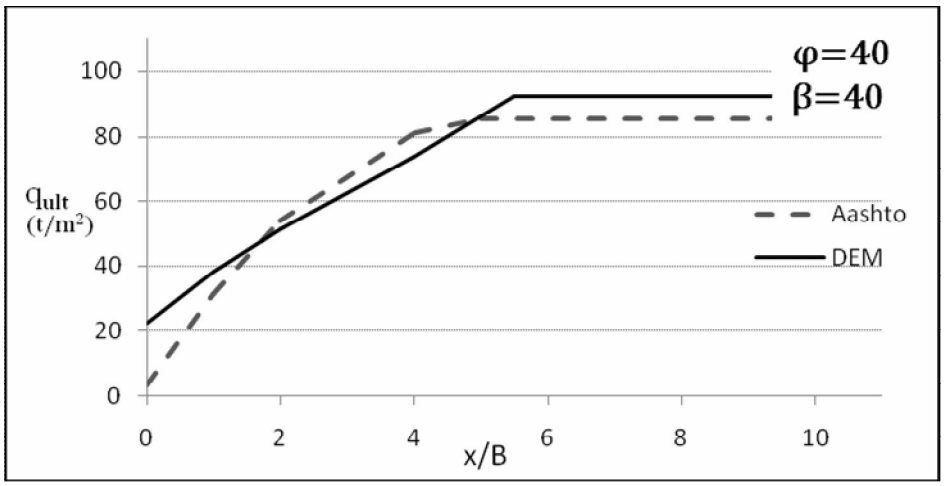

Fig. 10: Comparison of the bearing capacity of cohesionless soil resulted from DEM and AASHTO ($\frac{L}{B} = 4$)

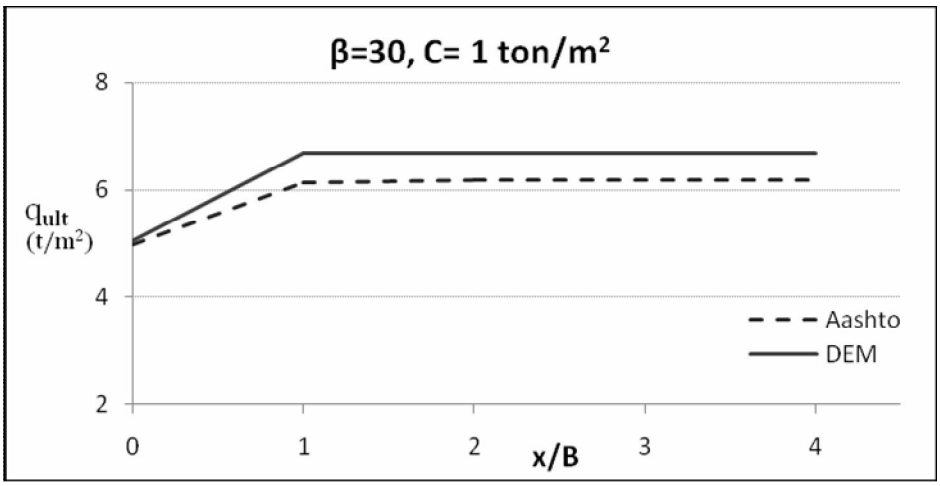

Fig. 11: Comparison of the bearing capacity of saturated clay resulted from DEM and AASHTO ($\frac{L}{B} = 1$)

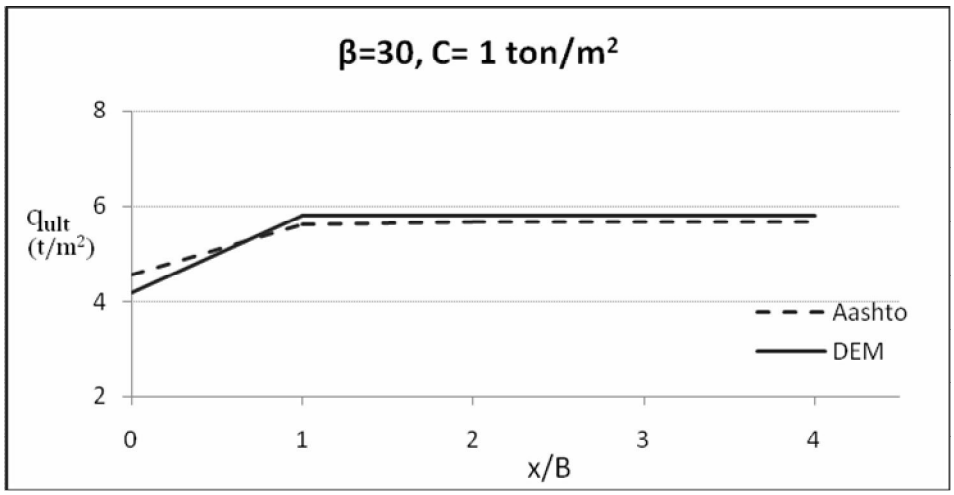

Fig. 12: Comparison of the bearing capacity of saturated clay resulted from DEM and AASHTO ($\frac{L}{B} = 2$)

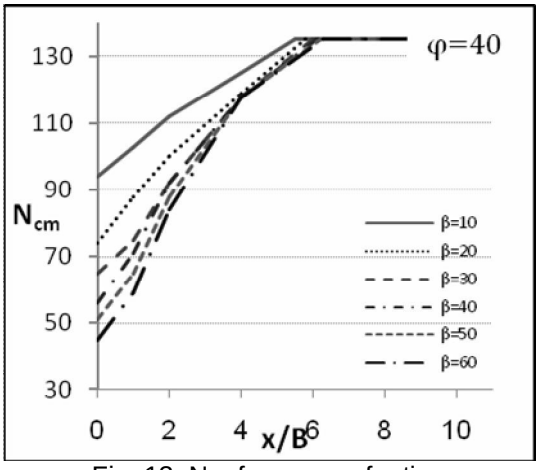

Fig. 13: N_{cm} for square footing

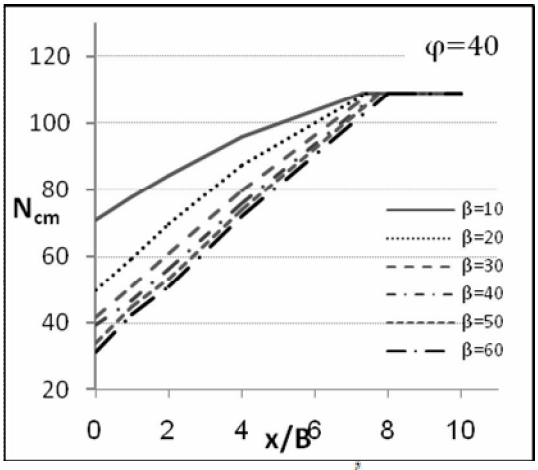

Fig. 16: N_{cm} for ($\frac{L}{B} = 2$)

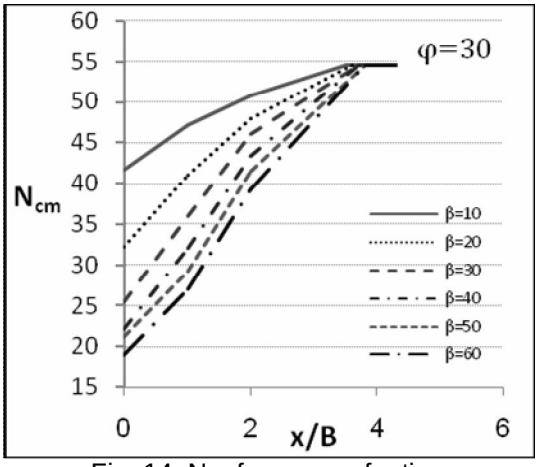

Fig. 14: N_{cm} for square footing

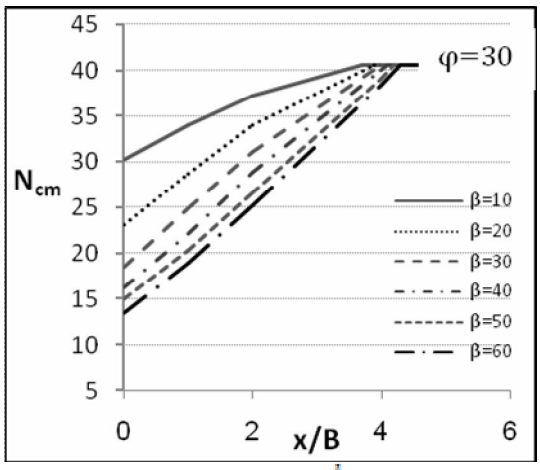

Fig. 17: N_{cm} for ($\frac{L}{B} = 2$)

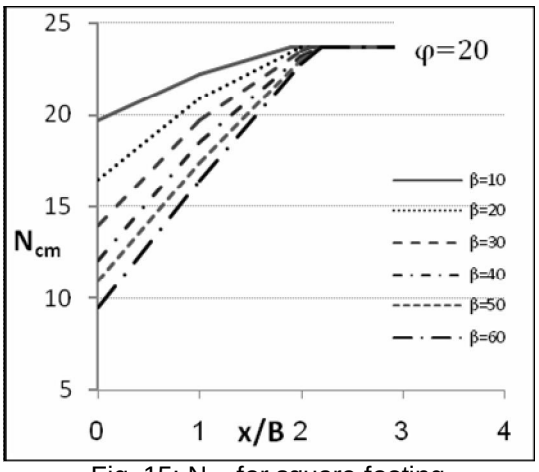

Fig. 15: N_{cm} for square footing

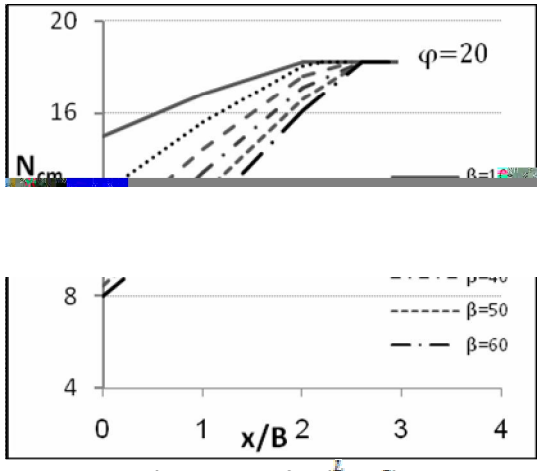

Fig. 18: N_{cm} for ($\frac{L}{B} = 2$)

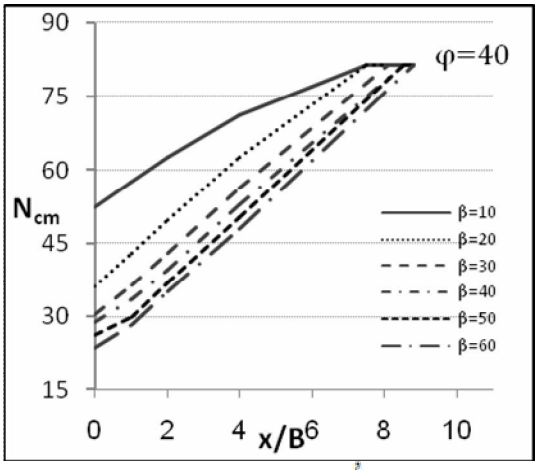

Fig. 19: N_{cm} for ($\frac{L}{B} = 4$)

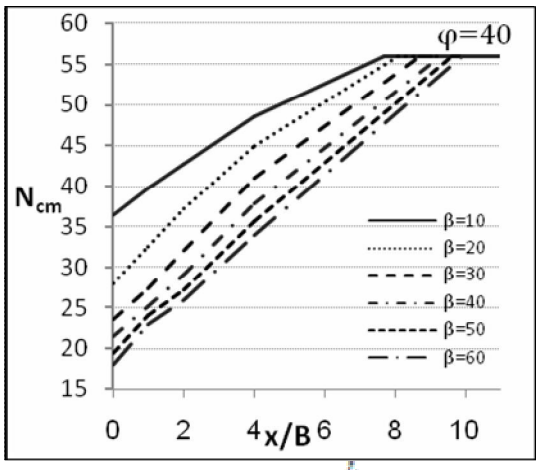

Fig. 22: N_{cm} for ($\frac{L}{B} = 10$)

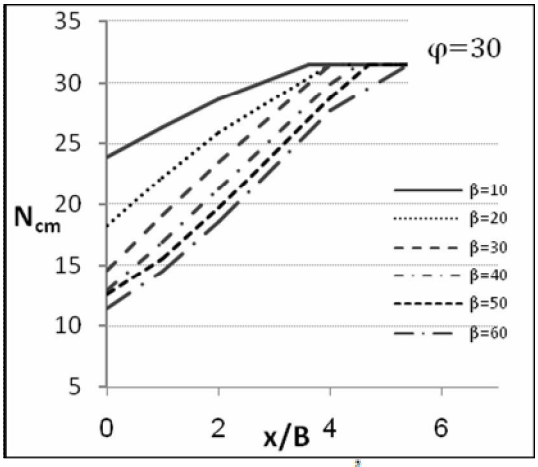

Fig. 20: N_{cm} for ($\frac{L}{B} = 4$)

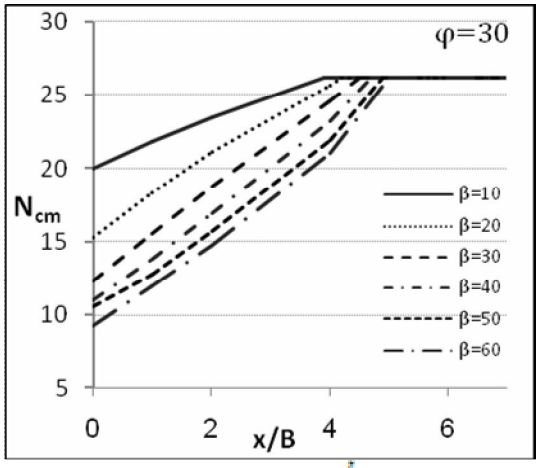

Fig. 23: N_{cm} for ($\frac{L}{B} = 10$)

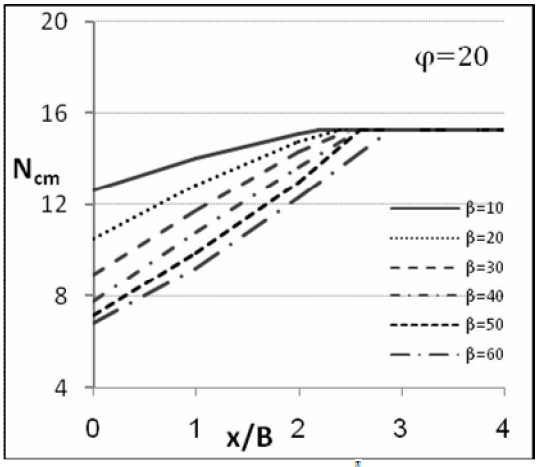

Fig. 21: N_{cm} for ($\frac{L}{B} = 4$)

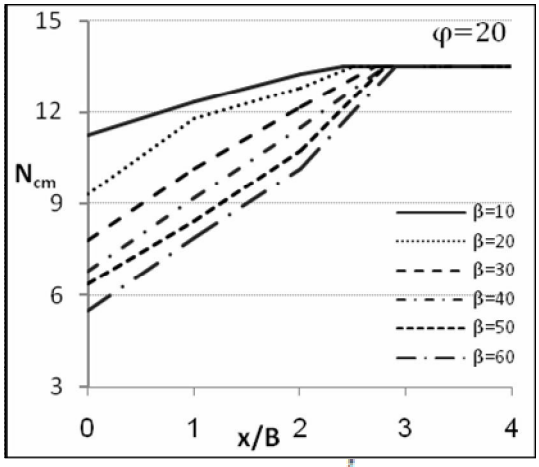

Fig. 24: N_{cm} for ($\frac{L}{B} = 10$)

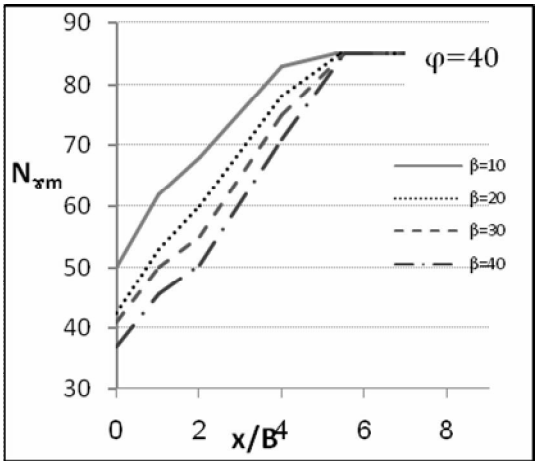

Fig. 25: $N_{\gamma m}$ for square footing

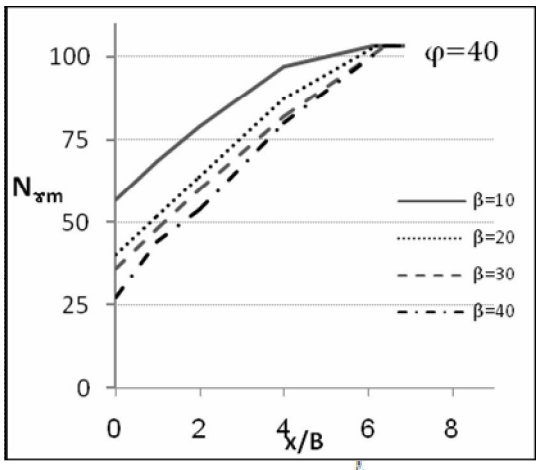

Fig. 28: $N_{\gamma m}$ for ($\frac{L}{B} = 2$)

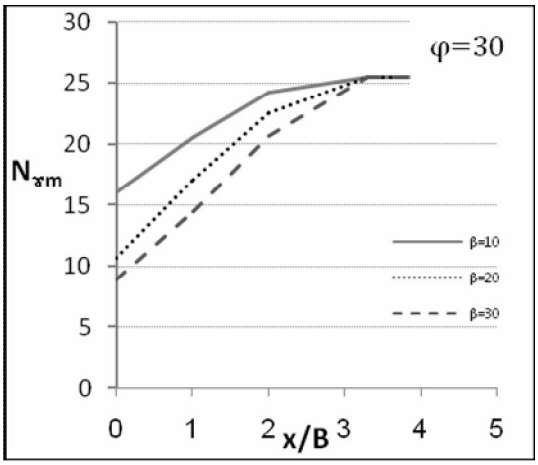

Fig. 26: $N_{\gamma m}$ for square footing

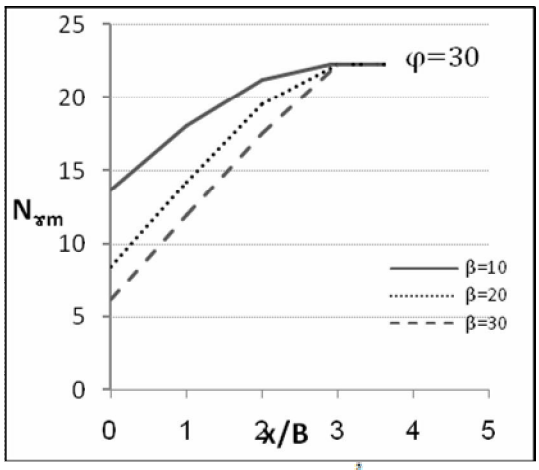

Fig. 29: $N_{\gamma m}$ for ($\frac{L}{B} = 2$)

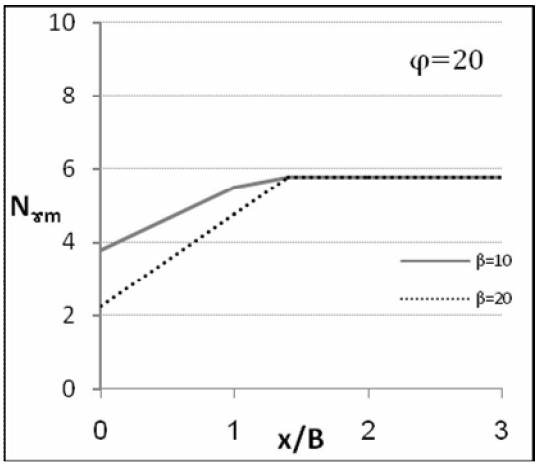

Fig. 27: $N_{\gamma m}$ for square footing

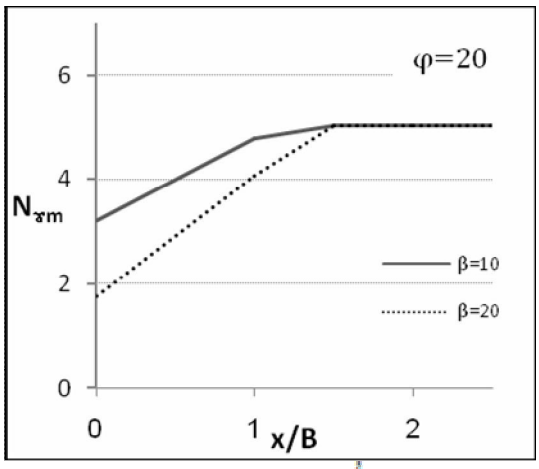

Fig. 30: $N_{\gamma m}$ for ($\frac{L}{B} = 2$)

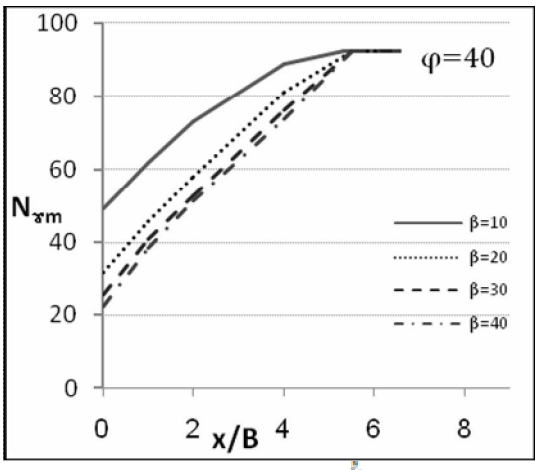

Fig. 31: $N_{\gamma m}$ for ($\frac{L}{B} = 4$)

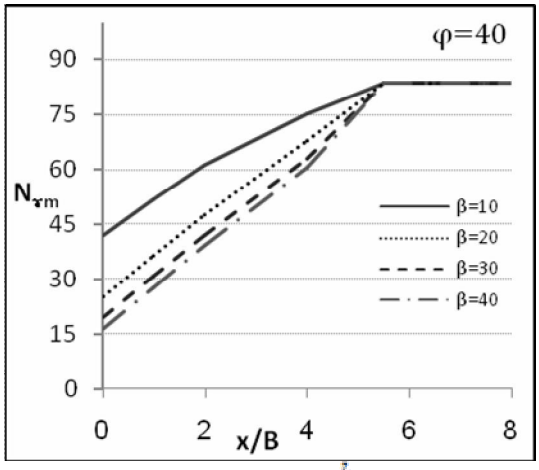

Fig. 34: $N_{\gamma m}$ for ($\frac{L}{B} = 10$)

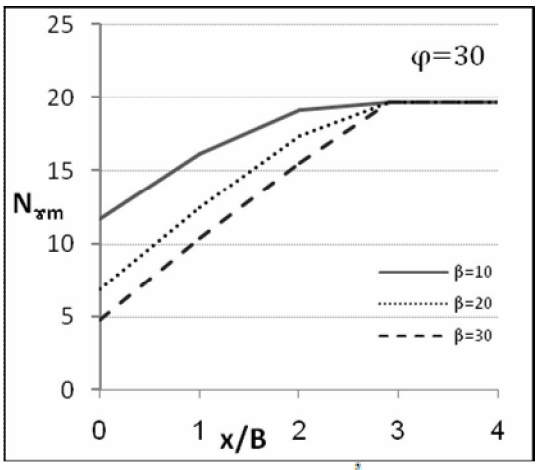

Fig. 32: $N_{\gamma m}$ for ($\frac{L}{B} = 4$)

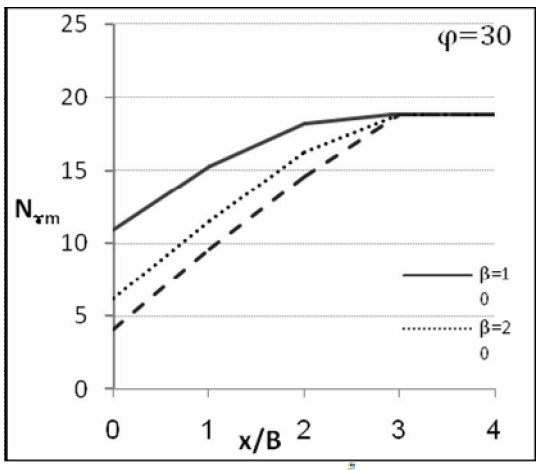

Fig. 35: $N_{\gamma m}$ for ($\frac{L}{B} = 10$)

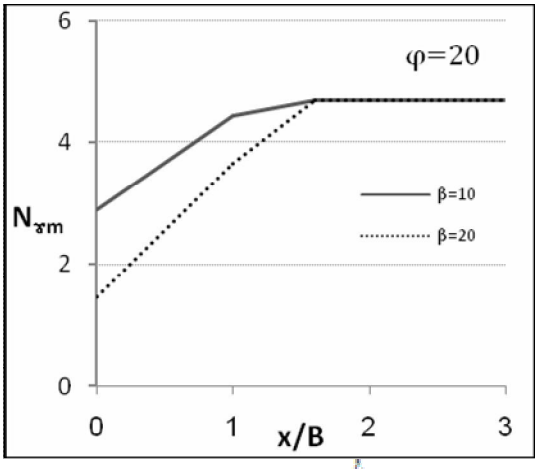

Fig. 33: $N_{\gamma m}$ for ($\frac{L}{B} = 4$)

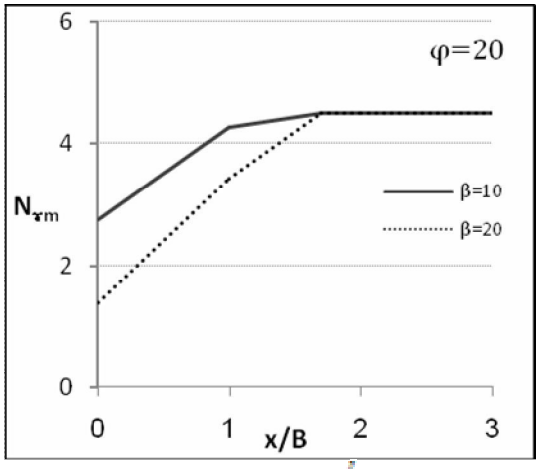

Fig. 36: $N_{\gamma m}$ for ($\frac{L}{B} = 10$)

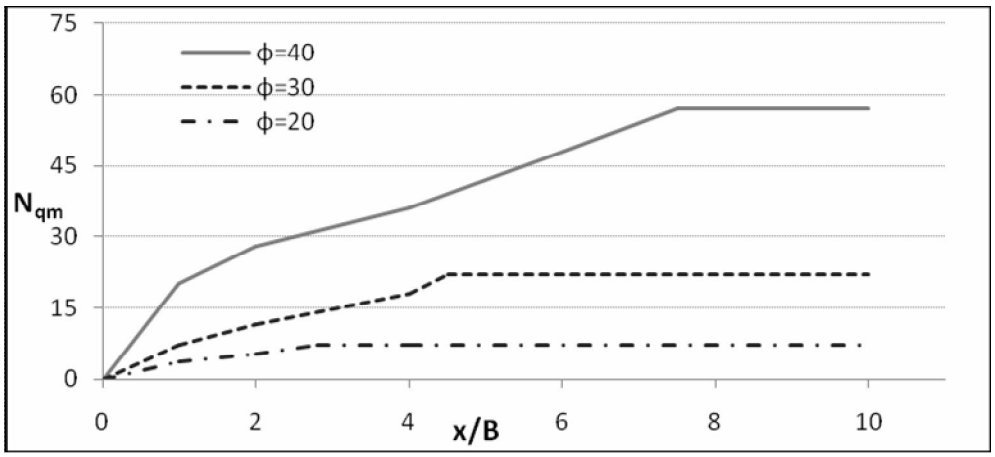

Fig. 37: N_{qm} for square footing

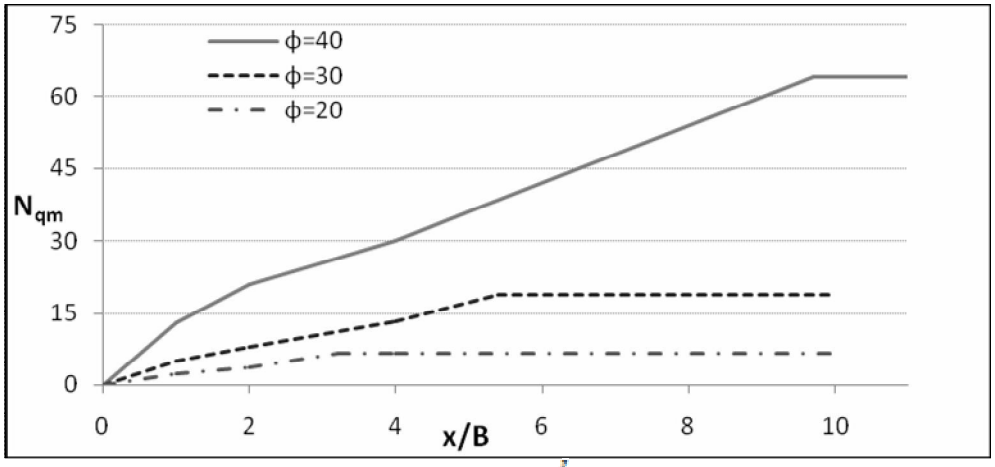

Fig. 38: N_{qm} for ($\frac{z}{B} = 2$)

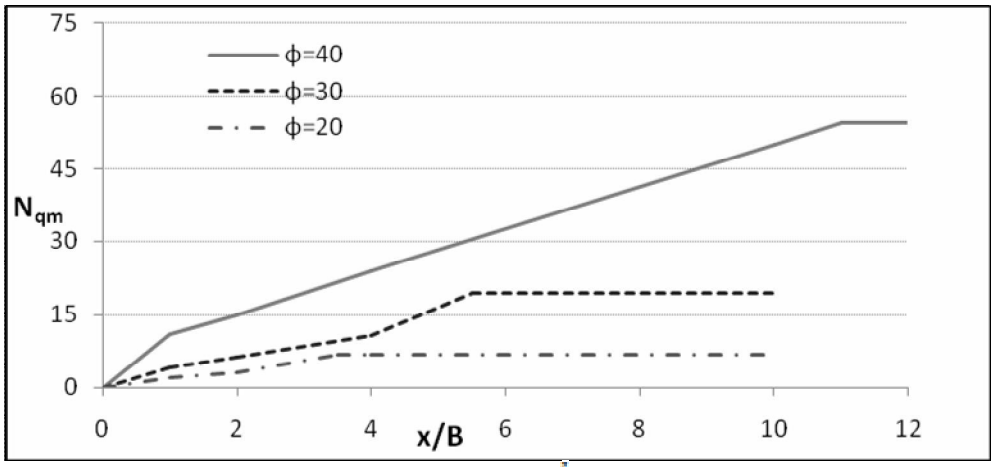

Fig. 39: N_{qm} for ($\frac{z}{B} = 4$)

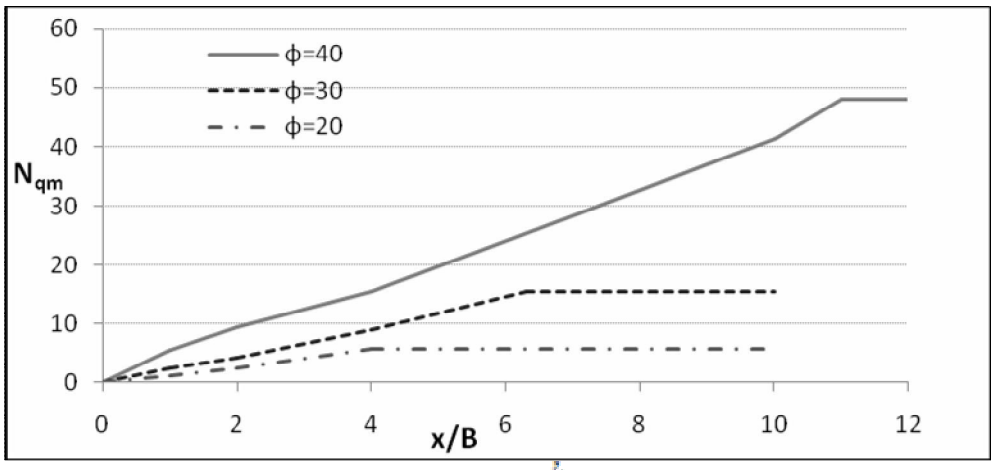

Fig. 40: N_{qm} for ($\frac{L}{B} = 10$)

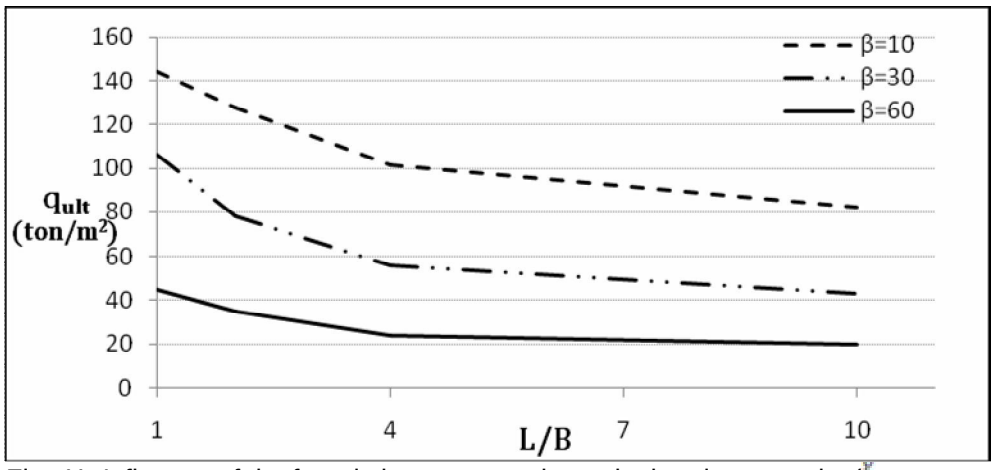

Fig. 41: Influence of the foundation aspect ratio on the bearing capacity ($\frac{x}{B} = 0, \varphi = 40°$)

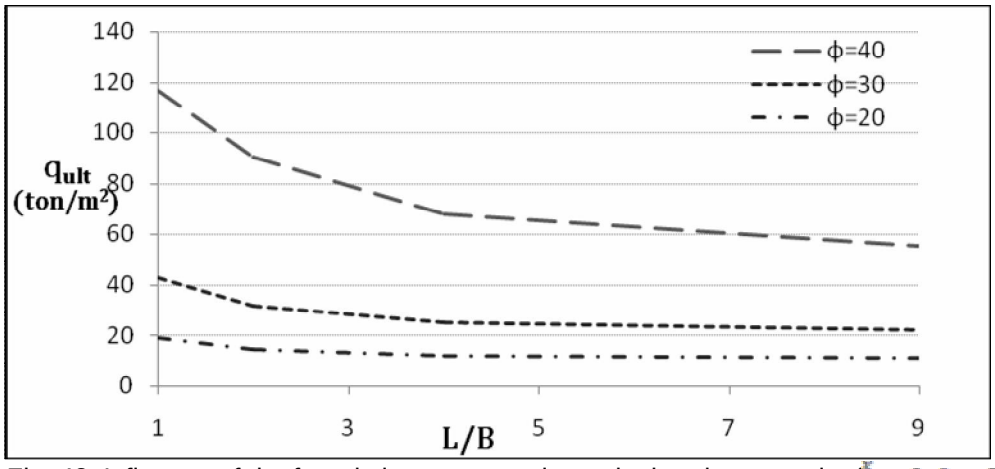

Fig. 42: Influence of the foundation aspect ratio on the bearing capacity ($\frac{x}{B} = 0, \beta = 20°$)

7. REFERENCES

[1] G. G. Meyerhof, “Some Recent Research on the Bearing Capacity of Foundations.” *Canadian Geotech. J.*, 1(1):16-26, 1963.

[2] K. Terzaghi and R. B. Peck, “*Soils Mechanics in Engineering Practice*,” J.Wiley, New York. (1967)

[3] J.B. Hansen, “A Revised and Extended Formula for Bearing Capacity.” *Danish Geotech. Inst. Bulletin,* No. 28, Denmark. 1970.

[4] E.E. De Beer, “Experimental determination of shape factors and the bearing capacity factors of sands,” *Géotechnique,* 20(4) :387-411, 1970.

[5] A.S. Vesic, “Analysis of Ultimate Loads of Shallow Foundations.” *J. of Soil Mech. and Fndn Div.* ASCE, 99(SM1): 45-73, 1973.

[6] R.T. Shield and D.C., Drucker, “The application of limit analysis to punch-indentation problems.” *J. of Appl. Mech.,* ASCE: 453-460, 1953.

[7] A. Nakase, “Bearing capacity of rectangular footings on clays of strength increasing linearly with depth.” *Soils and Foundations*, 21(4): 101-108, 1981.

[8] K. Narita and H.Yamaguchi, “Three-dimensional bearing capacity analysis of foundations by use of a method of slices.” *Soils and Foundations*, 32(4): 143-155, 1992.

[9] K. Ugai, “Bearing capacity of square and rectangular footings on nonhomogeneous clays.” *J. of JSSMFE*, 25(4): 179-185, 1985.

[10] R.L. Michalowski, “Upper-bound load estimates on square and rectangular footings.” *Géotechnique,* 51(9): 787-798, 2001.

[11] R.L. Michalowski, and E.M. Dawson, “Three-dimensional analysis of limit loads on Mohr-Coulomb soil.” *Fndn of Civ. and Inv. Eng., No.* 1: 137-147, 2002.

[12] M. Zhu and R.L. Michalowski, “Shape Factors for Limit Loads on Square and Rectangular footings.” *J. of Geotech. and Geoenv. Eng. ASCE,* 131, No.(2): 223-231, 2005.

[13] R. Salgado, A.V Lyamin, S.W. Sloan, and H.S. Yu, “Two- and three-dimensional bearing capacity of foundations in clay.” *Géotechniqu,* 54(5): 297-306, 2004.

[14] F. Askari and O. Farzaneh, “Upper-bound solution for seismic bearing capacity of shallow foundations near slopes”. Géotechnique, 53(8): 697-70, 2003.

[15] S. K. Sarma and Y. C. Chen, “ Bearing capacity of strip footings near sloping ground during earthquakes”. Proc. 11th world conf. on earthquake engineering, 1989.

[16] P.A. Cundall and O.D.L. Strack, “A discrete numerical model for granular assemblies.” *Géotechnique,* 29(1): 47-56, 1979.

[17] C.S. Chang, “Discrete element method for bearing capacity analysis.” *Comput. and Geotech.,* 12: 273-288, 1991.

[18] C.S. Chang, “Discrete element method for slope stability analysis.” *J. of Geotech. Engng.*, 118(12): 1889-1905, 1992.

[19] C.S. Chang, “Discrete element analysis for active and passive pressure distribution on retaining wall.” *Compu. and Geotech.*, 16: 291-310, 1994.

[20] A.R. Majidi, “Development of the Implicit Three Dimensional Discrete Element Method and Using in Three Dimensional Bearing Capacity Analysis of Shallow Foundations” PHD thesis, University of Tehran, May 2007.

[21] A.R. Majidi and A.A. Mirghasemi, “Iranian Journal of Science and Technology Transaction B-Engineering,32 : 107-124, 2008.

[22] “Aashto LRFD bridge design specifications”, American association of state highway and transportation officials.

[23] A.H. Bozorg Haddad, “3-D study behavior of foundations placed on the slopes by model tests” Master of Science thesis, University of Tehran.

A modified free decay test apparatus for the characterization of soft magnetic gels in the presence of magnetic fields

Venkateswara Rao. P, pvbn.rao@gmail.com
Research scholar / Dept. of Applied Mechanics / Solid Mechanics division
Indian Institute of Technology Madras
Chennai, 600 036, India

Maniprakash. S, smprakashbe@gmail.com
Postgraduate student / Dept. of Applied Mechanics / Solid Mechanics division
Indian Institute of Technology Madras
Chennai, 600 036, India

Srinivasan. S.M mssiva@iitm.ac.in
Professor / Dept. of Applied Mechanics / Solid Mechanics division
Indian Institute of Technology Madras
Chennai, 600 036, India

Abstract

This paper presents the development of a simple free decay test apparatus that can be a cost effective alternative to the popular expensive dynamical mechanical analyzers useful for characterization of the dynamic characteristics of soft magnetic composite gels in the presence of variable magnetic field. This apparatus also addresses the common difficulty faced in dynamical mechanical analyzers to conduct the characteristics of deformation dependent mechanical characteristics especially for large deformations, sometimes to the order of 100% that may be necessary for highly compliant polymeric materials. In addition, this apparatus can easily be fitted or modified to facilitate the application of magnetic field. The apparatus is designed to test thin sheet specimens of the magnetic gels in the shear mode at room temperature. As an example, magnetic composite gels prepared with micron sized polarizable particles (carbonyl iron particles) interspersed in a polymer matrix gel are used to show the effectiveness of the apparatus. The compliance of this magnetic gel can be varied under the influence of an external magnetic field. Deviations from the linear material behavior can be captured using the appropriate equations that relate the linear assumptions made. Such deviations can then be used in determining the large deformation dependent characteristics of the gel specimen. Thus, it is demonstrated that the apparatus is a cost effective and useful tool for purposes of testing soft and compliant magnetic composite gels used for damping applications.

Key words: Magneic composite gel, shear mode free decay test, storage modulus and loss factor.

1. INTRODUCTION

Magnetorheological elastomers (MREs)/ magnetic composite gels constitute a new generation of materials used in vibration control and damping devices. Apart from the passive damping properties, it is possible to control the properties of these materials under the influence of a magnetic field [1]. Primarily the storage modulus (stiffness coefficient) and the damping are the properties that are controlled in the applications. The performance of an MRE is dependent on the tunability of these properties. Based on unique characteristics of MREs, an adaptive tuned vibration absorber (ATVA) has been developed by Deng et al. [2]. Elastomeric isolator acts as a filler, amplifying or reducing the initial frequency content of the seismic motion [3]. There are also other applications of these MREs such as controllable membranes in micro-pumps [4]. In structural vibration control system applications, the transmitting force of a vibrating structure to the base through the support depends on the dynamic characteristics of the support [5]. If the dynamic characteristics of the supports are tunable then it will be possible to isolate large range of vibrations at the base of the structure. This tunability can be brought about by using magnetorheological gels in which the characteristics (typically storage moduli) is varied by applying an external magnetic field. To estimate these dynamic characteristics of a magnetic gel specimen that is deformation dependent and nonlinear, a suitable test is to be performed with the prepared magnetic gels in the presence of a magnetic field.

In the literature, various ways of performing the tests are identified to estimate the dynamic characteristics of MREs in the presence of magnetic field. Gong et al. [5], Hu et al. [6] and Wang et al. [7] have measured the mechanical properties of MREs using a custom-made system developed by them. In this system, the MRE sample sandwiched between copper slabs is subjected to shear mode forced vibration in the presence of an electromagnet with the help of an exciter, a power amplifier, a dynamic signal analyzer and piezoelectric acceleration transducers. Fuchs et al. [8] have obtained the storage and loss moduli of the MREs by the dynamic frequency scan program of the DMA instrument. Chen et al. [9] have characterized the dynamic performances of MREs by using a modified dynamic mechanical analyzer (DMA) system. The DMA system is modified by introducing a self made electromagnet which can generate a variable magnetic flux density upto 1 T. In this experiment the dynamic strain amplitude is set at 0.3% only. Zhou [10], conducted the experiment testing the damped free vibration of a system composed of a MRE and a mass in order to determine the shear storage modulus and damping factor. In this experiment the MRE is placed between the vertically arranged magnetic pole pieces in such a way that one side of the MRE is attached to the surface of lower pole and the other side is attached to the brass cover board. Here, this brass cover board acts as a mass and provides an initial displacement to the MRE when it is excited by an impulse hammer. This type of arrangement may not facilitate large deformation measurements in MRE.

Lokander and Stenberg [11] have measured the dynamic shear modulus for a double lap shear specimen using an Instron 8032 dynamic testing machine equipped with an electromagnet. The resulting electromagnet induction through the samples due to this electromagnet was 0.24T only. It was not clear regarding the possibility of more variation of magnetic induction in this test rrangement. This test was done with the small deformations (small amplitude strain range of 0.6% to 2.5%) only. Shen et al. [12] carried out the shear test on polyurethane MREs using tensile testing machine with a negligible shear deformation rate of 1 mm/min. Sun et al. [13] used DMA and MRE samples were analyzed in tensile mode at a strain of 0.5%. Abramchuk et al. [14] measured the shear modulus of the MREs using the uniaxial compression method. Popp et al. [15] investigated the MRE performances under both shear and squeeze modes. But in these tests the shear strains used is 0.1% to 10%. This set up provides the magnetic field strength of 0.15 T only when the coil current is 3A. Stepanov et al. [16] and Bose and Roder [17] studied the rheological measurements of MREs in the oscillation mode in a rheometer equipped with a magnetorheological measuring unit. In the later one, the experiments were carried out at an amplitude of 1% only.

Mostly, in the literature [2,67,9,13], it was observed that the experiments were conducted using Dynamic Mechanical Analyzer (DMA) testing machines for identifying the dynamic characteristics of MR elastomers. However, one important difficulty apart from having to introduce the magnetic field while using DMA is to be able to characterize the gel that undergoes large nonlinear deformations. The setup envisaged for use in this work would accommodate for both strong magnetic field up to 1 T when the coil current is 3A and the large nonlinear deformations. Therefore, for the characterization of dynamic characteristics of magnetic composite gels, a dynamic shear mode experiment (free decay test) is to be conducted in the presence of magnetic field.

Thus, the objective of this work, as a first step, is to prepare isotropic magnetorheological gels with different concentrations of well-dispersed micron sized magnetically polarizable particles and to develop a simple experimental setup to study and obtain the dynamic characteristics of the magnetic composite gel under varying magnetic fields in the shear mode. The uniqueness of this experimental set up is that, the experiment is performed on the gels in direct shear mode instead of indirect shear mode (either by tensile or by compressive loading) in order to obtain the shear characteristics of the gels. The dynamic characteristics are obtained in terms of storage moduli and loss factor.

The paper is arranged in three sections: methodology, results and discussion and conclusions. To show the effectiveness of the apparatus, in methodology as an example; procedures for the preparation of magnetic composite gel, description of the development of experimental set up that is designed and fabricated in conducting free decay test and data analysis performed are discussed. The static shear test is also conducted to observe the strain range above which the magnetic gel behaves as a nonlinear material. The results obtained for various compositions of the magnetic gels prepared by conducting free decay test at various magnetic field influences are discussed before making the concluding remarks.

2. METHODOLOGY

To show the effectiveness of the apparatus, a free decay test is conducted in shear mode for the determination of dynamic characteristics of soft magnetic composite gels in the presence of electromagnetic field.

There are three stages involved in finding the dynamic characteristics of soft magnetic composite gel under dynamic shear conditions. They are

1. Magnetic gel sample preparation,
2. Free decay test under varying magnetic field, and,
3. Data analysis.

And then conducted the static shear test in order to identify the shear strain above which the response is non linear.

2.1 Magnetic gel sample preparation

The magnetic gel samples are prepared using the constant ratio of polystyrene-hydrogenated polybutadiene-polystyrene triblock copolymer [18] to mineral oil gel matrix with various proportions 10%, 30%, 50%, & 70% by weight of carbonyl iron particles of size 2 to 10 μm. The detailed procedures for the preparation of this magnetorheological gel can be found in ref. [19]. The cured samples at room temperature are cut into small rectangular magnetic gel strips of 20x20x3mm to be suitable for use in mechanical characterization tests. This magnetic gel strip is then sandwiched between two non-magnetizable thin plates and adhesively bonded to them to form testable samples.

2.2 Free decay test under varying magnetic field

2.2.1 Experimental setup and test procedure

In order to facilitate large deformations with magnetic composite gel and to accommodate the magnetic field, a simple free decay test apparatus has been designed and fabricated in-house. This apparatus is used for obtaining the magnetic field dependent dynamic characteristics such as storage modulus and loss factor at room temperature and ambient conditions. The photographs of experimental set up are shown in Figure 1. The magnetic gel specimen part of the test apparatus is placed between two magnetic poles for the application of the magnetic field. The direction of the magnetic field is, thus, in the direction perpendicular to the plane of shear action when the rod oscillates.

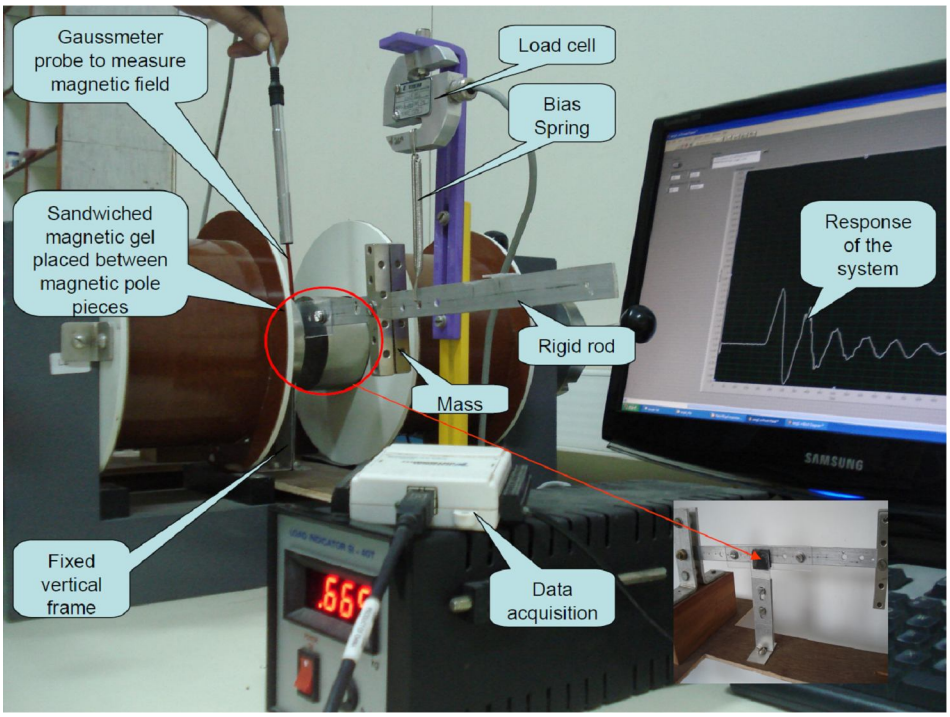

FIGURE 1: The magneto-mechanical coupled free decay testing instrument on magnetic gel under shear mode oscillation.

This instrument consists of a rigid rod with negligible mass hinged at one of its ends and hung by connecting a tensile spring at the other end. A mass is attached to the rigid rod at a known distance from the hinge. A load cell is connected to the rigid rod through a tensile spring to measure the instantaneous force exerted in the load cell. This instantaneous force is proportional to the displacement of the spring. The force exerted in the load cell is recorded through a data acquisition card as a computer data file using LabVIEW (Laboratory Virtual Instrumentation Engineering Workbench) software [20].

One plate of the magnetic gel strip specimen is fastened to the rigid rod while the other plate is fixed to the frame. The specimen gel plate which is fastened to the rigid rod can be removable from the rigid rod in order to facilitate in measuring the dynamic properties of the system in the absence of the gel. Here, the rigid rod, gel plates and the fasteners are chosen as the non magnetic materials.

The idea of this test is to determine the natural frequency and damping ratio of gels using the changes in dynamic properties of an oscillating rod in the system. In order to do this, first the dynamic characteristics of the free oscillating rod (without the magnetic gel specimen attached to the rod) should be measured so that appropriate changes can be registered and used to obtain the gel characteristics in the actual tests on the gel specimens. Therefore, as a first step in the absence of magnetic gel, initial excitation is given to the rod. Due to the presence of the spring

and the mass, the rod starts to oscillate and the response of the system is measured using a load cell. The transient response due to the initial excitation dies down due to air friction and other damping conditions.. Once this initial characteristic of the rod-mass-spring assembly is registered, then, the magnetic gel is placed appropriately in the system that allows a shear mode vibration of the gel sample. Once again, the system is excited and a fresh response measurement is made on the system. The above test procedure is repeated under various magnetic fields in the range of 0 to 0.7 T for different gels prepared.

2.2.2 *Data analysis*

The dynamic response of the system for the given initial excitation depends primarily on the three dynamic attributes of the system – the stiffness of spring elements, the dissipation due to internal friction of the system and the inertia due to mass. If the gel sample is also attached, the stiffness and the damping associated with the gel specimen also affect the dynamic characteristics. The testing system is assumed to be linear. Tests on the system dynamic characteristics were conducted to validate this assumption.

With the mass of the system known, a simple straightforward procedure is adopted to estimate the other two attributes of the system, namely, the storage part (stiffness of the spring) and the dissipation part (damping coefficient). Using a free decay test (by introducing a small initial disturbance / excitation to the system), these attributes are then calculated from the measured response data obtained from the load cell. The procedure and the principle used to calculate the above mentioned system attributes are discussed below.

The equation of motion for the system in the absence of the gel specimen can be written using the moment equilibrium about the hinge as,

$$m l_m^{\,2}\ddot{\theta} + c_s l_s^{\,2}\dot{\theta} + k_s l_s^{\,2}\theta = 0 \tag{1}$$

where m is the mass and, l_m and l_s are the distances from hinge support to the mass and the spring respectively. c_s and k_s are chosen such that the response of mathematical model matches closely with the obtained response. Typically, the damping frequency of the system, ω_d in Hz and the damping ratio, ε_d, are used in the response calculations to match with the experimentally obtained response and then the stiffness, k_s, and the damping coefficient, c_s, of the system are calculated by using the following expressions and these are assumed to be constants irrespective of whether the magnetic gel is mounted or not.

$$k_s = 4\pi^2 m \frac{l_m^{\,2}}{l_s^{\,2}} \frac{\omega_d^{\,2}}{1-\varepsilon_d^{\,2}} \tag{2}$$

$$c_s = 4\pi m \frac{l_m^{\,2}}{l_s^{\,2}} \frac{\omega_d \varepsilon_d}{\sqrt{1-\varepsilon_d^{\,2}}} \tag{3}$$

Figure 3 shows the schematic of the vibrating test system with the gel. The gel is represented using a spring and dashpot in parallel attached to the horizontal bar of the system. With the gel mounted to the system, the equation of motion of the system can be written using moment about the hinge in the Fig. 3 as,

$$m l_m^{\,2}\ddot{\theta} + (c_s l_s^{\,2} + cg\, l_g^{\,2})\dot{\theta} + (k_s l_s^{\,2} + k_g\, l_g^{\,2})\theta = 0 \tag{4}$$

where l_g is the distance of the center of the mounted gel from the hinge support as shown in Fig.3. Thus, the stiffness and the damping coefficient (k_g, c_g) of the gel can be calculated with the known values of c_s and k_s obtained earlier by using the following expressions [21]..

$$k_g = \frac{4\pi^2 m l_m^{\,2} \omega_d^{\,2}}{(1-\varepsilon_d^{\,2}) l_g^{\,2}} - \frac{K_s l_s^{\,2}}{l_g^{\,2}} \tag{5}$$

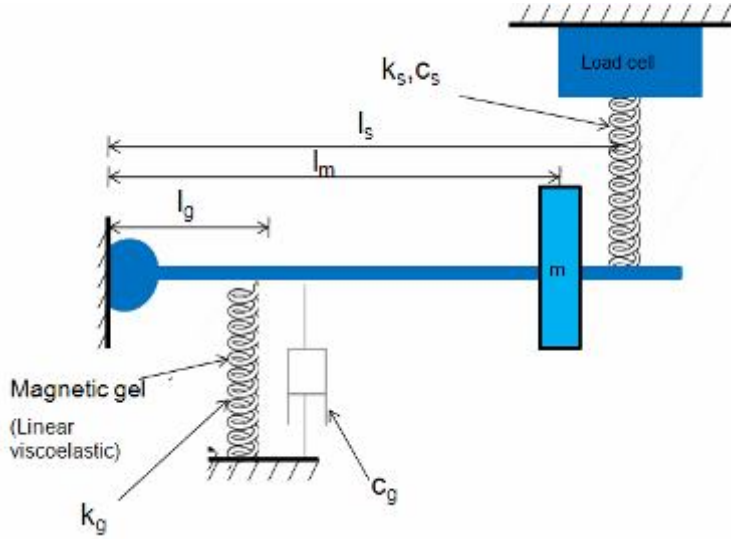

FIGURE 3: A schematic diagram of the testing system with the magnetic gel mounted. The magnetic gel is assumed to be of linear viscoelastic nature.

$$c_g = \frac{4\pi m l_m^{\,2} \omega_d \varepsilon_d}{\left(\sqrt{1-\varepsilon_d^{\,2}}\right) l_g^{\,2}} - \frac{c_s l_s^{\,2}}{l_g^{\,2}} \tag{6}$$

The solution of the equation of motion in equations (1) and (4) is in the following form:

$$\theta = \Theta e^{-\varepsilon_d \omega_n t} \sin(\sqrt{1-\varepsilon_d^{\,2}}\,\omega_n t) \tag{7}$$

Where Θ is initial amplitude and θ is amplitude with time t.
These dynamic properties are used to calculate the storage modulus, *G'*, the loss modulus, *G"* and the loss factor, η , of the gel using following equations.

$$G' = \frac{k_g t}{lb}; \tag{8}$$

$$G'' = \frac{c_g t \omega_d}{lb}; \quad \text{and} \tag{9}$$

$$\eta = \frac{G''}{G'} \tag{10}$$

where, *t* is the thickness of the gel strip, *l* is the length of the gel strip, and *b* is the breath of the gel strip.

2.3 Static shear test

The static shear test is performed in order to identify the shear strain above which the response is non linear. The same basic experimental set up used for free decay test is used even for static shear test with some modifications. This setup consists of a rigid rod (the same rod, which is considered for dynamic shear test) with negligible mass hinged at one of its ends and the rod is hung by connecting a tensile spring at the other end. Then, an LVDT probe for displacement measurement is placed at a known distance at which bar will balance in straight horizontal position. A load cell is connected to the rigid rod through a spring to measure the balancing force caused in the load cell. At this moment, the initial reading (at zero displacement) measured using LVDT.

Now, the gel plate is connected to the rigid rod while the spring attachment is removed from the rod. The displacement at this configuration is noted down. The difference in the above two readings gives the displacement at zero load. Knowing the displacement at the LVDT probe, the displacement at the gel and hence the shear strain can be calculated. At this zero load position, the force in the gel can be calculated by using force equilibrium conditions. The force vs. deflection of the gel specimen is used to find the shear stress to shear strain variation in the gel specimen.

3. RESULTS AND DISCUSSION

In this section, on the basis of system dynamic response and the gel specimen dynamic response, results obtained for one of the various compositions of the magnetic gels prepared by the earlier mentioned procedures using free decay test under varying magnetic field are discussed.

3.1 Free decay test-Determination of test system dynamic characteristics with out gel.

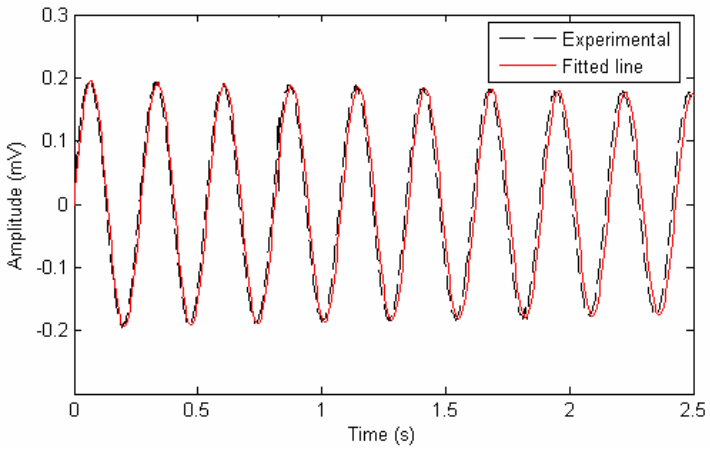

(a)

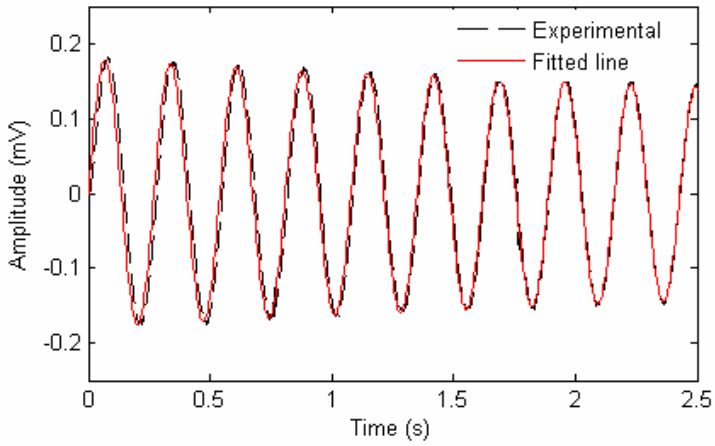

(b)

FIGURE 4: The response of the system measured using load cell in the absence of the gel. (a) without magnetic field, (b) With a magnetic field of 0.7T.

Figures 4(a) & (b) show the response of the system measured using load cell in the absence of the gel with and without magnetic field respectively. The voltage output is measured which is proportional to the displacement of the system. In these figures, dashed line shows the fitted experimental data obtained using load cell and the curve with solid line shows the matching response from the solution (eq.(7)) of the mathematical model obtained from the equation of motion upon choosing appropriate amplitude, frequency and the damping ratio.

The frequency and the damping ratio of the response are obtained to be the same for the system with and without magnetic field (ω_d = 3.722 Hz, damping ratio, ε_d = 0.024). Using these identified damped oscillation frequency and the damping ratio, the stiffness and damping coefficients of the system are found to be . c_s= 0.3446 Nm/s and k_s=167.9181 N/m. It is observed that there is no change in the response of the system due to the applied magnetic field. Here a linear spring response can be proved as a linear material from the exact curve fitting of the solution obtained from the linear equation to the experimental response

3.2 Free decay test response –with magnetic gel

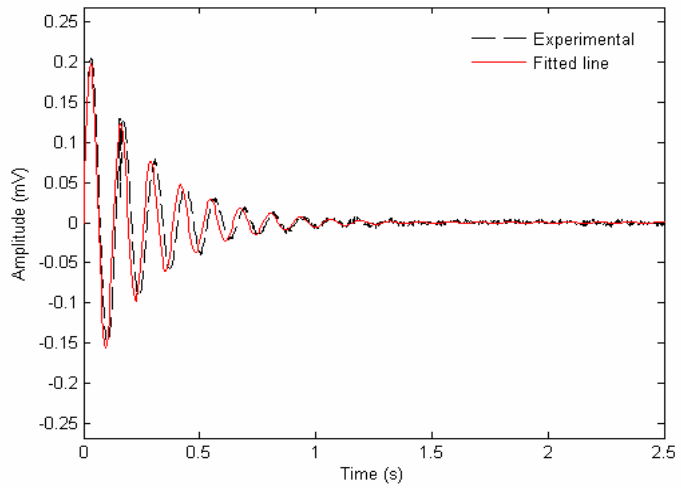

(a)

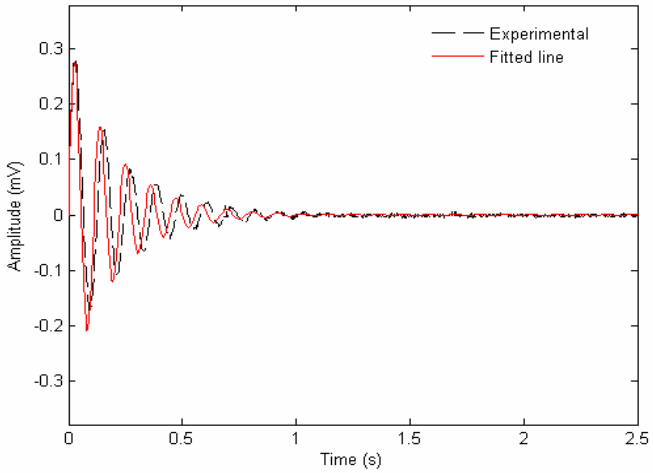

(b)

FIGURE 5: The response of the system measured using load cell in the presence of the gel with 50% by weight of carbonyl iron particles (a)without magnetic field, (b) with 0.7 T magnetic field. It can be seen that the oscillations die down fast in the presence of magnetic gel.

With the test system characteristics determined, the gel is mounted on the test system and the free decay vibration test is conducted with varying magnetic field. Depending on the initial excitation given, though small, shear strains up to 50% could be realized in the gels. From the response of the test system with the gel mounted, the damping frequency and the damping ratio are first determined under 0 to 0.7 T of magnetic field. The stiffness and damping coefficient (k_g, c_g) of the gel are then calculated using equations (5) and (6) respectively.

The response of the test system with the gel mounted (dashed lines) under 0 and 0.7T magnetic field and the matching responses (solid line) from the solution (eq.(7)) of the mathematical model obtained from the equation of motion are presented in Figures 5 (a) & (b) respectively. Here the shear strain experiences about 33%. On keen observation, one can identify that the curve obtained through mathematical model on the basis of equation of motion is exactly fitting with the experimental response at both extreme ends of the decayed curves. But, in the middle of the curves, a shift is observed. This could be due to the non linear nature of the gel. This nonlinearity due to large deformations can be observed from the following static shear test results also.

3.3 Static shear test: stress-strain behavior of gel due to large deformations

As shown in Figures 6, whenever the deformation is reaches about 30% of it's thickness, the stress-strain behavior is started showing non linear in nature.

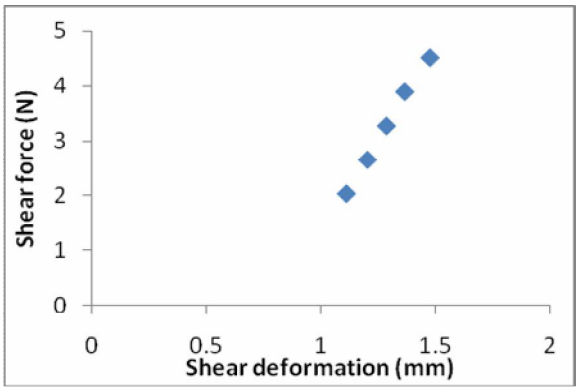

FIGURE 6: Static shear force vs shear deformation of magnetic composite gel with 50% by wt. of carbonyl iron particles at 0.7 T magnetic field.

3.4 Determination of dynamic characteristics of the magnetic gel

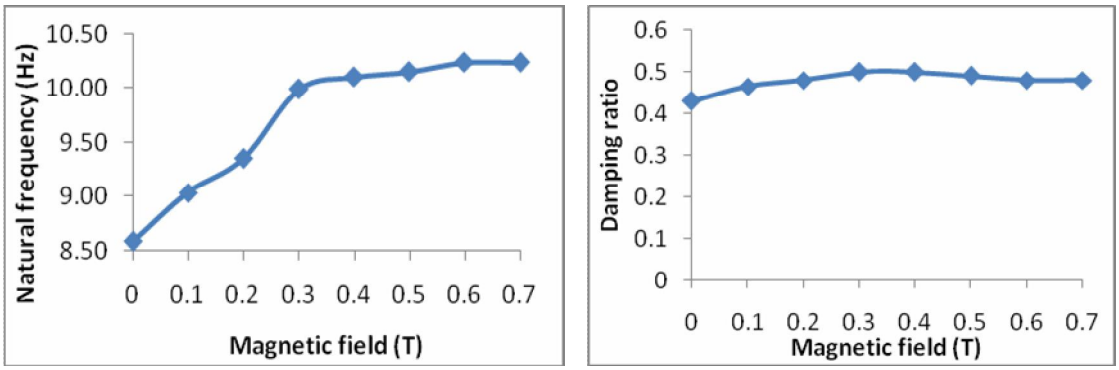

(a) (b)

FIGURE 7: The response of the system measured in terms of (a) *natural frequency and (b) damping ratio* with a gel (consists of 50% by weight of carbonyl iorn particles) mounted under varying magnetic field.

The total system characteristics in terms of the natural frequency and the damping ratio are first determined from the response curves. The natural frequency with respect to the applied magnetic field is presented in Fig. 7(a). One can also observe that there is a significant change in the natural frequency in the range of 0.1 T to 0.4 T in the gels so that the properties of the gel can be significantly controlled in this range of the magnetic field. There are no observable changes seen in the damping ratio for varying magnetic fields (see Fig.7(b)). This is an important observation in the context of application of the magnetic gel to damping applications.

The shear storage modulus and loss modulus are calculated appropriately using equations (8) and (9) for various magnetic field values. The shear storage modulus, from Fig. 8(a), about 52% change is observed over 0.6 T of applied magnetic field in the gel prepared with 50% by weight of carbonyl iron particles. In other words, a change in storage modulus of 41.387 kPa to 65.835 kPa can be achieved with 0.7 T of magnetic field. This capability is required for vibration control applications. Here, three tests were run at every magnetic field. From those three tests, the deviation in the results obtained in storage modulus and loss factor are less than 4%. Due to this very less deviation, the average of the three tests results were presented in the Figs.8(a) and (b). As can be seen in Fig.8(b), loss factor obtained from equation (10) does not change significantly, indicating that the change in damping is marginal.

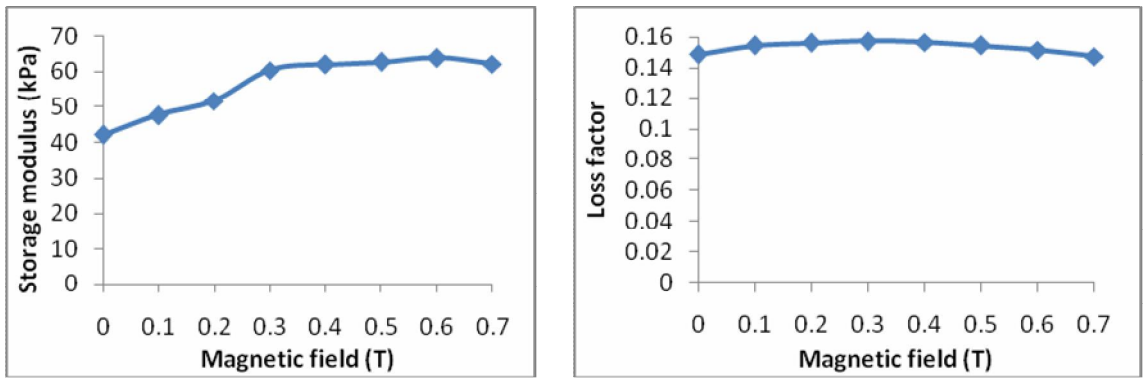

(a) (b)

FIGURE 8: (a) Storage modulus, and (b) loss factor of the gel with 50& by weight of carbonyl iron particles under different magnitudes of magnetic field.

It is shown in this work that the improvement in storage modulus due to magnetic field of as high as 59% is achievable with isotropic soft MR gels. This is significantly higher than reported in literature [5, 6, 13] (nearly 30% or less improvement in the storage modulus). The authors believe that this increase could be due to the soft elastomeric matrix used in this work.

4. CONCLUSIONS

Since, dynamical mechanical analysis tests are difficult to conduct in the presence of large deformations (of the order of 50%) and strong magnetic fields, a simple, cost effective free decay test apparatus is designed, fabricated and used to conduct the magnetic field dependent shear response tests on soft magnetic gels under dynamic conditions at room temperature.

It is shown in this paper, that the dynamic response of the gel can be obtained. The dynamic characteristics of the gel can be calculated from this response using a linear model for the gel.

The apparatus also provides for the possibility of obtaining deviations from the linear behavior that, if modeled appropriately, can fetch the nonlinear characteristics of the gel due to large deformations. The deviation from linearity is also confirmed from the static tests conducted.

For a future work, the authors are planning to incorporate the above deviation in behavior as a measurement for nonlinear response. In the experimental procedures, while giving a free excitation to the rigid rod, sometimes the rigid rod may be subjected to minor lateral oscillations. This may leads to small error in the response of the system. In future, the authors are also trying to improve the experimental setup in order to avoid this minor lateral oscillations of the rigid rod .

5. REFERENCES

1. Carlson, J. D. and M. R. Jolly (2000). MR fluid, foam and elastomer devices. *Mechatronics,* 10, 555-569.

2. Deng, H. X. and X. L. Gong (2008). Application of magnetorheological elastomer to vibration absorber. Communication in nonlinear science and numerical simulation, 13,1938-1947.

3. Ibrahim,R.A. (2008). Recent advances in nonlinear passive vibration isolators. *Journal of sound and vibration*, 314, 371-452.

4. Beskok, A., and Srinivasa, A. R.,"Simulation and analysis of a magnetoelastically driven micro-pump", J. Fluid Eng-T, ASME, 123 (2): 435-438, 2001.

5. Gong, X. L., X. Z. Zhang, and P. Q. Zhang (2005). Fabrication and characterization of isotropic magnetorheological elasomers. *Polymer testing* 24, 669-676.

6. Hu, Y., Y. L. Wang, X. L. Gong, X. Q. Gong, X. Z. Zhang, W. Q. Jiang, P. Q. Zhang and Z. Y. Chen (2005). New magnetorheological elastomers based on polyurethane/Si- rubber hybrid. *Polymer testing*, 24, 324-329.

7. Yinling wang, Yuan Hu, Xinglong Gong, Wanquan Jiang, Peiqiang Zhang, Zuyao Chen (2007). Preparation and properties of magnetorheological elastomers based on silicon rubber/polystyrene blend matrix. Journal of applied polymer science, Vol.103, 3143-3149.

8. Fuchs, A, Q. zhang, J. Elkins, F. Gordaninejad and C.Evrensel (2007). Development and characterization of magnetorheological elastomers. J. Applied polymer science, vol.105,2497-2508.

9. Chen, L, X. L Gong, W. Q. Jiang, J. J. Yao, H. X. Deng and W. H. Li (2007). Investigation on magnetorheological elastomers based on natural rubber. *J. mater.sci.,*.42, 483-5489.

10. G. Y. Zhou . (2003). Shear properties of a magnetorheological elastomer. Smart materials and structures, 12, 139-146.

11. Lokander. M and B. Stenberg (2003). Performance of isotropic magnetorheological rubber materials. Polymer testing, 22, 245-251.

12. Shen.Y, M.F. Golnaraghi and G.R. Heppler (2004). Experimental research and modeling of magnetorheological elastomers. Journal of intelligent material systems and structures, 15, 27-35.

13. Sun.T. L., Gong, X. L., Jiang. W. Q., Li.J.F., Xu. Z. B., and Li. W. H. (2008). Study on the damping properties of magnetotheological elastomers based on cis-polybutadiebe rubber. *Polymer testing,* 27, 520-526.

14. Abramchuk S S, D.A. Grishin, E.Yu. Kramarenko, G.V. Stepanov and A.R. Khokhlov (2006). Effect of Homogeneous magnetic field on the mechanical behavior of soft magnetic elastomers under compression. Polymer science, 48, 138-145.

15. Popp. K.M, X.Z. Zhang, W.H Li and P.B. Kosasih (2009). MRE properties under shear and squeeze modes and applications. Journal of physics: Conference series 149, 012095, 1-4.

16. Stepanov, G. V., S. S. Abramchuk, D. A. Grishin, L. V. Nikitin, E. Yu. Kramarenko and A.R.Khokhlov (2007). Effect of a homogeneous Magnetic field on the viscoelastic behavior of magnetic elastomers*. Polymer,* 48 (2007) 488-495.

17. H. Bose and R. Roder (2009). Magnetorheological elastomers with high variability of their mechanical properties. Journal of physics: Conference series 149, 012090, 1-6.

18. Terry V.Pearce. (2006). “Jelly Blocks and Jelly Letters”, U.S. Patent. 7,101,247 B2.

19. J. Venkataraghavan, Compliant mechanisms, Master’s thesis, Mechanical Engineering, Texas A&M University, College Station, Texas, 2001.

20. J.Travis and J. Kring.(2006). LabVIEW for Everyone: Graphical programming made easy and fun ed.3. Prentice Hall.

21. Thomson W.T and Dahleh M.D. (2003). Theory of vibration with applications, fifth edition, Pearson Education Pvt. Ltd. ,Singapore.

Modeling of moisture diffusion and heat transfer during softening in wood densification

Donghua Jia jiadonghua@hotmail.com
Former Graduate Student
Faculty of Forestry and Environmental Management,
University of New Brunswick, P.O.Box 4400,
Fredericton, NB, E3B 5A3 Canada

Muhammad T. Afzal mafzal@unb.ca
Associate Professor
Department of Mechanical Engineering
University of New Brunswick, P.O.Box 4400,
Fredericton, NB, E3B 5A3 Canada

Meng Gong mgong@unb.ca
Research Scientist
Faculty of Forestry and Environmental Management,
University of New Brunswick, P.O.Box 4400,
Fredericton, NB, E3B 5A3 Canada

Alemayehu H. Bedane alemhailu2003@yahoo.com
Graduate Student
Faculty of Forestry and Environmental Management,
University of New Brunswick, P.O.Box 4400,
Fredericton, NB, E3B 5A3 Canada

Abstract

Mechanical densification of wood involves compressing the wood in radial direction using heat, water and steam to produce a higher density surface exhibiting better mechanical properties. The densified wood is an environmentally friendly product that presents new opportunities for the wood products industry. Wood surface densification involves both soaking and heating. The objective of this study is to present a two-dimensional model of moisture diffusion and heat transfer during softening process in order to understand and control the degree of surface densification. The governing equations for diffusion process and heat transfer are solved numerically at non-steady state conditions. Experimental data was also collected on Aspen and Balsam fir specimens to determine the moisture profile. The model predicts suitably the moisture content and temperature in the soaking process. The results showed that the surface to be softened could be heated to a temperature of 80~90 ^{o}C in 3~5 minutes with an average moisture content of 25 percent in the surface layer.

Keywords: Softening, soaking, densification, moisture diffusion, heat transfer, modeling

1. INTRODUCTION

With the importance of wood in man's environment, the demand for hardwood used for furniture and interior materials keeps increasing. In Canada, coniferous woods account for about 80% of the total volume of merchantable timber. Compared with hardwoods, coniferous softwoods show low density and are generally soft. Therefore, to utilize softwoods for interior materials, it is necessary to improve their surface properties such as abrasion resistance and hardness as well as their dimension stability. Inoue *et al.* (1990) studied the improvement of surface properties of lumber by surface compression [1]. In comparison with untreated wood, abrasion resistance and hardness increased by 40 to 50% and 120 to 150%, respectively. Softening is an important step in the manufacture of surface-densified wood. Softening process involves soaking and heating of wood. It is vital to study and determine the distribution of moisture content and temperature across the thickness of a wood board in order to understand and control the degree of surface densification. This study was aimed at understanding the moisture diffusion and heat transfer in the coniferous wood boards during softening process, and eventually proper softening parameters can be determined and optimized.

2. MATHEMATICAL MODEL

2.1 Governing equations

At low temperature, moisture in wood mainly moves by a diffusion process that is driven by a gradient in the moisture content. Fick's second law offers one generalized method to describe the diffusion process [2, 3]. This approach allows the estimation of moisture gradients at any time during heating period. In the literature, the thermally induced mass transfer, which contributed considerably to the total moisture flux, was also taken into account in the model construction [4]. Moisture transfer should be considered a coupled process with heat transfer, or described by a non-isothermal diffusion model.

Non-isothermal diffusion was analyzed by different methods. Siau (1995) indicated that the thermodynamic model provided the best fit to the experimental data [5]. The model derived from non-equilibrium thermodynamics was presented by Nelson (1991) [6], and the steady state mass flux was shown as,

$$J_m = -k_m\left(\frac{dM}{dT}\frac{dT}{dx}+\frac{dM}{dx}\right) \tag{1}$$

The temperature gradient coefficient was given as,

$$\frac{dM}{dT} = \frac{H}{RT}\frac{\partial M}{\partial H}\frac{E_b}{T} \tag{2}$$

Where

$$k_m = G_m D\,, \tag{3}$$

$$E_b = 38{,}500 - 290M \tag{4}$$

Taking Eq. 1 as the starting point, the differentiated unsteady-state equation was derived as,

$$\frac{\partial M}{\partial t} = \nabla \cdot \left(D_{eff,T} \nabla T + D_{eff,M} \nabla M \right) \tag{5}$$

As a complete model for moisture movement, the energy balance equation is also required in addition to Eq. 5. Heat transport in wood occurs via heat conduction in all the three phases (free water, bound water, and vapor), and by convection through mass transportation. In the slow heating condition the vapor and free liquid bulk flows can be ignored, and the term of heat transfer by convection can also be omitted. With the simplification of conventional heat transfer, the heat balance equation was derived as,

$$\frac{\partial \left(\rho_{wood} c_{pwood} T \right)}{\partial t} = \nabla \left(\lambda_{eff} \nabla T \right) \tag{6}$$

In this study, the soaking process makes a two dimensional model necessary. In the experiments, the water was sucked into wood mainly in the thickness direction. However, the wood specimen was heated in two scenarios: heat transfer along specimen thickness from the boiling water, and heat transfer along specimen width from surrounding hot evaporated vapor. Thus, the cross section (i.e. width and thickness) of a specimen was taken into consideration in the model study.

Boundary conditions

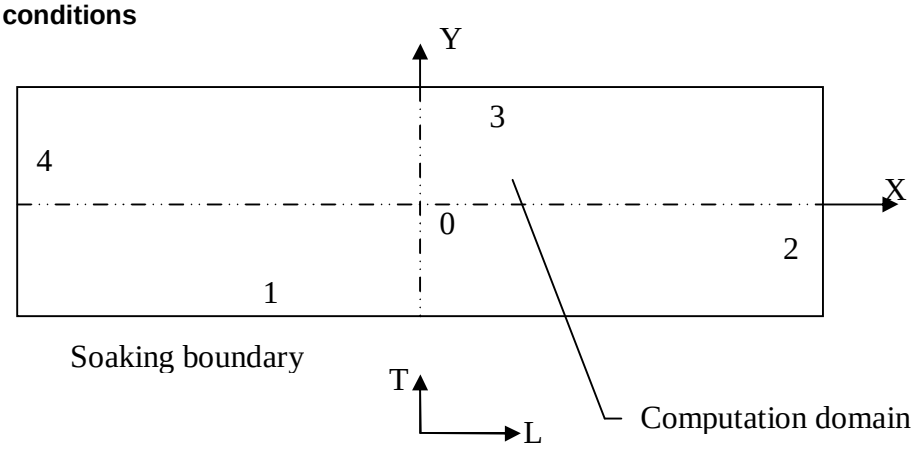

FIGURE.1. Configuration of 2-D model computation domain

In Figure 1, there were three types of boundary conditions. Boundary 1 was emerged into the water; boundaries 2 and 4 were heated by hot evaporated vapor; boundary 3 was exposed to open air. Using the relation between surface emission coefficient (*S*) and moisture transfer on the surface, the external surface, boundaries 2, 3, and 4 can be expressed as,

$$D \frac{\partial M}{\partial x} = -S \left(M - M_{\infty} \right) \tag{7}$$

The boundary condition for heat exchange could be written as,

$$\lambda_{eff}\ \frac{\partial T}{\partial x} = -h_{heat}\left(T - T_{\infty}\right), \text{ at the external surface} \tag{8}$$

At the boundary 1 (in water), the condition is imposed as:

$$M = M_{\max} \tag{9}$$
$$T=100\ ^{o}\text{C}, \tag{10}$$

2.2 Numerical procedures

The non-isothermal model equations are solved numerically. The finite element method is used to discretize the mass diffusion and heat transfer equations. The weak form of Eq. 5 and Eq. 6 is expressed as,

$$\int_V \begin{bmatrix} N_i & 0 \\ 0 & N_i \end{bmatrix} \frac{\partial}{\partial t} \begin{bmatrix} M \\ \rho Cpwood T \end{bmatrix} = \int_V \begin{bmatrix} N_i & 0 \\ 0 & N_i \end{bmatrix} \frac{\partial}{\partial x} \begin{pmatrix} D_{Mx}\frac{\partial M}{\partial x} + D_{Tx}\frac{\partial T}{\partial x} \\ k_x \frac{\partial T}{\partial x} \end{pmatrix} + \int_V \begin{bmatrix} N_i & 0 \\ 0 & N_i \end{bmatrix} \frac{\partial}{\partial y} \begin{pmatrix} D_{My}\frac{\partial M}{\partial y} + D_{Ty}\frac{\partial T}{\partial y} \\ k_y \frac{\partial T}{\partial y} \end{pmatrix} \tag{11}$$

Following the procedure of integration by parts, Eq. 12 can be obtained:

$$\int_V \begin{bmatrix} N_i & 0 \\ 0 & N_i \end{bmatrix} \frac{\partial}{\partial t} \begin{bmatrix} M \\ \rho Cpwood \end{bmatrix} \begin{matrix} \\ T \end{matrix} = \int_S \begin{bmatrix} N_i & 0 \\ 0 & N_i \end{bmatrix} \begin{pmatrix} D_{Mx}\frac{\partial M}{\partial x} + D_{Tx}\frac{\partial T}{\partial x} \\ k_x \frac{\partial T}{\partial x} \end{pmatrix} dS -$$
$$\int_V \frac{\partial}{\partial x} \begin{bmatrix} N_i & 0 \\ 0 & N_i \end{bmatrix} \cdot \begin{pmatrix} D_{Mx}\frac{\partial M}{\partial x} + D_{Tx}\frac{\partial T}{\partial x} \\ k_x \frac{\partial T}{\partial x} \end{pmatrix} dx - \int_V \frac{\partial}{\partial y} \begin{bmatrix} N_i & 0 \\ 0 & N_i \end{bmatrix} \cdot \begin{pmatrix} D_{My}\frac{\partial M}{\partial y} + D_{Ty}\frac{\partial T}{\partial y} \\ k_y \frac{\partial T}{\partial y} \end{pmatrix} dy \tag{12}$$

where N_i is the weighting function.

The finite element approximation can be derived by considering

$$M(x,y) = [N]\{M\} \tag{13}$$
$$T(x,y) = [N]\{T\} \tag{14}$$

where *M, T* represents the nodal point values with respect to time. Substitution of these finite element approximations into the weak form gives,

$$\sum \int_{Ve} [C]dV\ \frac{\partial}{\partial t}\begin{Bmatrix} M_e \\ T_e \end{Bmatrix} + \sum \int_{Ve} [S]dV \begin{Bmatrix} M_e \\ T_e \end{Bmatrix} = \sum \int_{Se} [B]dS \tag{15}$$

$$\text{where} \quad [C] = [N]\rho c_p [N] \tag{16}$$

$$[S] = [N'] D_{eff} [N'] \tag{17}$$

Eq. 18 can be obtained, in terms of central time difference,

$$\left(\frac{1}{2}[S] + \frac{1}{\Delta t}[C_t]\right)\begin{Bmatrix} M_e \\ T_e \end{Bmatrix}^{n+1} = [B]^{n+\frac{1}{2}} + \left(\frac{1}{\Delta t}[C_t] - \frac{1}{2}[S]\right)\begin{Bmatrix} M_e \\ T_e \end{Bmatrix}^{n} \tag{18}$$

A computer code was developed to solve above algebraic equations.

3. EXPERIMENTAL

Aspen (*Populus tremuloides* Michx.) and Balsam fir (*Abies balsamea* (L.) Mill.) specimens were used for moisture distribution tests. The dimension of each specimen was 280 mm long, 25 mm thick and 37 mm wide. All specimens were stored in a conditioning chamber set at 20^{o}C and 65% relative humidity prior to the tests. In the soaking process, the water was heated to the boiling point, and then a specimen was put on the top of a shelf in the water with 1mm of the specimen in the radial direction (thickness) being emerged into the water. The whole soaking process took approximately 5 minutes. After soaking, the specimen was cut into several small slides along the thickness to determine the moisture profiles.

4. RESULTS AND DISCUSSION

4.1 Model validation

During softening in wood densification, it is important to know how the heat and moisture transfer distributed within the surface of the wood. This information can be used to adjust the treatment for densification parameters, and to control the quality of final product more effectively. The proposed model predicted the moisture and temperature profile very well. The test results are shown in Figures 2 and 3 for aspen and balsam fir, respectively. The soaking depth of a specimen shown in the figures is approximately 8 mm for both species. The average moisture content distribution along the thickness for aspen after soaking process was increased non-uniformly from unsoaked surface. In case of balsam fir the average moisture content distribution along the thickness was increased uniformly from unsoaked surface.

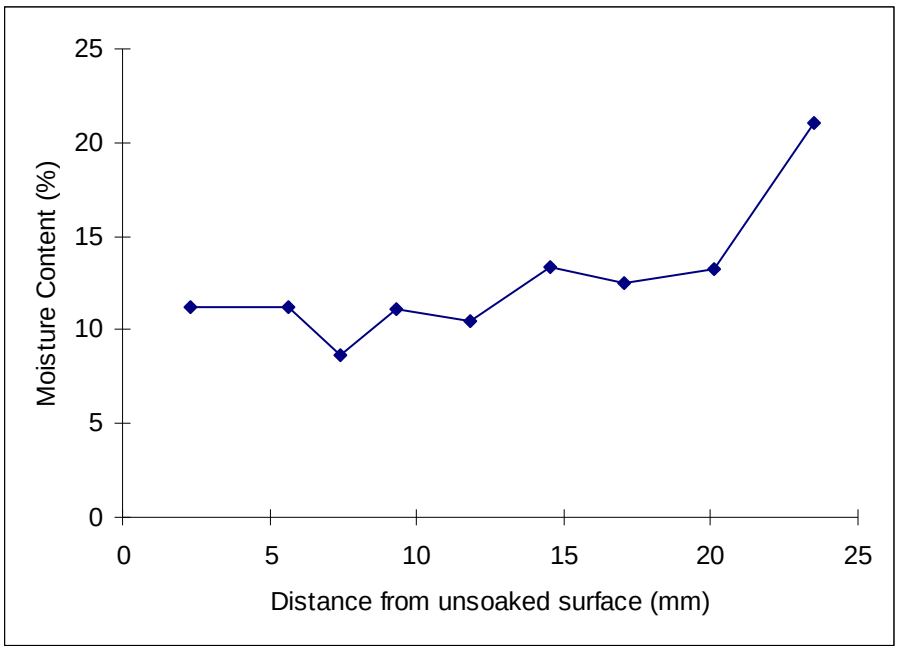

FIGURE.2. Distribution of average moisture content along thickness for three aspen specimens after soaking process

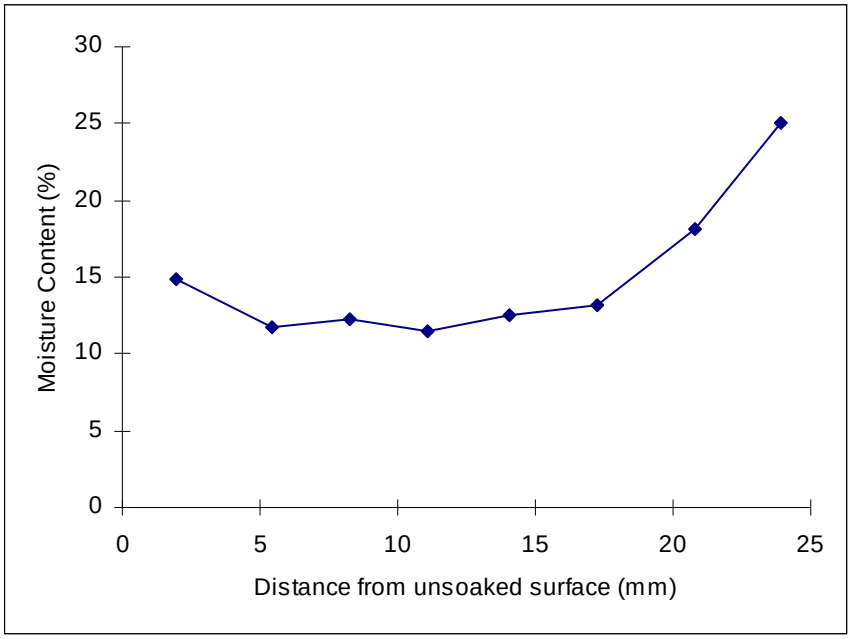

FIGURE. 3. Distribution of average moisture content along thickness for three balsam fir specimens after soaking process

Experimental results of the moisture profile of wood in the soaking process compared to verify the model calculation. To simulate the soaking process by model calculation, the following diffusion coefficient was used in the model for wood [4],

$$D_{eff,M} = 4.78\times10^{-5}\exp\left(-3574/T\right) \tag{19}$$

Thermal conductivity of wood with moisture content was approximated by the following empirical equation [7]:

$$k = G(0.2+0.004M)+0.024 \tag{20}$$

Where *G* is the specific gravity based on volume at moisture content *M*.
The heat capacity of wet wood is a function of both moisture content and temperature. Koumoutsakos (2001) showed that the heat capacity was not related to wood species and density, and was assumed to be constant over the temperature range of interest [7],

$$Cp_{wood} = \left(1176+5859M\right)/\left(1+M\right) \tag{21}$$

The results of model simulation and corresponding experimental data are shown in Fig. 4 and 5. Both figures show a very good model prediction of temperature and moisture distribution. Fig. 4 illustrates that the temperature gradient along the thickness is minimal; this can be explained by the effect of hot evaporated vapor surrounding the wood. In Fig. 5, the thickness wetted by soaking in model calculation is also approximately 8 mm.

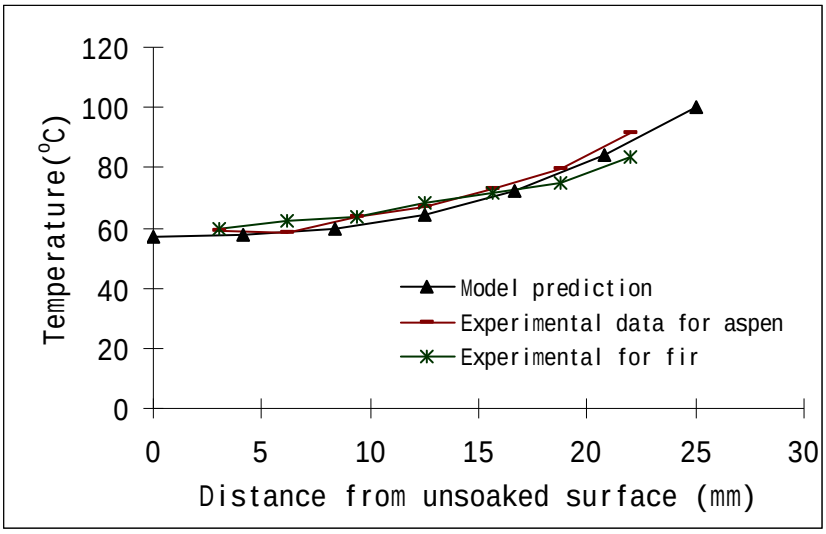

FIGURE. 4. Predicted temperature distribution by model calculation

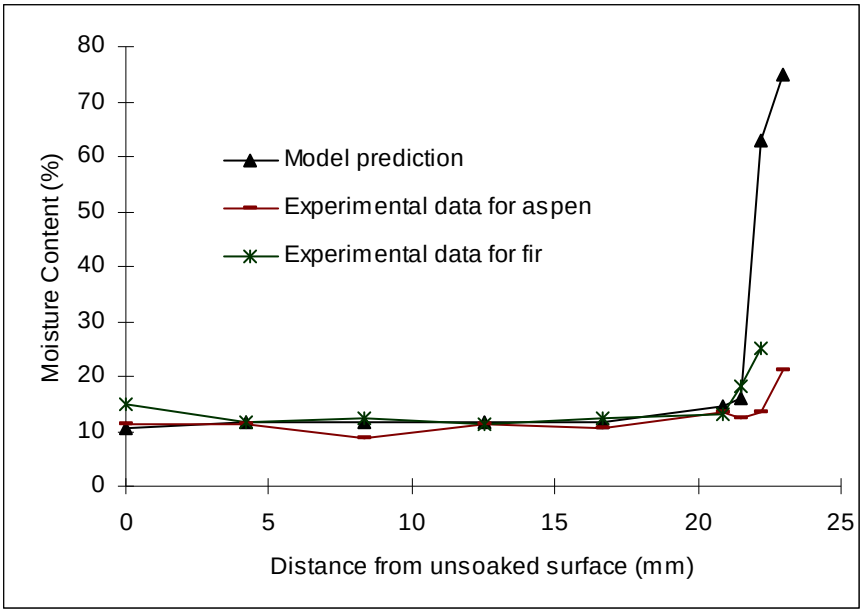

FIGURE. 5. Predicted moisture distribution by model calculation

5. CONCLUSIONS

From the above analysis and comparison between model prediction and experimental data, it can be concluded that:

(1) The principal mechanism of moisture movement in the soaking process is the diffusion of moisture caused by moisture and temperature gradients, also the numerical model for moisture and heat transfer can be suitably used to predict the variables of moisture content (*M*) and temperature (*T*) in the soaking process.

(2) The boundary conditions selected can accurately describe the moisture and heat transfer processes through the material surfaces.

(3) The average moisture content in the surface layers was approximately 25%.

(4) The surface of a specimen to be softened could be heated to a temperature of 80°C to 90°C in 3-5 minutes for these two species. The temperature of the opposite face layers was approximately 60°C.

6. NOMENCLATURES

C_p	heat capacity, $J / Kg.K$
D_{eff}	effective diffusion coefficient, m^2/s
E_b	activation energy, $J/\ mol$
G	specific gravity
h_{heat}	heat transfer coefficient, $W / m^2.K$
ΔH	latent heat, J / kg
H	relative humidity
J	fluxes of moisture, $kg/m^2.s$
J_e	fluxes of enthalpy, W/m^2
k	thermal conductivity
k_m	heat transfer coefficient, m / s
M	moisture content
R	gas constant, $J/mol.K$
S	surface emission coefficient, m/s
T	temperature
ρ	density of liquid, kg/m^3
λ_{eff}	thermal conductivity, W/m.K

7. ACKNOWLEDGMENT

The authors would like to acknowledge Natural Resources Canada for its support and funding under its Value to Wood Program.

8. REFERENCES

[1] M. Inoue, M. Norimoto, Y. Otsuka, and T. Yamada. 1990. Surface compression of coniferous wood lumber. 1: A new technique to compress the surface layer. Mokuzai Gakkaishi 36(11): 969-975.

[2] W.T. Simpson and J. Y. Liu. 1991. Dependence of the Water Vapor Diffusion Coefficient of Aspen on Moisture Content, Wood Sci. Tech. 26: 9-21.

[3] W.T. Simpson, 1993. Determination and Use of Moisture Diffusion Coefficient to Characterize Drying of Northern Red Oak, Wood Sci. Tech. 27: 409-420.

[4] S. Avramidis, P. Englezos, and T. Papsthansiou. 1992. Dynamic nonisothermal transport in hygroscopic porous media, Moisture diffusion in wood, AIChE J. 38(8): 1279-1287.

[5] J.F. Siau, 1995. Wood: Influence of Moisture on Physical Properties, Virginia Tech., USA.

[6] R.M. Nelson, Jr. 1991. Heats of Transfer and Activation Energy for Bound-water Diffusion in Wood, Wood Sci. Tech. 25: 193-202.

[7] A. Koumoutsakos, S. Avramidis, and S. G. Hatzikiriakos. 2001. Radio Frequency Vacuum Drying of Wood. I. Mathematical Model, Drying Technology 19(1): 65-84.

CALL FOR PAPERS

International Journal of Engineering (IJE) is devoted in assimilating publications that document development and research results within the broad spectrum of subfields in the engineering sciences. The journal intends to disseminate knowledge in the various disciplines of the engineering field from theoretical, practical and analytical research to physical implications and theoretical or quantitative discussion intended for both academic and industrial progress.

Our intended audiences comprises of scientists, researchers, mathematicians, practicing engineers, among others working in Engineering and welcome them to exchange and share their expertise in their particular disciplines. We also encourage articles, interdisciplinary in nature. The realm of **International Journal of Engineering (IJE)** extends, but not limited, to the following:

- Aerospace Engineering
- Agricultural Engineering
- Biomedical Engineering
- Chemical Engineering
- Civil & Structural Engineering
- Computer Engineering
- Control Systems Engineering
- Education Engineering
- Electrical Engineering
- Electronic Engineering
- Engineering Mathematics
- Engineering Science
- Environmental Engineering
- Fluid Engineering
- Geotechnical Engineering
- Industrial Engineering
- Manufacturing Engineering
- Materials & Technology Engineering
- Mechanical Engineering
- Mineral & Mining Engineering
- Nuclear Engineering
- Optical Engineering
- Petroleum Engineering
- Robotics & Automation Engineering
- Telecommunications Engineering

CFP SCHEDULE

Volume: 4
Issue: 3
Paper Submission: May 2010
Author Notification: June 30 2010
Issue Publication: July 31 2010

CALL FOR EDITORS / REVIEWERS

CSC Journals is in process of appointing Editorial Board Members for ***International Journal of Engineering (IJE)***. CSC Journals would like to invite interested candidates to join **IJE** network of professionals/researchers for the positions of Editor-in-Chief, Associate Editor-in-Chief, Editorial Board Members and Reviewers.

The invitation encourages interested professionals to contribute into CSC research network by joining as a part of editorial board members and reviewers for scientific peer-reviewed journals. All journals use an online, electronic submission process. The Editor is responsible for the timely and substantive output of the journal, including the solicitation of manuscripts, supervision of the peer review process and the final selection of articles for publication. Responsibilities also include implementing the journal's editorial policies, maintaining high professional standards for published content, ensuring the integrity of the journal, guiding manuscripts through the review process, overseeing revisions, and planning special issues along with the editorial team.

A complete list of journals can be found at http://www.cscjournals.org/csc/byjournal.php. Interested candidates may apply for the following positions through http://www.cscjournals.org/csc/login.php.

Please remember that it is through the effort of volunteers such as yourself that CSC Journals continues to grow and flourish. Your help with reviewing the issues written by prospective authors would be very much appreciated.

Feel free to contact us at coordinator@cscjournals.org if you have any queries.

Contact Information

Computer Science Journals Sdn BhD
M-3-19, Plaza Damas Sri Hartamas
50480, Kuala Lumpur MALAYSIA

Phone: +603 6207 1607
+603 2782 6991
Fax: +603 6207 1697

BRANCH OFFICE 1
Suite 5.04 Level 5, 365 Little Collins Street,
MELBOURNE 3000, Victoria, AUSTRALIA

Fax: +613 8677 1132

BRANCH OFFICE 2
Office no. 8, Saad Arcad, DHA Main Bulevard
Lahore, PAKISTAN

EMAIL SUPPORT
Head CSC Press: coordinator@cscjournals.org
CSC Press: cscpress@cscjournals.org
Info: info@cscjournals.org

COMPUTER SCIENCE JOURNALS SDN BHD
M-3-19, PLAZA DAMAS
SRI HARTAMAS
50480, KUALA LUMPUR
MALAYSIA